ELECTRON AND MOLECULAR DYNAMICS: PENNING IONIZATION AND MOLECULAR CHARGE TRANSPORT

by

Tamika Arlene Madison

B.S. University of Pittsburgh, 2005

Submitted to the Graduate Faculty of
Arts and Sciences in partial fulfillment
of the requirements for the degree of
Doctor of Philosophy

University of Pittsburgh

2011

UNIVERSITY OF PITTSBURGH

FACULTY OF ARTS AND SCIENCES

This dissertation was presented

by

Tamika A. Madison

It was defended on

April 12th, 2011

and approved by

Lillian T. Chong, Professor, Department of Chemistry

Joseph G. Grabowski, Professor, Department of Chemistry

David Yaron, Professor, Department of Chemistry, Carnegie Mellon University

Dissertation Advisor: Geoffrey R. Hutchison, Professor, Department of Chemistry

Dissertation Advisor: Geoffrey R. Hutchison

ELECTRON AND MOLECULAR DYNAMICS: PENNING IONIZATION AND MOLECULAR CHARGE TRANSPORT

Tamika A. Madison, PhD

University of Pittsburgh, 2011

An understanding of fundamental reaction dynamics is an important problem in chemistry. In this work, experimental and theoretical methods are combined to study the dynamics of fundamental chemical reactions. Molecular collision and dissociation dynamics are explored with the Penning ionization of amides, while charge transfer reactions are examined with charge transport in organic thin film devices.

Mass spectra from the Penning ionization of formamide by He*, Ne*, and Ar* were measured using molecular beam experiments. When compared to 70eV electron ionization spectra, the He* and Ne* spectra show higher yields of fragments resulting from C─N and C─H bond cleavage, while the Ar* spectrum only shows the molecular ion, H-atom elimination, and decarbonylation. The differences in yields and observed fragments are attributed to the differences in the dynamics of the two ionization methods. Fragmentation in the Ar* spectrum was analyzed using quantum chemistry and RRKM calculations. Calculated yields for the Ar* spectrum are in excellent agreement with experiment and show that 15% and 50% of the yields for decarbonylation and H-atom elimination respectively are attributed to tunneling

The effects of defects, traps, and electrostatic interactions on charge transport in imperfect organic field effect transistors were studied using course-grained Monte Carlo simulations with explicit introduction of defect and traps. The simulations show that electrostatic interactions dramatically affect the field and carrier concentration dependence of charge transport in the presence of a significant number of defects. The simulations also show that while charge transport decreases linearly as a function of neutral defect concentration, it is roughly unaffected by charged defect concentration. In addition, the trap concentration dependence on charge transport is shown to be sensitive to the distribution of trap sites.

Finally, density functional theory calculations were used to study how charge localization affects the orbital energies of positively charged bithiophene clusters. These calculations show that the charge delocalizes over at least seven molecules, is more likely to localize on “tilted” molecules due to polarization effects, and affects molecules anisotropically. These results suggest that models for charge transport in organic semiconductors should be modified to account for charge delocalization and intermolecular interactions.

TABLE OF CONTENTS

LIST OF TABLES

LIST OF FIGURES

ACKNOWLEDGEMENTS

My journey to this point in my academic career has seen many challenges and I would not have made it through without my faith and the help of others. I would like to take a moment to acknowledge some of those who have helped me along the way.

I would first like to acknowledge my family and friends. My mother Stephanie did a great deal of fighting for me to have the same educational opportunities as my peers despite my vision impairment as I was growing and has always given me her love and encouragement. My sisters and brothers: James, Tosha, Tiara, Shawn, Stephanie, Steven, Anthony, and Sierra have been my best friends by always making me smile, listening to my problems, having fun, and giving me a lot of love. My grandma Mary always gave me extra love, support and good advice when I needed it. My best friend Andrea has always been there to cheer me up and commiserate with me about the world. There are a large host of family members and friends that I cannot mention here by name, but please know that you have my deepest gratitude and that I love you all.

I would also like to thank the University of Pittsburgh Varsity Marching Band for giving me an outlet during my time in graduate school as well as during my undergraduate years. Being a member of the Pitt band got me through some of the lowest times in my graduate career by

allowing me to express myself through music and providing me with friends that I will be connected to for the rest of my life.

Next, I would like to thank my friends and colleagues in the Chemistry department here at Pitt. I would first like to thank my fellow group members in the Siska and Hutchison groups for the experimental and programming assistance, stimulating discussion, the constructive criticism, and the many fun lunches and coffee runs. You have no idea how special it is for me to be considered "part of the group". Dr. David Waldeck has always looked out for me during my graduate career, especially during Dr. Siska's illness and after his passing. Dr. Joseph Grabowski stepped in as my advisor during Dr. Siska's illness. The Machine and Electronics shops helped me to fix and maintain instrumentation in the Siska lab. All of the faculty members and office staff, who have given me assistance, served on a committee, or given me a kind word. Thank you all for giving me so much support and for being my academic family.

Last but certainly not least; I would like to acknowledge my research advisors, Dr. Geoff Hutchison and the late Dr. Peter Siska. Thank you so much Dr. Hutchison for letting me a part of your group. I have really enjoyed working with you and have learned a great deal during the time I spent here. Thank you for providing me with the many opportunities to present my research, for patiently guiding me through research problems, and for having faith in me. All of your support has greatly improved my self-confidence and my growth as a chemist.

As I prepared this dissertation and for my defense, I have thought a lot about Dr. Siska and the time I spent in his lab. I would like to thank him for that time, developing my confidence in the lab, supporting and enriching my teaching interests, and most of all for his kindness and faith in me. I will never forget you and you are greatly missed.

There are so many others who have contributed positively to my educational journey who I have not mentioned by name here. Please know that I have certainly not forgotten you and that you have my sincerest gratitude.

Dedicated to

Dr. Peter E. Siska

“If ever there is tomorrow when we’re not together… there is something you must always remember. You are braver than you believe, stronger than you seem, and smarter than you think. But the most important thing is, even if we’re apart… I’ll always be with you.”

~A. A. Milne, *Winnie the Pooh*

1.0 INTRODUCTION: PENNING IONIZATION AND ION FRAGMENTATION OF AMIDES

1.1 THE PENNING IONIZATION REACTION

Penning ionization (PI) is a form of chemi-ionization that proceeds through the following:

$$A^* + BC \rightarrow [ABC]^* \rightarrow [ABC]^+ + e^- \quad (1)$$

where A^* is an excited species and BC is a ground state target species. When A^* and BC collide, they form the activated complex $[ABC]^*$. If the frontier orbitals of A^* and BC have similar energy and symmetry, they will overlap and a valence electron from BC will be extracted by A^*. If the excitation energy of A^* exceeds the ionization energy of BC, then the excited electron is ejected, leading to the formation of the activated complex $[ABC]^+$. $[ABC]^+$ may undergo any of the following:

$$[ABC]^+ \rightarrow A + BC^+ \text{ (Penning ionization)} \quad (2a)$$

$$[ABC]^+ \rightarrow ABC^+ \text{ (Associative ionization)} \quad (2b)$$

$$[ABC]^+ \rightarrow AB + C^+ \text{ (Rearrangement ionization)} \quad (2c)$$

$$[ABC]^+ \rightarrow A + B + C^+ \text{ (Dissociative ionization)} \quad (2d)$$

The fate of $[ABC]^+$ depend on the dynamics of initial collision. There has been a small debate over what should be considered “Penning ionization”; traditionally the first of the reaction products is considered to be the Penning ionization reaction. However, it has been argued that the Penning ionization reaction should be defined as the entire chemi-ionization process itself.[1] For the sake of this discussion, the formation of A and BC^+ will be referred to as Penning ionization, since it is the focus of this work. The molecular ion formed in this reaction, BC^+ may decompose into smaller fragments depending on the amount of excess energy it has after ionization.

The year 2007 marked the 80th anniversary of the discovery of this process by Frans M. Penning during his studies of the breakdown of neon and argon gas discharges in the presence of impurities.[2] He implicated the metastable states of these noble gas atoms as the culprits for this process. This discovery came at an important time in the history of chemistry and physics, in the midst of the quantum revolution. Penning was one of the first to suggest that there are some electronically excited states that cannot radiate to the ground state. This hypothesis, coupled with the observation of “missing” transitions in atomic line spectra led to the derivation of “selection rules” to explain allowed and forbidden electronic transitions. For these reasons, Penning’s discovery has made a major contribution to quantum theory.

1.2 THE PENNING IONIZATION MECHANISM

The mechanism of Penning ionization can be described using a “two potential” model which is illustrated in Figure 1.1. This model is a classical treatment of Penning ionization as presented by Miller in a 1970 paper.[3] This model is based on the Born-Oppenheimer approximation, which allows for the nuclear and electronic motion to be separated at a fixed separation of two or more nuclei. In this model, $V_0(r)$ is a potential energy function that describes the $A^* + R$ system, where A* is an excited state atom and R is a target species. $V_+(r)$ is the potential energy function that describes the $A + R^+$ system where A is the ground state atom and R^+ is the ionized target. Both functions depend on r, which is the distance between A^* and the center of mass of R (if R is a molecule). Figure 1.1 shows the situation in which the ionization energy of R is less than the excitation energy of A^*. In this case, $V_+(r)$ is the lower bound of a continuum of potential energy states for the $A + R^+ + e^-$ that take the form of $V_+(r) + \varepsilon$, where ε is the energy of the ionized electron. At any fixed distance r, $V_0(r)$ is embedded in this continuum of states. The decay of the discrete electronic state of $V_0(r)$ into this continuum of states is facilitated by an imaginary component of $V_0(r)$ denoted $\Gamma(r)$, the resonance width, which arises due to degeneracy of the incoming state with a state in the continuum. This decay into the continuum via $\Gamma(r)$ is what causes Penning ionization. It should also be noted that as r approaches infinity, $\Gamma(r)$ approaches zero. This means that Penning ionization is less likely to occur at large distances.

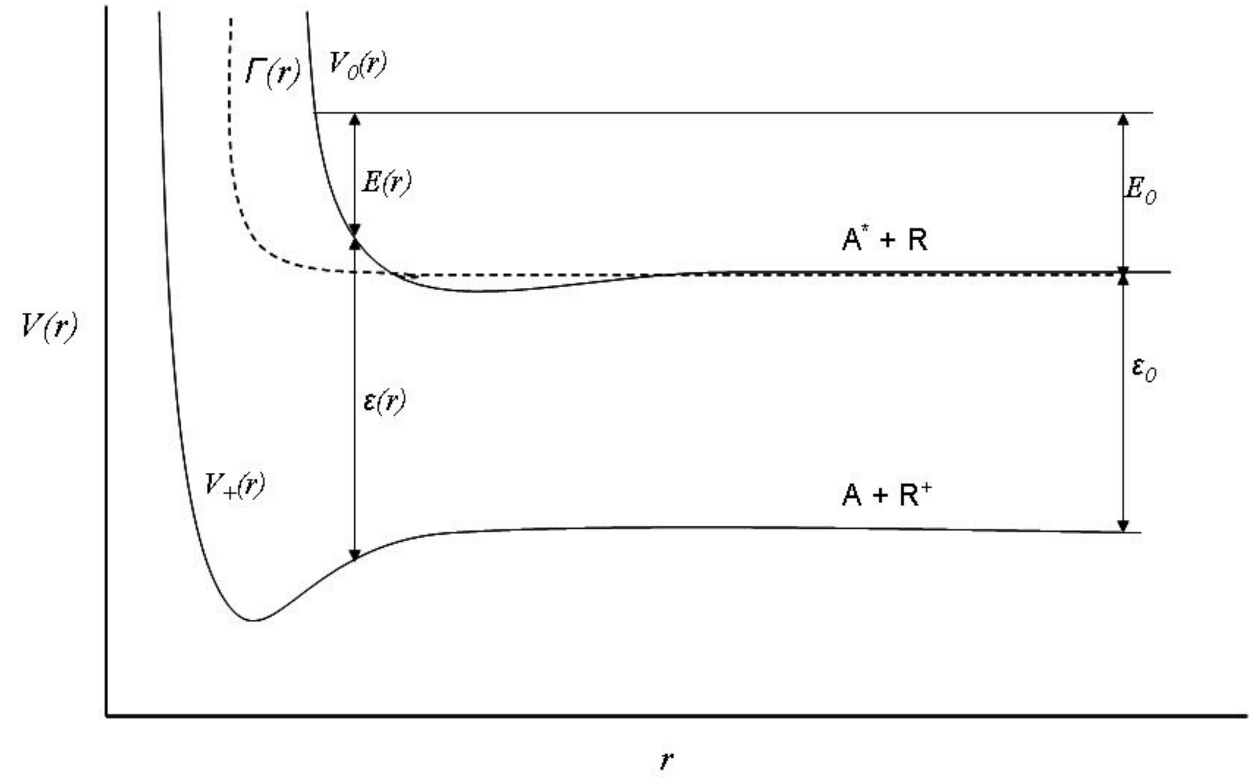

Figure 1.1. The two potential model for Penning ionization

There are other features of this model, which should be noted. The energy ε_0 is the difference between the asymptotes of $V_0(r)$ and $V_+(r)$ and is also equal to the excitation energy of A^* less the ionization energy of R. E_0 is the kinetic energy of the center of mass for the collision. $E(r)$ is the classical kinetic energy of the colliding heavy particles at distance r and includes the centrifugal energy of the system. The final term, $\varepsilon(r)$, is the kinetic energy of the ejected Penning electron at distance r. If the kinetic energy of the Penning electron is sufficiently large (or if the well in the $V_+(r)$ potential function is sufficiently deep), the complex AR^+ may not be able to break up into $A + R^+$, resulting in associative ionization. It is also important to note that if R is molecular (as it is in this study) all of the curves in Figure 1 become multi-dimensional surfaces, which further complicates the model.

1.3 LITERATURE REVIEW

The majority of Penning ionization studies focus on understanding its dynamics in terms of molecular collisions. However, as the size of the target molecule grows, the intermolecular potential surfaces (IPES) become more complex due to their dependence on the conformation of the molecule. Because of this, Penning ionization studies must either take these into account, either by using multi-dimensional methods or by shifting towards more statistical and analytical endeavors.

In the proceeding sections, synopses of three related areas are presented. First, a short history of molecular beam studies of the Penning ionization reaction is presented; a more extensive review was published by Siska in 1993[4]. Next, the history of applications of Penning ionization to mass spectrometry is given. Finally, a history of the study of unimolecular decay of molecular ions is presented.

1.3.1 Molecular Beam Studies of Penning Ionization Dynamics

Molecular beam studies of Penning ionization and related processes were begun in the 1960's in order to gain insight into their dynamics. A wide variety of experiments can be done using molecular beams; this section will focus on experiments that include mass analysis of the ions produced during the Penning reaction.

The most common measurements using mass analysis were to determine the total ionization cross section (Q_I) and branching ratios for different possible ionization pathways (Q_{XI}/Q_I, where XI is the type of ionization pathway), related to the signal collected at a certain mass and collision energy. The total ionization cross section measures the probability of ionization occurring when two species interact. Branching ratios measure the fraction of the total ionization cross-section associated with a given ionization process. Angle energy distributions of ions were also measured using a mass analyzer that could be rotated to measure ionic products scattered at different angles.

The measurement of Q_I using a beam apparatus goes back a 1962 paper by Sholette *et al*.[5] In this study, Q_I was measured for 7 species (including Ar-Xe) using He^* ($2^{1,3}S$), although they did not include mass analysis. Since then, Q_I and Q_{XI}/Q_I have been measured on a variety of systems, mostly using He^* ($2^{1,3}S$). For example, Q_I and Q_{AI}/Q_I have been measured for atomic systems (only Penning ionization and associative ionization are possible for these systems); the most studied atom is H (D),[6-7] since it is the simplest atomic species to consider theoretically. For diatomic molecules, there are two more ionization channels possible, rearrangement ionization and dissociative ionization. The most studied diatomic molecule is H_2,[8-9] although there are also a few studies on HD and other diatomic molecules. There are also a handful of studies on triatomic and small organic molecules. The total ionization cross section tends to increase with the surface area of the species and is larger for the 2^1S state than for the 2^3S state. These trends can be seen clearly in an article by Schmeltekopf et al.,[10] who measured the quenching cross section for 18 species from noble gas atoms to small hydrocarbons for both spin states of He^*. There are fewer ionization cross-section studies that use Ne^*[11-14] and other metastable atoms. In all studies, Penning ionization has the highest ionization cross section of the possible ionization channels.

Angle energy distribution measurements have also been done on very simple systems. Again, most of the measurements have been done with He^* with very few done with Ne^* and other metastable noble gases. The targets that have been studied to date with He^* are H (D),[15-16] Ar,[17-18] H_2,[19] N_2,[20] O_2, CO,[21] CO_2, and CH_4[22]. With Ne^*, only H (D)[23] and Ar have been studied. These studies have found that the Penning ionization products are mostly scattered forward with respect to the target beam in the center of mass frame.

There are alternative measurements to mass analysis, including Penning ionization electron spectroscopy (PIES)[24-30], which measures the kinetic energy of the Penning electron, and non-reactive angular distribution (NAD) measurements[31-34] that look at the decay of the [ABC]* complex back into reagents. PIES spectra have improved over the years in terms of the resolution of vibrational states of the species in question. PIES spectra also yield a great deal of information about the internal energy distribution of the Penning ion. This aspect of PIES will play a major role in this study. NAD measurements provide a great deal of information about the nature of $V_0(r)$ and dynamics of the Ng^* + R system before ionization.

1.3.2 Penning Ionization and Mass Spectrometry

The application of Penning ionization to mass spectrometry has been limited and still remains in the realm of academia. A few early studies of Penning ionization as an ion source in mass spectrometry looked mainly at the yields of the Penning ion and its fragments[35-36]. The ion sources in these studies did not always separate ions formed from Penning ionization from those that may have been formed in the process of forming the metastable atoms. In 1993, Bertrand and co-workers[37] first illustrated the application of Penning ionization to mass spectrometry using a separate metastable atom source. This article was also the first to refer to the use of Penning ionization in analytical mass spectrometry as metastable atom bombardment (MAB). In this report, MAB mass spectra were taken of anisole and 2-butanone using He^*-Kr^* produced by passing a corona discharge through a noble gas beam. It was shown that by knowing the ionization potentials and appearance potentials of the analyte along with excitation energies of the metastable noble gases, one could control the degree of fragmentation. It was also shown that one could selectively ionize an analyte in a mixture by using a metastable atom with the appropriate excitation energy comparing Ne^* and Kr^* MAB spectra of a 2:1:1 phenol/water/acetonitrile mixture. This study first showed that MAB mass spectrometry provides more versatility than electron impact without sacrificing sensitivity. Since then, only a few articles that applied MAB to analytical problems have appeared[38-45].

However there are virtually no studies on the MAB mass spectra of a homologous series of organic molecules. Only one report by Hiraoka et al. seems to study this[46]. In this report an atmospheric pressure negative corona metastable atom source was used to study a series of hydrocarbons (C_5 – C_8). It was observed that the molecular ion ($M^{+\bullet}$) intensity increased with the size of the carbon chain in He^* spectra. In pentane through heptane, the $(M - H)^{+\bullet}$ was the most intense peak. However in the octane spectrum, the $M^{+\bullet}$ peak is more intense than the $(M - H)^{+\bullet}$ peak. Also, it was shown that the intensity of the $M^{+\bullet}$ peak of octane decreased in the order of He^* - Kr^* (it was not visible in the Kr^* spectrum). There was however an increase in fragmentation. These observations were attributed to the lifetimes of the molecular ion; if the lifetimes are long enough, they can undergo collisional deactivation in the atmospheric pressure ion source.

1.3.3 Unimolecular Decay of Radical Cations

In order to gain a theoretical understanding of what is observed in a mass spectrum, one has to examine the unimolecular kinetics of the radical cation in question. The use of unimolecular kinetics to study gas phase molecular ion fragmentation was reviewed in a set of papers in volume 118 of the International Journal of Mass Spectrometry and Ion Processes in 1992 in back to back articles. The first article, written by Lifshitz[47] discussed the use of RRKM/QET to describe a variety of processes, including molecular ion decomposition. The second article by Radom[48] outlined the use of computational chemistry methods used to describe the chemistry of gas phase ions. He discussed the calculation of such properties as heats of formation, transition states, and vibrational frequencies using various levels of theory, which are valuable in the theoretical interpretation of mass spectra. Since then, few articles have been published on computational studies of the unimolecular kinetics of gas phase ions; some not directly related to mass spectrometry experiments. Most molecular ions studied were radical cations of organic molecules. The next two studies found in the 1990's were by Ruttink et al. in 1995[49] and McAdoo et al. in 1998[50]. The Ruttink paper discussed the decarbonylation of formamide and will be discussed in more detail later. The McAdoo paper discussed the unimolecular decomposition of the propane radical cation. The transition states and vibrational frequencies connected with the elimination of a hydrogen atom, methyl radical, and methane were calculated using QCISD(T) and UMP2 levels of theory. This information was used to calculate the rate constants and reaction profiles for the formation of these fragments and their corresponding ionic byproducts as a function of internal energy using RRKM theory with a correction for tunneling.

In the present century, two computational studies that include RRKM analysis of the thiomethane radical cation appeared six years apart[51-52]. Also, an article on the decomposition of the ethanol radical cation was published in 2006[53] that also included RRKM analysis. Recently, an article appeared in *Science* that discussed the dynamics of different conformations of the propanal cation,[54] but did not include RRKM analysis. There have also been a few studies directly related to mass spectrometry experiments[55-58], however none of these studies include RRKM analysis. None of the studies mentioned go so far as to predict the ion yields in a mass spectrum using RRKM theory.

1.4 PROJECT DESCRIPTION

The metastable atom bombardment mass spectra of formamide ($HCONH_2$) and acetamide (CH_3CONH_2) were examined. Amides were chosen for study because of their importance in biological systems as well as their chemical properties. Also, these molecules have not been studied using MAB mass spectrometry. The amide functional group ($RCONR_2$) contains an O═C─N linkage, a very unique connection of carbon and the two most important heteroatoms in organic chemistry. This linkage also provides amides with a delocalized pi system, which makes them the least reactive of the carboxylic acid derivatives. The amide linkage, because of its stability, plays a crucial role in biological systems since it is how amino acids polymerize to form polypeptides and proteins. Therefore the amide C─N bond can be viewed as the simplest version of a peptide linkage.

The MAB spectra will be compared with available electron impact mass spectra, to see if there is any difference in the fragmentation of formamide and acetamide between the two ionization methods. In particular, selective bond cleavage was examined. The key competition between bond cleavages is the C─N and C─H(C) bonds. Fragmentation that does not require hydrogen atom loss in amides can make MAB mass spectrometry of amides a precursor to MAB mass spectrometry of polypeptides and proteins. If MAB mass spectra show a higher propensity for C─N and bond cleavage than for electron impact mass spectra, it may be very useful in sequencing polypeptide chains.

MAB mass spectrometry is also a good place to apply the theory of mass spectrometry. The degree of fragmentation depends on the amount of excess energy available after ionizing the target species. In MAB mass spectrometry, the amount of energy available for fragmentation is the excitation energy of the noble gas atom less the ionization energy of the target, since all of the excitation energy of the noble gas atom is transferred to the molecule. For electron impact, this energy excess is not well defined, since the electrons have a lower energy transfer efficiency that can vary between measurements. The energy deposition functions for these molecular ions were determined using their corresponding Penning ionization electron spectra (PIES).

Also needed are the rate constants for the decay of the molecular ion into fragments, which can be calculated using unimolecular kinetics (RRKM theory). The rate constants are determined using vibrational frequencies and barrier heights from first principles quantum chemistry calculations. These calculations along with the energy deposition function are used to produce a theoretical mass spectrum that is used to help interpret the experimental MAB spectra. The last step of these calculations has not been performed with studies of radical cations, mainly because the energy deposition function is difficult to determine for other methods of ionization in mass spectrometry. This makes this study unique since it is one of the few studies of the MAB spectra of a homologous series of molecules that includes a full theoretical treatment of the radical cation decomposition that predicts a mass spectrum.

2.0 EXPERIMENTAL: MOLECULAR BEAM EXPERIMENT

2.1 THE VACUUM SYSTEM

All mass spectra were collected using a crossed beam apparatus modeled from the "beam machine" of Y.T. Lee.[59] Figure 2.1 shows a top down view of the chambers of the apparatus and Figure 2.2 is a detailed schematic of the experimental setup. The apparatus was encased in a 42 x 37 x 26 inch stainless steel chamber. Two adjacent faces of the main chamber housed the buffer chambers in which the supersonic beam sources sat. The main chamber also housed the effusive beam source and the detector assembly. One side of the main chamber was a removable aluminum door for maintenance. The roof of the chamber was also removable and contained a sprocket and chain mechanism, which allowed for the detector assembly to be rotated. Both the door and lid had o-ring seals.

The main chamber, buffer chambers and beam sources were kept under high vacuum using separate diffusion pumps (Varian VHS model series). The foreline pressures of the diffusion pumps were kept at around 0.1 torr using mechanical pumps (Welch 1375). The mechanical pumps were also used to put the chambers under "rough vacuum" before they are introduced to the diffusion pumps. The pressure of each chamber and beam source was measured using Granville Phillips (Series 274) ion gauges. Under experimental conditions the pressures in the main chamber, buffer chambers and nozzle chambers read between 10^{-6} - 10^{-8}, 10^{-5} - 10^{-6}, and 10^{-3} - 10^{-4} torr respectively.

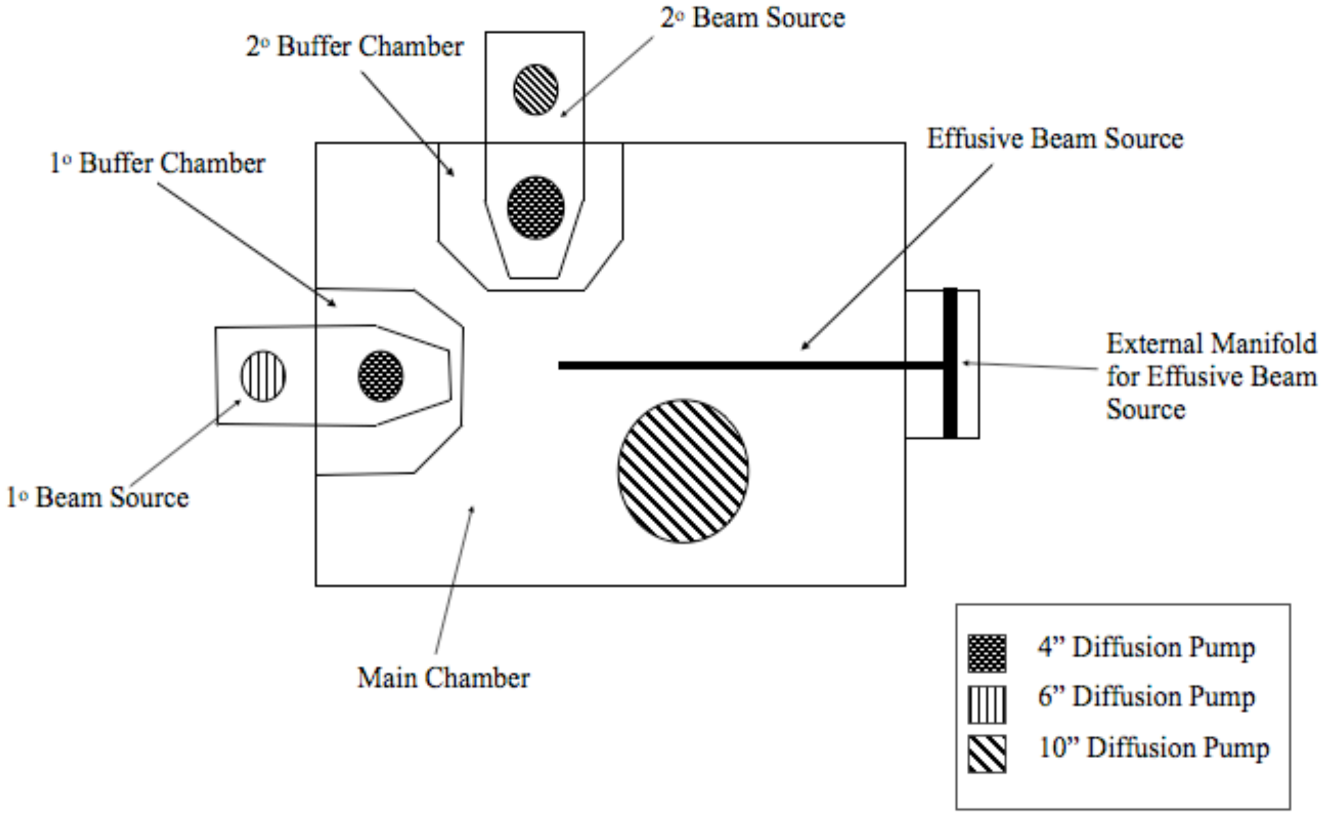

Figure 2.1. Top down schematic of the vacuum system for the crossed beams apparatus

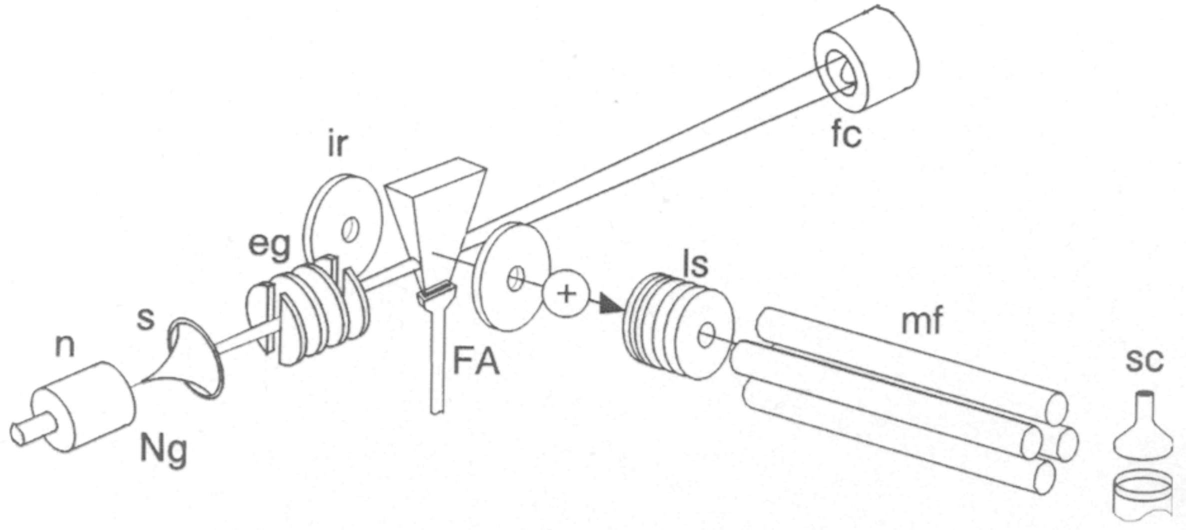

n = nozzle
s = skimmer
Ng = noble gas beam source
eg = electron gun
FA = formamide effusive beam source
fc = Faraday cup
ir = ion extractor
ls = retarder-lens assembly
mf = quadrupole mass filter
sc = scintillation ion counter

Figure 2.2. Crossed beam experimental set-up.

2.2 BEAM SOURCES

2.2.1 Metastable Noble Gas (Ng*) Beam Source

The metastable atoms are produced by electron impact on a supersonic noble gas beam. The noble gases were purchased from Valley National Gasses (He 99.997% purity), Air Products (Ne 99.99% purity), and Matheson (Ar, 99.999% purity). The supersonic beam was formed by expanding gas from a high-pressure reservoir through a through a 0.08mm orifice and a skimmer, into the low-pressure buffer chamber. As the gas expands, the random translational motion of the atoms is converted into forward motion. The result is a beam with a high and narrow velocity distribution.

The supersonic noble then traveled through the electron gun. The noble gas beam first meets a set of parallel plates. One of these plates is grounded, the other is “floating” on ceramic spacers that keep it ungrounded. This plate acts as a deflector and is biased at -500V with a Hewlett Packard (HP) model 6448D power supply. Next, the beam travels through a grounded tungsten mesh electrode and then a tungsten filament; which provides the electron impact source. The filament was connected in series with a 2 kΩ resistor, biased at -500 V and “floating” on ceramic spacers. The filament current was supplied by a HP model 6282A power supply. An emission current is generated between the tungsten mesh electrode and the filament and this electron beam is what is used for electron impact. The electron beam is directed anti-parallel to the noble gas beam. The deflector keeps the electron beam from traveling into the nozzle of the beam source, where it may cause residual pump oil to polymerize and clog the nozzle. A custom-built emission current regulator regulated the emission current.

The beam then passes through another set of parallel plates similar to the previously described set. This deflector removes ions and electrons created in the impact process before the beam finally exits the gun through a slit. The distance from the exit slit of the electron gun and the exit point of the primary buffer chamber was about 1cm. The resulting beam now contains metastable noble gas atoms and a few Rydberg atoms mixed in a ground state neutral noble gas beam. The populations and excitation energies of the metastable states for each noble gas are given in Table 2.1. Note that the beam populations were measured for this particular beam source only and the populations may vary in other beam sources in different laboratories. The metastable beam current is measured using a Faraday cup, which is made of copper and is coated with aquadag (graphite in a mixture of organic solvents). The metastable beam strikes the graphite layer, producing ions via Penning ionization. The ion current produced in this reaction is directly related to the strength of the metastable beam and is measured using a Keithley Model 416 picoammeter.

Table 2.1. Metastable Noble Gas Beam Source Conditions

Noble Gas	Electronic State	Excitation Energy[4] (eV)	Beam Populations[60, a]
He	2^3S	19.8696	0.11
	2^1S	20.6198	
Ne	$^3P_2$	16.6193	3.35
	$^3P_0$	16.7156	
Ar	$^3P_2$	11.5484	2.97
	$^3P_0$	11.7232	

---

[a] For He*: 2^3S / 2^1S, for Ne*and Ar*: $^3P_2$ / $^3P_0$

2.2.2 Effusive Beam Source for Amide Samples

The effusive beam source was constructed of copper tubing, and stainless steel flexible tubing. The Ultratorr fittings used to connect the tubing were made of stainless steel and brass and o-ring seals. Starting from beam crossing, the nozzle was constructed from 1/8 inch copper tubing that was flattened on one end. The nozzle was then connected to a flexible tube and a ¼ inch copper line that ran the length of the main chamber parallel to the metastable beam source. The flexible tube allowed for the nozzle to be adjusted so that the target beam intersects the metastable beam at a right angle. The copper line was then connected to an external manifold via a stainless steel feed thru. A toggle valve on the external manifold was used to isolate the external and internal components of the beam source. This valve was left open during a background scan.

The external manifold was equipped with vent and pump lines that were connected to a ¼ inch diameter copper line via “t junctions”. This copper line ran perpendicular to the internal line. A flexible tube connected the copper line to a second toggle valve that separated the sample vapor from the rest of the manifold. Another flexible tube connected the manifold to a barostat via a ball joint and O-ring seal. The barostat held the sample at a constant pressure and was equipped with a heating element sealed in an evacuated space between the sample tube and the outside wall. The amide samples were purchased from Acros Organics (formamide and acetamide purity was 99.5% and 99% respectively) and were used without further purification

2.3 ION EXTRACTION, DETECTION, AND MASS ANALYSIS

The ion extraction assembly was similar to that used in a previous study.[9] The ionic products of the Penning ionization reaction were accelerated toward a grounded electrode by an ion extractor plate biased at +60 V. The ions have an energy of +30 eV as they reach the grounded electrode. After passing through the grounded electrode, the ions passed through a series of 3 element lenses that focused the ions toward the quadrupole mass filter. The quadrupole was biased at +20 V to slow the ions to a kinetic energy of 10 eV. Lambda LPD model series power supplies powered the ion extractor and lenses voltage(s) as well as the quadrupole bias. The quadrupole was also home built; it measured ¾ x 9 inches, and was controlled by an Extranuclear power supply and controller.

After the ions traveled through the mass analyzer, they went through another series of lenses (powered by a Power Designs model 2K20 high voltage power supply) that focused the ions into a scintillation detector similar to that designed by Daly in 1960[61]. The ions hit a "door knob" electrode set at -25kV using a Bertan model 605B high voltage power supply. The impact of the ions on this electrode produces a secondary burst of electrons that impacts a sheet that is made of an organic phosphorescent material. This impact produces a burst of photons that enter an EMI model 9524S photomultiplier tube. The photomultiplier tube was powered by a Power Designs Inc. Model 1-2012 high voltage power supply. The pulses of current from the photomultiplier tube passed through an Ortec model 9302 discriminator and amplifier and were counted by a Jorway model 1836 dual channel scaler and monitored by a Mech-tronics model 775 counting rate meter.

2.4 DATA ACQUISITION

Spectra were collected using a computer interface. A QuickBasic program controlled the mass analyzer by commanding it to ramp through a preset mass range using a preset step size. The step size was typically 0.1 amu. At each step the program recorded the number of counts read from one channel of the dual channel scaler. The mass scan was repeated several times to improve the signal-to-noise ratio of the spectrum. The number of counts for each step was summed over the number of scans. The program also showed a graphical representation of the data and could also write a text file that included experimental settings as well as the data. The text file could then be modified and analyzed using Microsoft Excel or other data analysis programs.

Each experiment required the collection of four spectra, the background and background + signal, each at both low and high resolution. High-resolution spectra were recorded with the condition that all observed product masses were baseline resolved, while low resolution spectra were recorded with the condition that the parent ion peak was at its highest intensity. The low-resolution condition generally resulted in peak widths of around 4 amu. The set of spectra was used to account for the mass dependent transmission of analyzer at high resolution.

3.0 PENNING IONIZATION AND ION FRAGMENTATION OF FORMAMIDE BY HE*-AR*[b]

3.1 INTRODUCTION

In this chapter, the first measurements of the mass spectra generated by thermal energy Penning ionization (PI) of formamide using He*, Ne*, and Ar* metastable atoms are presented. In the next section, the data reduction process is discussed and the resulting mass spectra are presented. This is followed by a thermodynamic assessment of open fragmentation channels in the Ng* + $HCONH_2$ system. Finally, the analysis of the fragmentation in the Ar* + $HCONH_2$ system using tunneling corrected RRKM theory along reaction paths generated using quantum chemistry calculations is outlined and discussed.

3.2 DATA REDUCTION AND MASS SPECTRA

Quantitative ion abundances were extracted from the experimental mass spectra by least squares simulations of the background subtracted spectra at high and low resolution. This analysis

---

[b] Based on published work[62]

employed Gaussian peak shape functions, which were found to represent the high-resolution peak shapes closely. However, to simulate the low-resolution peak shapes, flat-topped peaks with Gaussian wings replaced the Gaussians. Simulation of the high-resolution peaks allowed for the determination of all m/z produced along with the relative intensities of each m/z within a group of peaks (within a 5 amu range). Optimized Gaussian peak-widths differed from one group of peaks to another but were held constant within the grouping itself. The problem of peak overlap is resolved by the modeling and the abundances of the mass peaks are proportional to the least squares Gaussian amplitudes.

The corresponding low-resolution spectrum was simulated by retaining the relative intensities obtained by the high resolution fit and varying only the relative intensities of the clusters of mass peaks themselves. The abundances obtained from these fits are taken to be the final values. Error bars for the fits are determined by the statistical noise in the original data with the allowance for imperfect modeling and transmission variation within a cluster of mass peaks. Figures 3.1-3.3 show representative raw, background subtracted, and fitted spectra for each Ng* + $HCONH_2$ reaction studied.

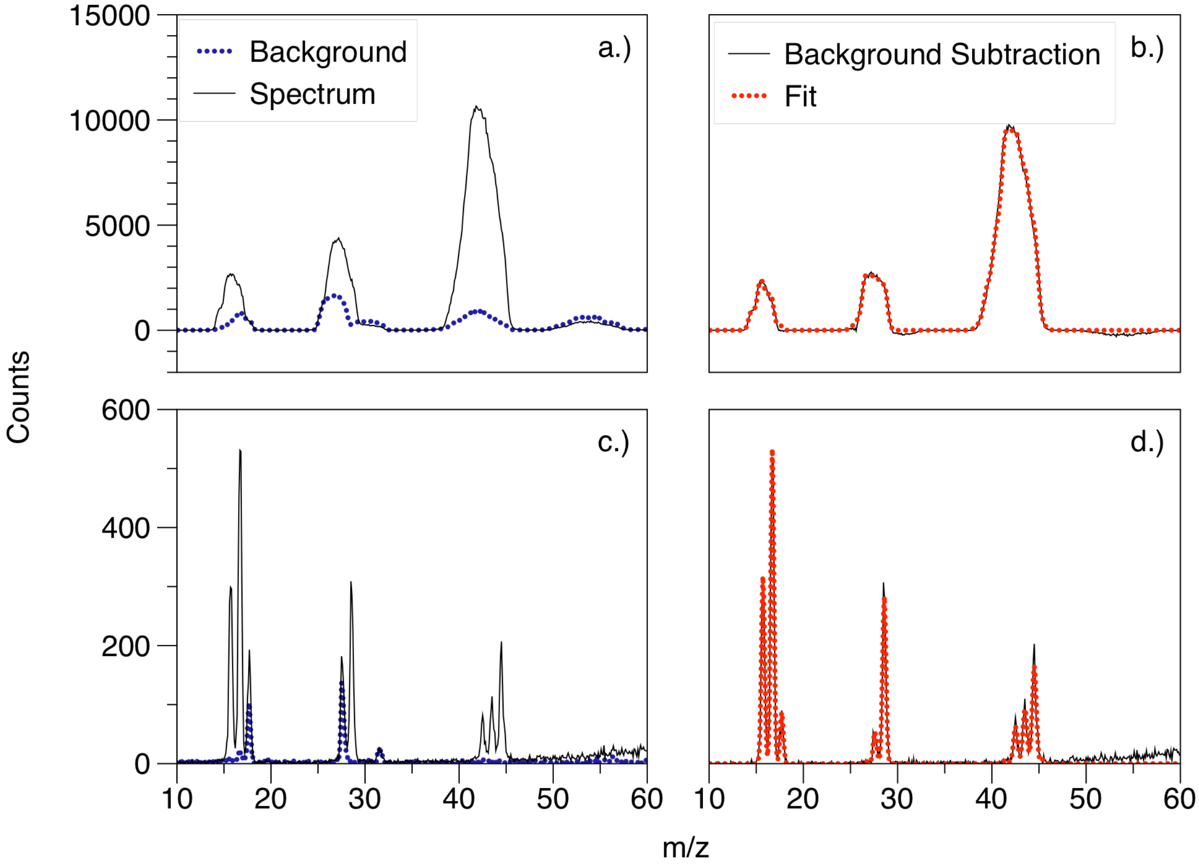

Figure 3.1. Simulation of He* + $HCONH_2$ Spectra. a.) Raw low resolution spectra, b.) Background subtraction and least squares fit for low resolution spectrum, c.) Raw high resolution spectra, d.) Background subtraction and least squares fit for high resolution spectrum.

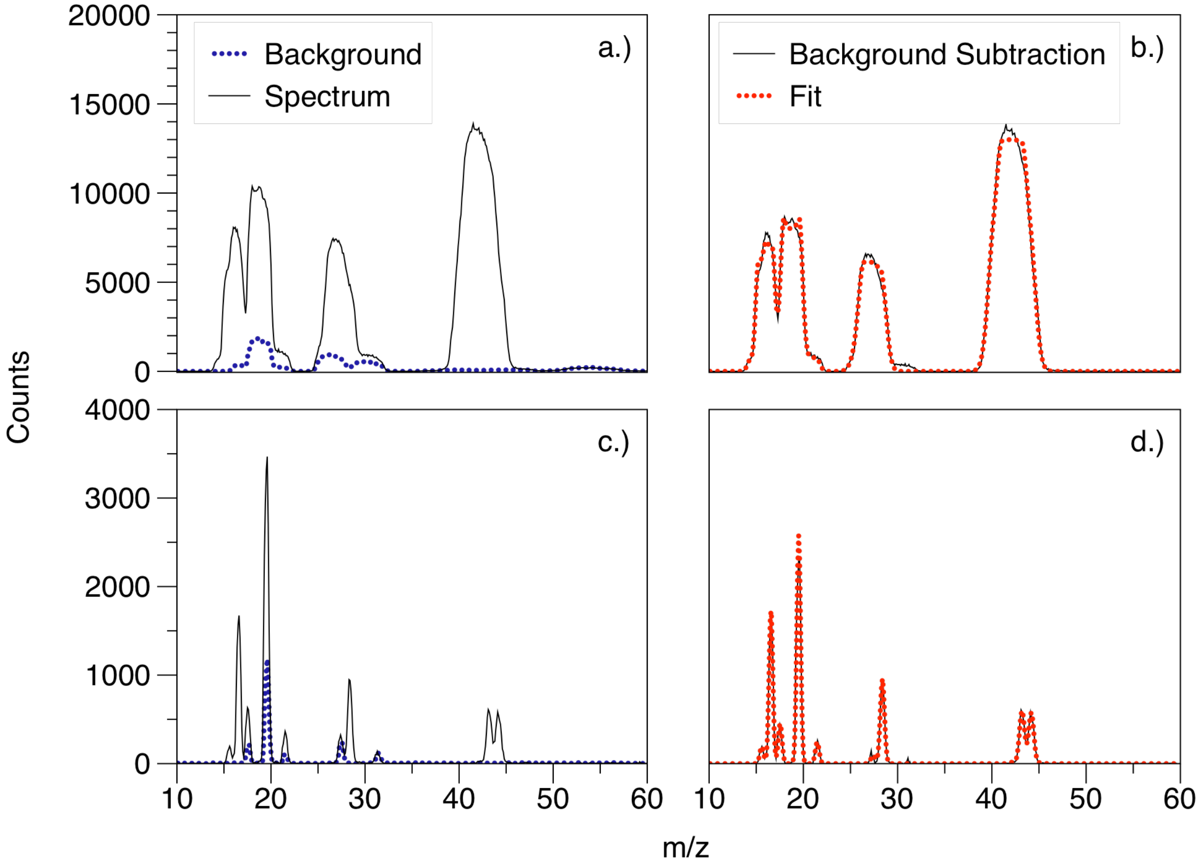

Figure 3.2. Simulation of Ne* + $HCONH_2$ spectrum**.** a.) Raw low resolution spectra, b.) Background subtraction and least squares fit for low resolution spectrum, c.) Raw high resolution spectra, d.) Background subtraction and least squares fit for high resolution spectrum.

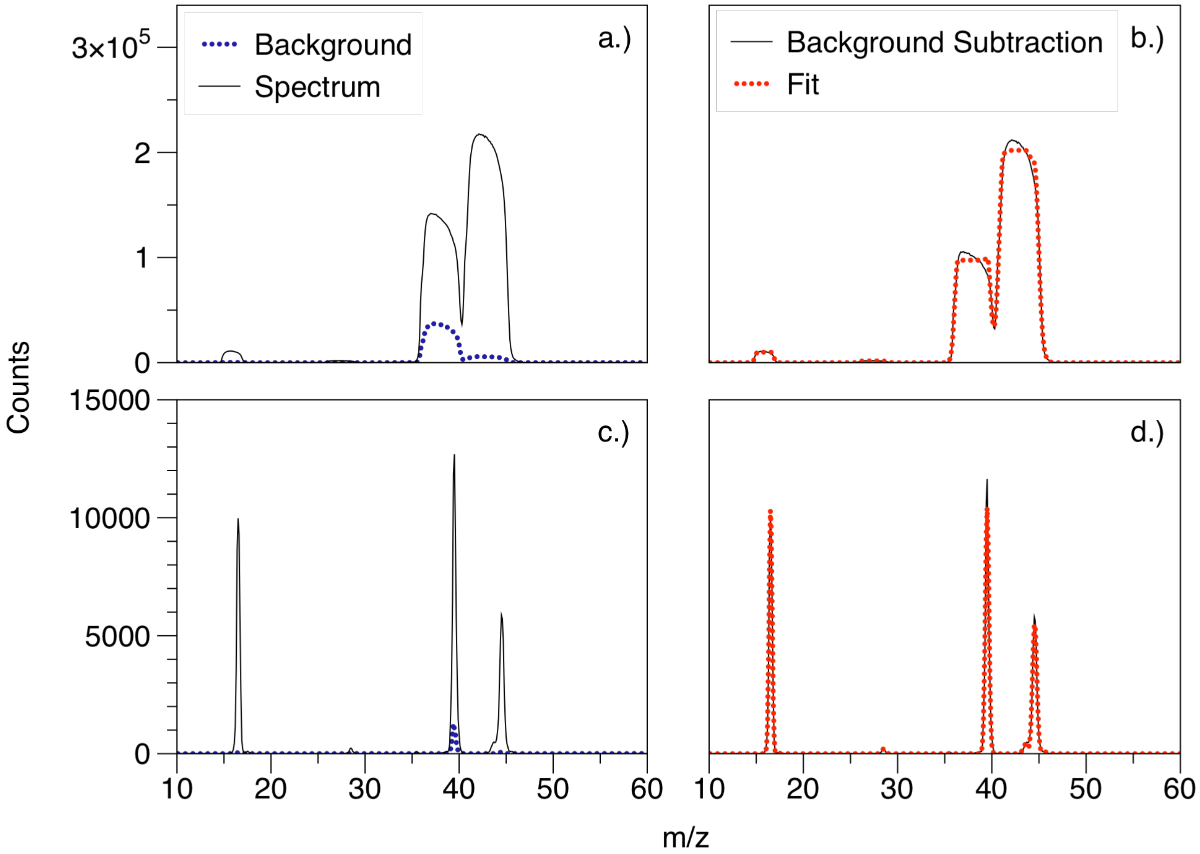

Figure 3.3. Simulation of Ar* + $HCONH_2$ Spectrum. .) Raw low resolution spectra, b.) Background subtraction and least squares fit for low resolution spectrum, c.) Raw high resolution spectra, d.) Background subtraction and least squares fit for high resolution spectrum.

For each analysis, the least squares program gave three output files. The "data" output file contained the raw and background subtracted spectra as well as the simulated spectra. The "parameter" output file contained the parameters used for least squares fitting as well as the resulting number of counts for each peak. The "stick" output file contained the final results of the fitting and included the relative abundances for each m/z with the highest peak normalized to unity. This file was used to plot the spectra as histograms. Figure 3.4 show representative spectra for each Ng* + $HCONH_2$ reaction studied. The 70 eV electron impact (EI) spectrum from the NIST Webbook[63] is included for comparison.

The determination of the final ion yields were done by comparing the relative abundances for each collected data set (see Appendix A). Peaks that resulted from the noble gas Rydberg ions were omitted from this analysis since they were not the result of Penning ionization. Also not included in this analysis was the isotopic m/z 46 peak, m/z values that had relative abundances that fell below 1% or whose relative abundances had a large standard deviation (> $\underline{+}$10). The m/z values that had large standard deviations were generally peaks that corresponded to peaks observed in both the background and background + signal spectra. The ion yields were then calculated from the number of counts given in the parameter output files.

Table 3.1 gives the percent yields for the product ions; included are the yields from the 70 eV electron ionization (EI) mass spectrum from the NIST webbook for comparison. Again, relative abundances and yields resulting from the ionization of Rydberg atoms (Ng**) are not reported since they do represent open channels resulting from Ng* reactions nor do they bear any necessary abundance relations to these reactions. The assignment of the mass peaks is a result of the thermochemistry calculations described in Section 3.4

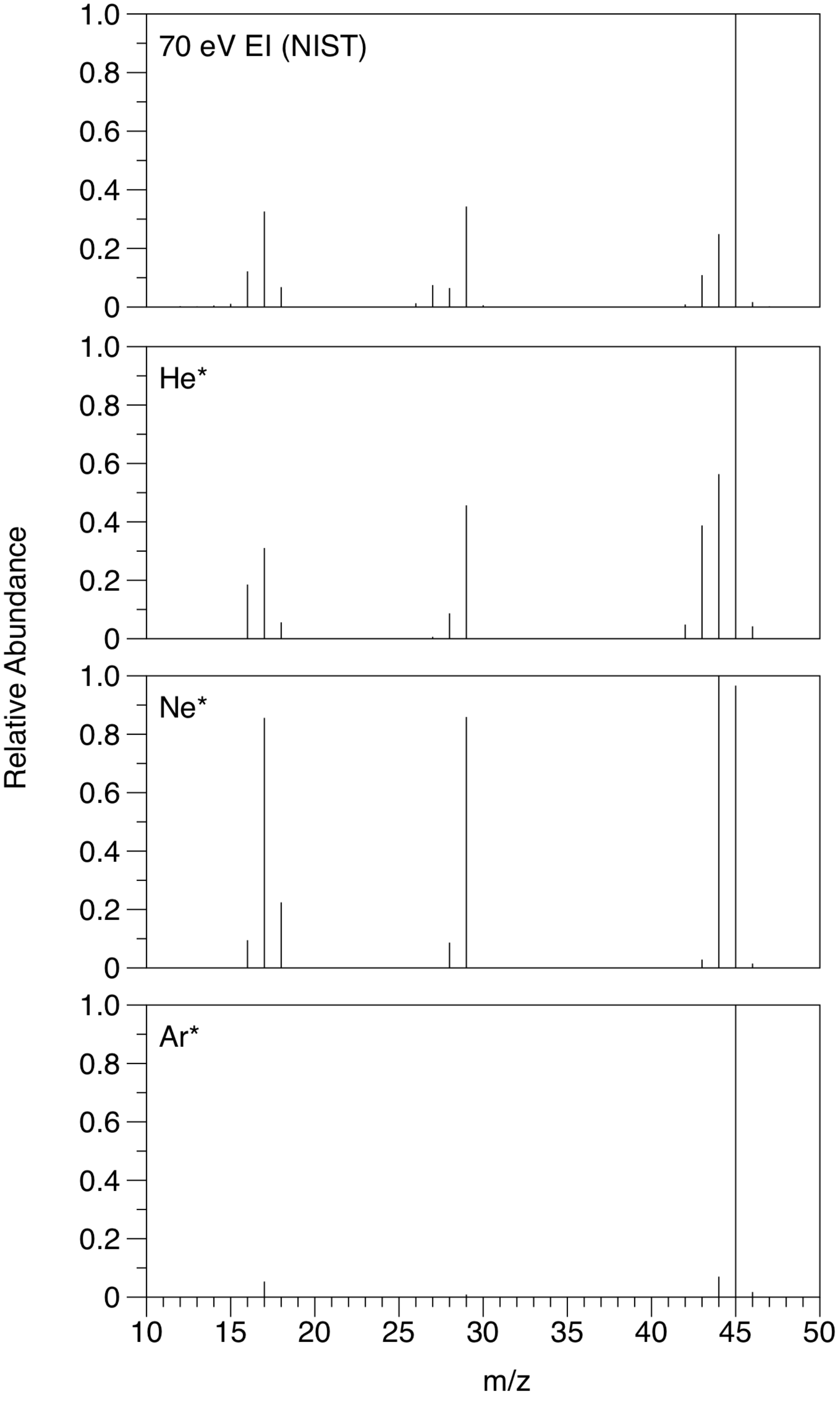

Figure 3.4. Mass spectra for Ng* + $HCONH_2$. The 70 eV EI spectrum (top) is included for comparison.

Table 3.1. Percent Yields for Ng* + $HCONH_2$.

m/z	Formula of Ion[c]	He*	Ne*	Ar*	70 eV EI Spectrum
12	†[d]	-	-	-	0.1
13	†	-	-	-	0.1
14	CH_2^+	-	-	-	0.2
15	CH_3^+	-	-	-	0.5
16	NH_2^+	7.5 ± 1.5	2.9 ± 1.6	-	5.0
17	$NH_3^{+\bullet}$	11.5 ± 1.9	21.4 ± 0.7	5.4 ± 1.5	13.4
18	$H_2O^{+\bullet}$	1.9 ± 0.5	-	-	2.8
26	†	-	-	-	0.5
27	$HCN^{+\bullet}$	-	-	-	3.1
28	$HCNH^+$	-	1.9 ± 0.9	-	2.6
29	HCO^+	15.7 ± 1.3	24.5 ± 1.9	0.7 ± 0.3	14.1
30	$H_2CO^{+\bullet}$	-	-	-	0.2
42	OCN^+	0.8 ± 0.7	-	-	0.8
43	$OCNH^{+\bullet}$	13.0 ± 1.0	0.6 ± 0.4	-	4.5
44	$CONH_2^{+\bullet}$	18.0 ± 1.2	25.0 ± 1.1	6.0 ± 0.6	10.2
45	$HCONH_2^{+\bullet}$	31.6 ± 1.4	23.7 ± 1.3	87.9 ± 0.6	41.1
46	*[e]	-	-	-	0.7
47	*		-	-	0.1

3.3 PENNING IONIZATION TOTAL CROSS SECTIONS

Unlike the case for many of the Penning ionization reactions involving small molecules studied in this laboratory, the reactions between He* - Ar* and $HCONH_2$ is expected to have a relatively attractive intermolecular potential energy surface (IPES). Experimental evidence of this comes from known PIES results for He* + $HCONH_2$[64-65] which show a nearly uniform shift toward low electron energy (~ -0.3 eV) of all peaks that correspond to the valence levels. In the two potential model of Penning ionization[3], this is roughly equal to the attractive well depth of the

---

[c] Based on ionization/fragmentation endoergicities calculated in this work

[d] Dagger indicates that the ionization/fragmentation endoergicity for an ion at that m/z was not evaluated in this work

[e] Asterisk indicates m/z values corresponds to isotopic peaks

IPES. Although the present IPES are also expected to be anisotropic, the results presented here are unlikely to be sensitive to such details.

Our experiments do not yield absolute cross sections, but they can be estimated. The spherically averaged long range attractive potential is of the form,

$$V(R) = -\frac{C}{R^6} \tag{3}$$

where R is the distance between Ng* and formamide. C may be written as a sum of the dispersion and dipole-induced dipole terms,

$$C = C_{Disp} + \mu^2 \alpha^* \tag{4}$$

Here, μ and α^* are the dipole moment of formamide and the polarizability of Ng* respectively. The dispersion term (C_{Disp}) is given by,

$$C_{Disp} = \frac{3}{2}\left(\frac{I_A I_B}{I_A + I_B}\right)\alpha_A \alpha_B \tag{5}$$

where I and α are the ionization energies and polaraizabilites of the colliding species respectively.

Assuming that ionization occurs for all collisions that surmount the centrifugal barrier for *V(R)* (i.e. “close” collisions), the maximum cross section is given by:

$$Q_c(s) = \pi\left[\frac{s}{s-2}\right]^{\frac{s-2}{s}}\left[\frac{sC}{E_{rel}}\right]^{\frac{2}{s}} \tag{6}$$

Here *s* is the number of atoms in the target molecule (s = 6 for formamide) and E_{rel} is the relative kinetic energy of Ng* and formamide (E_{rel} = 1 kcal/mol for this study).

Table 3.2 lists the estimated cross sections for the Ng* + $HCONH_2$ systems in this work. It should be noted that these cross sections are much larger than typical electron-ionization cross sections for organic molecules.[66] This compensates for the weaker fluxes obtained in molecular beam studies. Also note that *V(R)* approaches -0.3 eV for *R*=3.7 – 4.7 Å. These distances are comparable to the largest impact parameters for which capture can occur.

Table 3.2. Estimated total ionization cross sections for Ng* + $HCONH_2$

Ng*	State	C_{Disp} (10^3 a.u.)[f]	C (10^3 a.u.)	Q(s=6) (Å^2)
He*	2^3S	1.56	2.24	221
Ne*	$^3P_2$	0.948	1.35	187
Ar*	$^3P_2$	1.46	2.46	218

3.4 ION FRAGMENTATION ENERGETICS

In order to identify the fragments whose masses are detected, one may examine the reaction endothermicities ($\Delta H_{rxn,\ 298K}$) for all possible fragmentation pathways of the form,

---

[f] Input data for formamide are I = 10.226 eV, μ = 3.73 D, and α = 4.08 Å^3. The ionization energies and polarizabilites for Ng* can be found in Ref . 4.

$$P \rightarrow D_1 + D_2^+ \qquad (7)$$

Here, the molecular ion P is dissociating into two fragments, one neutral and one ionized. $\Delta H_{rxn,\ 298K}$ may be easily calculated from the standard enthalpies of formation ($\Delta H_{f,\ 298K}$) for the fragments and for the molecular ion. These values for the molecular ions and neutral fragments for the most part may be obtained from the NIST webbook. For the ionized fragments, $\Delta H_{f,\ 298K}$ may be calculated by summing $\Delta H_{f,\ 298K}$ and the ionization energy (IE) of the neutral counterparts. For fragments that do not have tabulated $\Delta H_{f,\ 298K}$ or IE data, $\Delta H_{f,\ 298K}$ may be calculated using quantum chemistry. In this work, the CBS-QB3[67] method was used to calculate $\Delta H_{f,\ 298K}$ for such fragments. This was done using the thermodynamic cycle outlined in Section A.2.

From the reaction endothermicities, the reaction endoergicities (ΔE_{0K}) may be evaluated. The usefulness of ΔE_0 is twofold. ΔE_0 is needed in the RRKM calculations to define the reaction barrier shape. Also, the beam sources that are used cool the reactants down to temperatures close to absolute zero, which "freezes out" vibrational degrees of freedom. Therefore, to accurately compare the likelihood of observing certain fragments, ΔE_0 is needed since it omits the thermal energy contribution.

Internal energies (e.g. – ΔE_T) are not tabulated, however they may be calculated using ΔH_T. The definition of enthalpy (ΔH) is:

$$\Delta H \equiv \Delta E + P\Delta V \qquad (8)$$

Using the ideal gas approximation, the reaction endothermicity (ΔH_T) can be related to the reaction endoergicity (ΔE_T) by:

$$\Delta H_T = \Delta E_T + \Delta n_g RT \tag{9}$$

Here, Δn_g is the change in moles for the reaction; in most fragmentation channels studied here this value equals 1. ΔE_T is defined by:

$$\Delta E_T = N_A \sum_j v_j \bar{\varepsilon}_j + \Delta E_0 \tag{10}$$

The first term is the thermal energy change. v_j is a stoichiometric coefficient for the reaction pathway and ε_j is given by:

$$\bar{\varepsilon}_j = \bar{\varepsilon}_t + \bar{\varepsilon}_v + \bar{\varepsilon}_r \tag{11a}$$

$$\varepsilon_t = \frac{3}{2} RT \tag{11b}$$

$$\bar{\varepsilon}_v = \frac{hc\tilde{v}}{e^{-hc\tilde{v}} - 1} \tag{11c}$$

$$\bar{\varepsilon}_r = \begin{cases} RT \ (Linear) \\ \frac{3}{2} RT \ (Non-Linear) \end{cases} \tag{11d}$$

ε_j can be calculated using experimental vibrational frequencies.[63] ΔE_0 can be evaluated by substituting equation 8 into equation 9 and rearranging. ΔE_0 may also be calculated using quantum chemistry if ΔH_T and/or vibrational frequencies for one or more fragments are unavailable. Here, the CBS-QB3 method[67] was used. Table 3.3 gives the values for $\Delta H_{rxn,\ 298K}$, the thermal energy change (ΔE_{therm}) and ΔE_0. ΔE_0 can be compared to the excitation energy of the metastable atoms to determine whether or not a certain fragmentation pathway will be observed in a particular spectrum as shown in Figure 3.5.

Table 3.3. Ionization/fragmentation endoergicities for low lying fragments of $HCONH_2$.

$D_1 + D_2^+$	m/z	ΔH_{298K} (kcal/mol)	ΔE_{therm} (kcal/mol)	ΔE_0 (kcal/mol)
$CO + NH_3^{+\bullet}$	17	242.2	26.6	237.7
$H + CONH_2^+$	44	261.0[g]	-	251.2[g]
$OH + HCNH^+$	28	280.1[g]	-	269.5[g]
$H_2 + HNCO^{+\bullet}$	43	288.0	30.80	285.9
$NH_2 + HCO^+$	29	288.1	34.34	286.3
$HCN + H_2O^{+\bullet}$	18	310.0	29.47	308.37
$N + CH_2OH^+$	31	326.7	23.5	328.2
$NH_3 + CO^{+\bullet}$	28	332.1	26.6	328.66
$H_2O + HCN^{+\bullet}$	27	332.5	29.47	330.9
$O + HCNH_2^{+\bullet}$	29	351.2[g]	-	345.6[g]
$HCO + NH_2^+$	16	364.5	34.34	347.1
$NH + H_2CO^{+\bullet}$	30	357.8	26.4	356.
$CH_2 + HNO^{+\bullet}$	31	393.4	26.7	392.0
$H + H_2 + OCN^+$	42	417.7	1.671	394.5
$HNO + CH_2^{+\bullet}$	14	399.2	26.7	398.8

---

[g] Calculated using the CBS-QB3 method

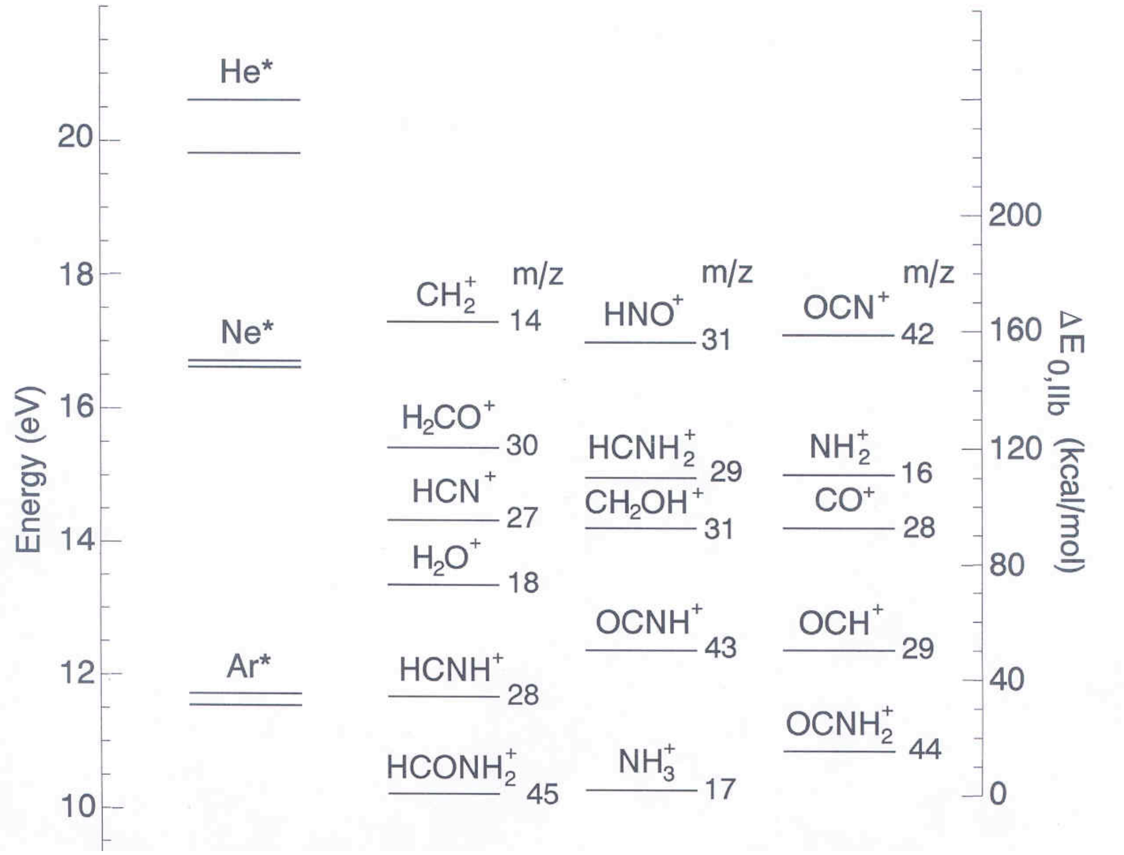

Figure 3.5. Fragmentation energetics: Ng* + HCONH$_2$

3.5 COMPARISON OF PENNING IONIZATION WITH ELECTRON IONIZATION AND ION ENERGETICS

In general, if ΔE_0 for a fragmentation channel falls below the excitation energy of a certain Ng*, the ionized fragment should appear in the spectrum. Figure 3.5 shows that all listed fragmentation channels should be observed in the He* spectrum. However in the experimental spectrum m/z 14, 30 and 31 are not observed although these peaks should be observed according their values of ΔE_0. The absence of these ions may be attributed to high activation energies for the corresponding channels. For the Ne* spectrum, three fragmentation pathways become energetically closed; the formation of OCN^+ (m/z 42), ONH^+ (m/z 31), and CH_2^+ (m/z 14). This coincides with the absence of these ions in the experimental Ne* spectrum. For the Ar* spectrum, only three fragmentation channels are open; hydrogen atom loss (m/z 44), decarbonylation (m/z 17), and $HCNH^+$ formation (m/z 28). In the experimental spectrum only m/z 17 and 44 are present in addition to the molecular ion peak. Also, a small yield of formyl ion is observed, while the endoergicity for this channel lies above the excitation energy of Ar*. This may be due to collisional energy transfer between the molecular ion and Ar*,

$$Ar^* + HCONH_2^{+\bullet} \rightarrow Ar + [HCONH_2^{+\bullet}]^* \tag{12}$$

This would result in the molecular ion having more excess internal energy, which would allow for the fragmentation channel to become accessible.

In the EI spectrum, the ion with the highest yield is that of the molecular ion with the peaks arising from the fragmentation having much smaller yields (less than 50%). This is not the case in the PI spectra. In the He* spectrum, the yields for the ions resulting from hydrogen atom and molecule loss (m/z 44 and 43 respectively) are considerably higher than that those in the standard 70 eV EI spectrum accompanied by a smaller molecular ion yield. In the Ne* spectrum the ions that result from decarbonylation, hydrogen atom loss and direct C─N bond cleavage (m/z 29) are far larger than those in the 70 eV. In fact, these three channels have nearly the same yields within the experimental error bars. PI, unlike EI is a chemical reaction that involves the frontier orbitals of the Ng* and the target species. Orbital overlap must occur in order for ionization to take place and orbital overlap is maximized if the energy and symmetry of the involved orbitals are similar. For example, the highest occupied molecular orbital (HOMO) for formamide is a non-bonding p orbital located on oxygen (10a′)[68]. Ne*'s singly occupied 2p orbital would therefore interact more strongly with this orbital. This would also be true for Ar* except the orbital overlap would decrease since the 3p orbital is larger in size and of a different energy. Ionization at 10a′ results in α-cleavage on either side of the carbonyl, producing m/z 29 and 44 as well as m/Z 17 when C—N bond cleavage is accompanied by proton transfer (see Figure 3.6). Therefore it is expected that the yields at these m/z values would be higher than in the He* spectrum since He* orbitals do not have the same symmetry as 10a′. However, it is expected that some degree of overlap between He* and 10a′ would occur, depending on the angle of approach, which would explain the increased yield of m/z 43 and 44 in the He* when compared to the 70 eV EI spectrum. Since EI is not dependent on orbital overlap, it is difficult to predict where ionization occurs and trends in ion yields.

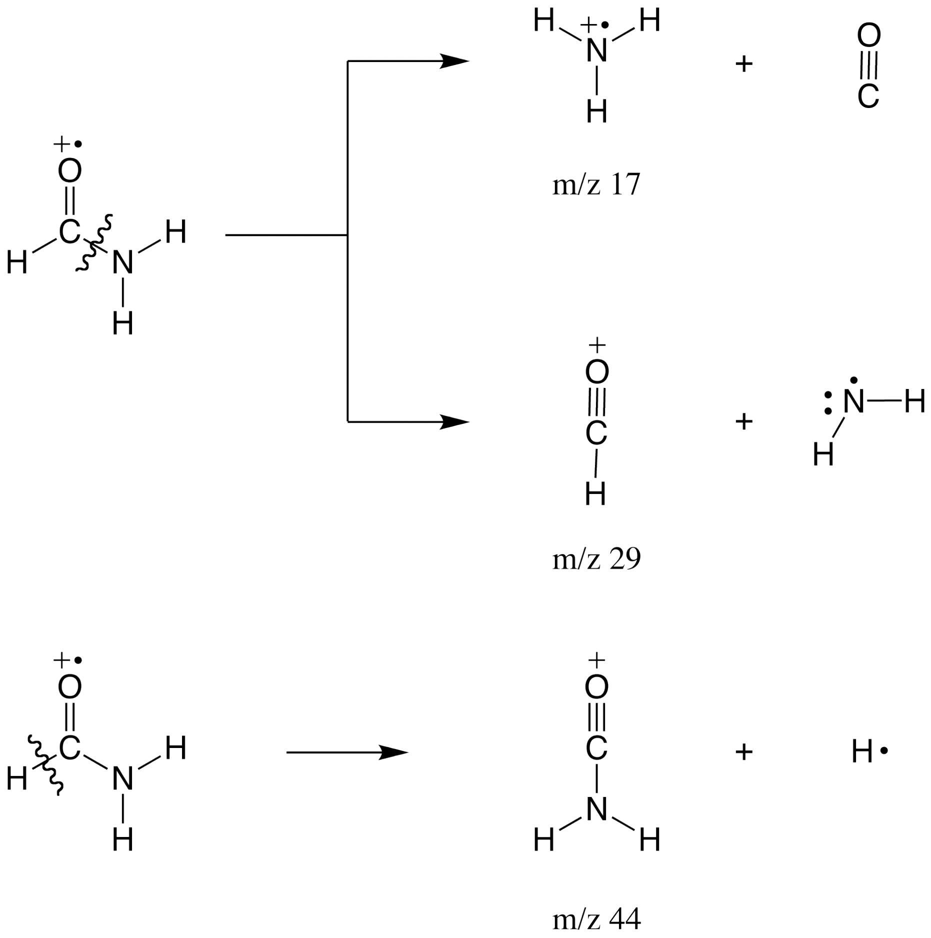

Figure 3.6. Fragmentation channels resulting from α-cleavage in formamide.

3.6 THEORETICAL CALCULATION OF THE AR* + HCONH$_2$ SPECTRUM

3.6.1 Quantum Chemistry Calculations

In order to calculate the RRKM rate constant for a fragmentation pathway, several pieces of information are needed. The “bare” barrier heights for the forward (V_0) and reverse reactions (V_1) are needed. The “bare” barrier heights can be calculated from the activation energies (E_a) by subtracting the zero point energy (E_z) of the molecular ion, transition state, and the fragments. Also needed are the vibrational frequencies of the molecular ion, transition states (TS) and fragments. This requires the geometries of the molecular ion, TS structures and fragments. These data may be obtained from quantum chemistry.

The first two channels in Table 3.3, (H atom loss and decarbonylation) were taken to be open for the Ar* + HCONH$_2$ spectrum. The first step in locating transition states that connect the molecular ion to the fragments in each channel involved performing a series of relaxed potential energy scans. This was done by varying a coordinate of the molecular ion (either a bond length or angle) and optimizing all other coordinates at each scan step. This creates an energy profile that is a function of the scanned coordinate. If the scan indicated that there was a transition structure between the molecular ion and fragments, it’s geometry was optimized to a TS and a frequency calculation was performed (looking for one imaginary frequency to confirm a TS). The transition structure was further characterized by performing an intrinsic reaction coordinate (IRC) calculation.[69] This calculation is done by taking the steepest descent from the transition state in both the forward and reverse directions along the reaction coordinate, which in this case is a composite of mass weighted internal coordinates dependent on bond lengths, angles and dihedrals. At each step in the calculation, the geometry is optimized for each structure so that the segment between two points can be described as the arc of a circle and the gradient for all points are tangent to the reaction path. The IRC calculation was used to confirm that the transition structure connects the molecular ion to the desired fragments.

All quantum chemistry calculations were performed using the Gaussian 03 software package. Initial calculations were performed using unrestricted Hartree-Fock (UHF) and Møller-Plesset perturbation (UMP2) theories with a 6-31g(d) basis set. In order to obtain more accurate energies, the composite CBS-QB3 method[67] was adopted. This method includes a geometry optimization and frequency calculation using the B3LYP functional and a 6-311G(d, p) basis set. The frequencies are scaled by a factor of 0.99. This is followed by a series of calculations at the MP2, MP4 and QCISD(T) levels of theory in order to include effects of electron correlation in the final energy. The MP2 energy calculation includes an extrapolation to the complete basis set limit. The result of using this method is very accurate energy calculations without a high computational cost (due to the use of DFT theory). For this reason, the CBS-QB3 method is widely used in the field of mass spectrometry theory.[57-58, 70-71]

Table 3.4 lists the results of these calculations for the Ar* + $HCONH_2$ system and Figure 3.7 illustrates the geometric specifications for each structure. E_a for decarbonylation and H atom loss are 21.3 and 20.2 kcal / mol respectively, which is above the zero point energy of the molecular ion. V_0 for each channel was calculated using the CBS-QB3 frequencies to obtain the zero point energies. V_1 was calculated using the theoretical reaction endoergicities given in Table 3.6.

Table 3.4. Results of CBS-QB3 calculations for m/z 17 and 44 fragmentation channels

Species	Electronic Energy (AU)	E_Z	V_0	V_1	ω (cm^{-1})
			(kcal/mol)		
$HCONH_2$	-169.69842	27.7			3719 3581 2921 1818 1620 1423 1268 1056 1049 653 568 219
$HCONH_2^{+\cdot}$	-169.30629	28.4			3508 3388 3121 1608 1436 1066 1037 1373 958 882 677 547
H_2N---$HCO^{+\cdot}$ (TS 17)	-169.26590	23.7	25.4	24.9	3481 3390 3220 2223 1532 928 566 424 414 291 94 549i
H---$CONH_2^{+\cdot}$ (TS 44)	-169.26547	22.4	25.6	3.45	3570 3444 2331 1585 1211 1113 593 545 518 511 234 518i
$CO + NH_3^{+\cdot}$	-169.30544	23.6			2220; 3515 3515 3341 1531 1531 870
$H + CONH_2^{+\cdot}$	-169.27110	21.3			3533 3437 2436 15y2 1230 1119 579 504 467

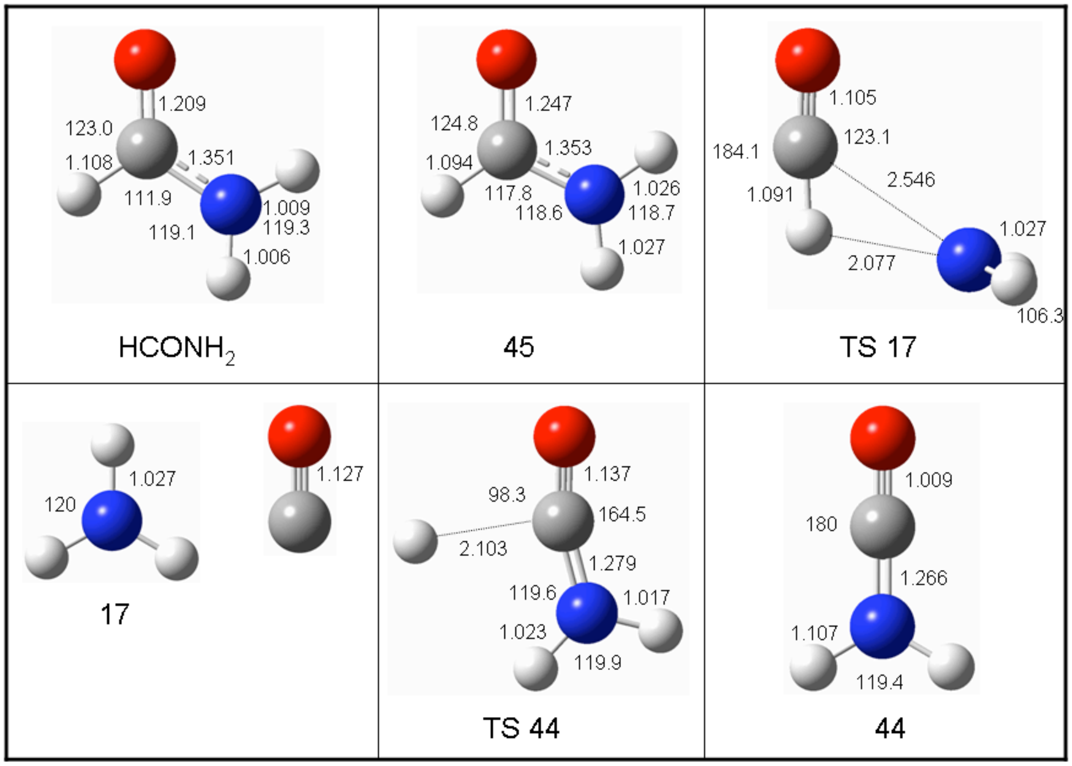

Figure 3.7. Geometry specifications for the m/z 17 and 44 fragmentation channels. CBS-QB3

3.6.2 Unimolecular Decay

In order to describe the kinetics of molecular ion fragmentation in terms of a unimolecular (RRKM) rate constant, the quasi-equilibrium theory (QET) may be used. QET assumes that the ionization of the target species is “vertical” and results in an odd electron ion that has low symmetry. Also, the low lying electronic states of the molecular ion are assumed to form a continuum that allows for the excess electronic energy of the molecular ion to be randomly distributed to its vibrational degrees of freedom on the timescale of one bond vibration. The rate of fragmentation then depends on the probability of the excess energy distribution becoming concentrated in certain degrees of freedom leading to TS structures that result in certain fragments.

Neglecting rotational degrees of freedom, the RRKM rate constant for P^+ with total energy E (including vibrational zero point energy) may be written as:

$$k(E) = \frac{N(E)}{h\rho_0(E)} \tag{13}$$

N(E) is the total number of energy states available to the transition state, $\rho_0(E)$ is the density of states for P^+ and *h* is Planck’s constant. The discrete quantum states for $\rho_0(E)$ may be approximated to be continuous; in this case the Whitten – Rabinowich approximation[72] was used. *N(E)* is the integral of the density for the TS and increases by a series of steps with increasing *E*, and can be written as,

$$N(E) = \sum_{n} H(E - \varepsilon_n^*) \tag{14}$$

$H(x)$ is the Heaviside step function ($x = E - \varepsilon^*_n$), which is,

$$H(x) = \begin{cases} 0, x < 0 \\ 1, x > 0 \end{cases} \tag{15}$$

$n \equiv [n_1, n_2, \ldots, n_{s-1}]$ is a collective quantum number, the n_j are vibrational quantum numbers and s is the number of vibrational degrees of freedom in P^+. ε^*_n is the vibrational energy of the transition state relative to P^+ in the harmonic oscillator approximation and is written as,

$$\varepsilon_n^* = V_0 + \sum_{j=1}^{s-1} hc\omega_j^* \left(n_j + \frac{1}{2} \right) \tag{16}$$

V_0 is the "bare" height of the barrier that separates P^+ from its fragments and $[\omega^*_j]$ are the vibrational frequencies.

In order to account for tunneling, the procedure outlined by Miller in 1979[73] was followed. This involves replacing the Heaviside function with the one-dimensional tunneling probability $P_{tun}(E - \varepsilon^*_j)$. In order to calculate P_{tun}, the shape of the reaction barrier needs to be defined. Following Miller, the Eckart potential[74] was chosen to represent the reaction barrier. The Eckart potential is defined as,

$$V(y) = -\frac{Ay}{(1-y)} - \frac{By}{(1-y)^2}, y = e^{-\frac{2\pi x}{L}} \tag{17a}$$

$$A = V_0 - V_1 = \Delta V \tag{17b}$$

$$B = \left(\sqrt{V_0} - \sqrt{V_1}\right)^2 \tag{17c}$$

$$L = \sqrt{\frac{2}{\mu c^2 \omega *}} \left(\frac{1}{\sqrt{V_0}} + \frac{1}{\sqrt{V_1}} \right)^{-1} \tag{17d}$$

V_0 and V_1 are the "bare" barrier heights for the forward and reverse reactions. μ and ω^* are the frequency and reduced mass of the critical oscillator and c is the speed of light. For these systems, $V_1 < V_0$, therefore the barrier is asymmetric. The Eckart barriers for decarbonylation and H atom loss are shown in Figure 3.8. In this figure, the zero point energies of the molecular ion, transition states, and products are shown as well as the excitation energies of the two different Ar* states.

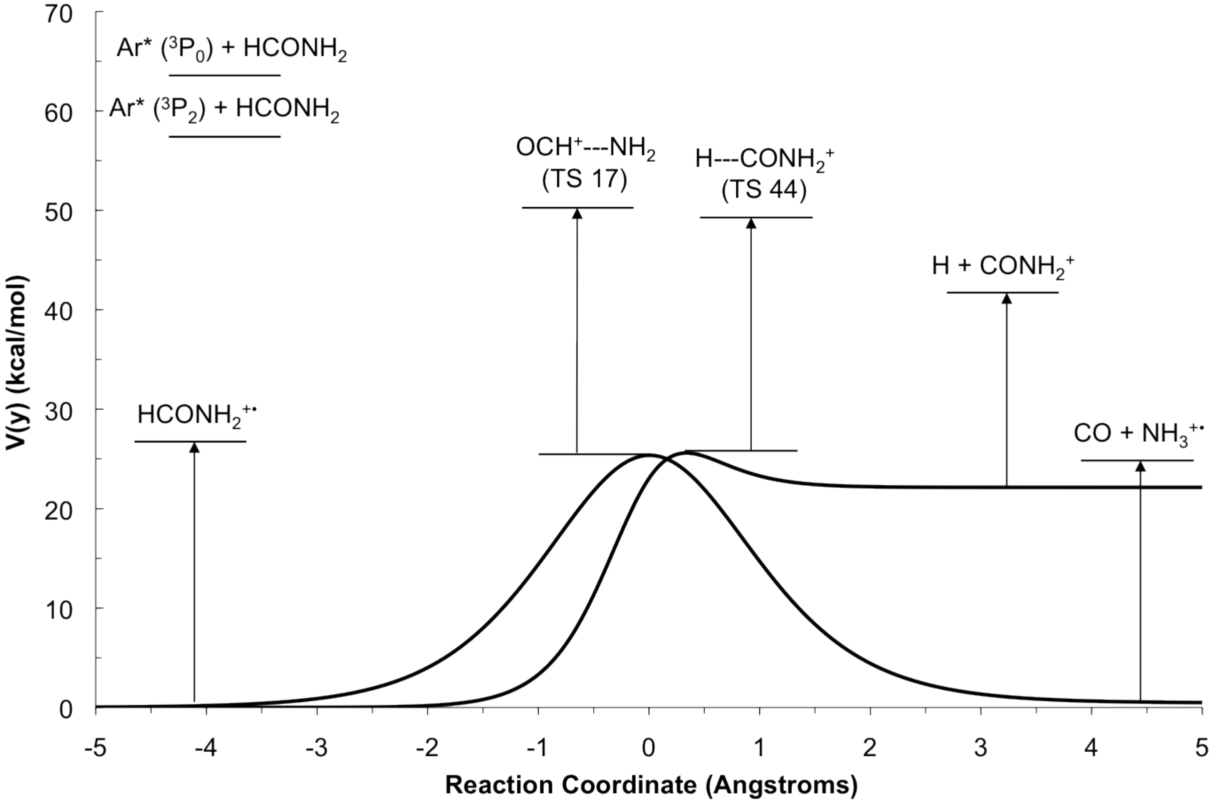

Figure 3.8. Eckart Potentials and zero point energies for the m/z 17 and 44 channels

The tunneling probability may be found by substituting *V(y)* into the Schrödinger equation yielding,

$$P_{tun} = \frac{\sinh(a)\sinh(b)}{\sinh^2\left(\frac{a+b}{2}\right) + \cosh^2 c} \tag{18a}$$

$$a = \frac{4\pi}{\hbar\omega^*}\left[\sqrt{E+V_0}\left(\frac{1}{\sqrt{V_0}} - \frac{1}{\sqrt{V_1}}\right)^{-1}\right] \tag{18b}$$

$$b = \frac{4\pi}{\hbar\omega^*}\left[\sqrt{E+V_1}\left(\frac{1}{\sqrt{V_0}} - \frac{1}{\sqrt{V_1}}\right)^{-1}\right] \tag{18c}$$

$$c = 2\pi\sqrt{\frac{V_0 V_1}{(\hbar\omega^*)^2} - \frac{1}{16}} \tag{18d}$$

In order to calculate the RRKM rate constants for both the tunneling and the non-tunneling cases, a FORTRAN program was used. For the non-tunneling case the Bayer-Swinehart algorithm[75] was used to compute *N(E)*, which adds chunks of states of different energies to come up with total number of states. This algorithm could not be used for the tunneling case; instead the Robinson-Holbrook algorithm[76] was used, which finds each individual state and replaces *H* by P_{tun} for each of them. The code was first tested against a set of examples given by Robinson and Holbrook, Miller's results for formaldehyde decomposition, and the calculations for the propane molecular ion done by MacAdoo *et al.*[50] The resulting RRKM rate constants for hydrogen atom loss and decarbonylation are shown in Figure 3.9.

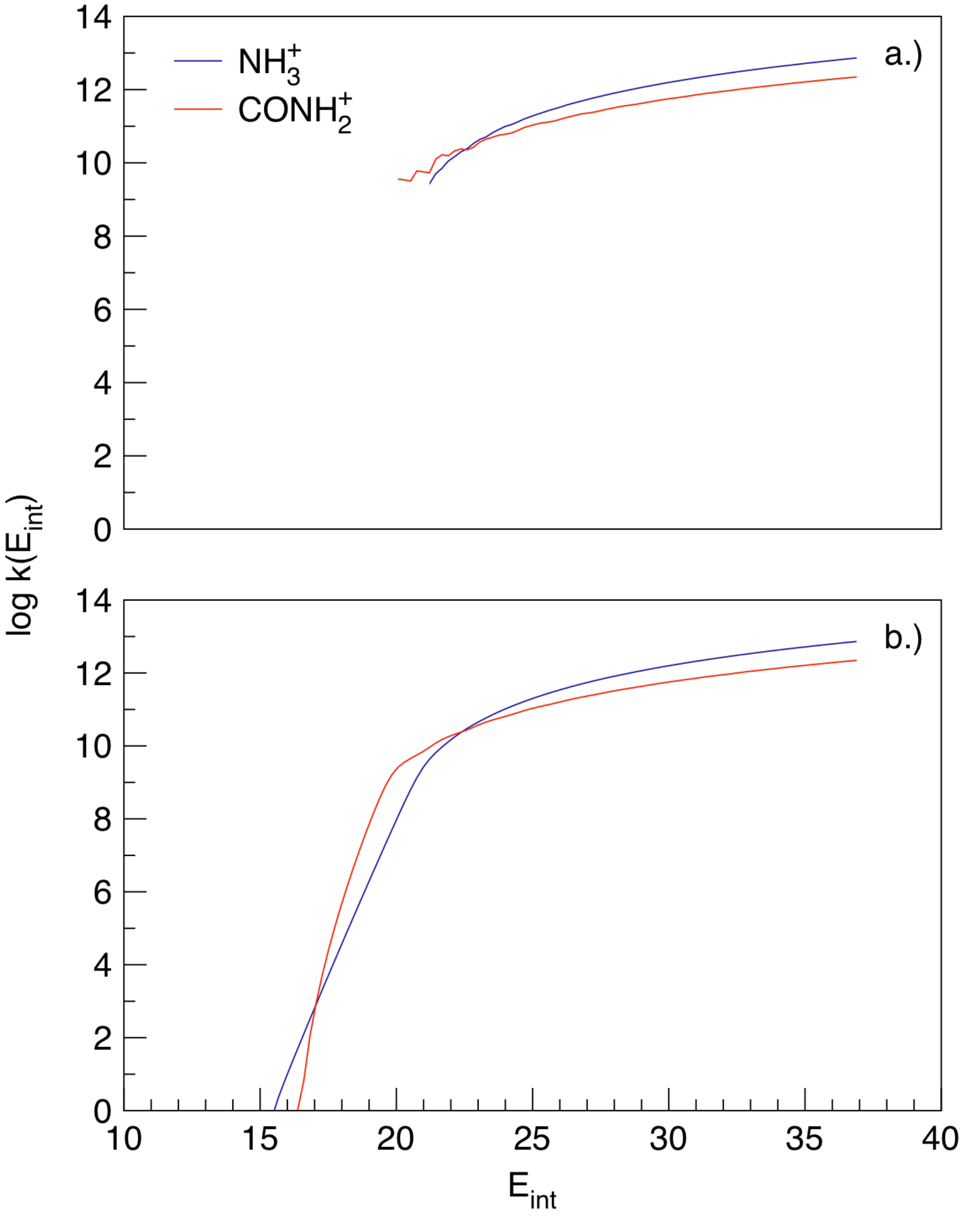

Figure 3.9. Plots of *log (k(E$_{int}$))* vs. *E$_{int}$* for the m/z 17 (blue) and 44 channels. a.) Without the tunneling correction. b.) With the tunneling correction.

The next step is to generate the breakdown graph, which is a plot of the population of an ion as a function of the internal energy. In order to accomplish this, first order loss of P^+ and first order accumulation of D_i^+ is assumed with rate constants k_i for channels $i = 1, n_c$. This results in the following integrated rate equations,

$$[P^+]_t = P^+(0)e^{-kt}, k = \sum_{i=1}^{n_c} k_i \tag{19}$$

$$[D^+]_t = \frac{k_i}{k} P^+(0)(1 - e^{-kt}), i = 1, n_c \tag{20}$$

In order to plot the breakdown graph, $P^+(0)$ is set equal to 1 and a detection time (t) is specified. For these experiments, t was chosen to be 1 μs. The resulting breakdown graphs for both the tunneling and non-tunneling cases are shown in Figure 3.10.

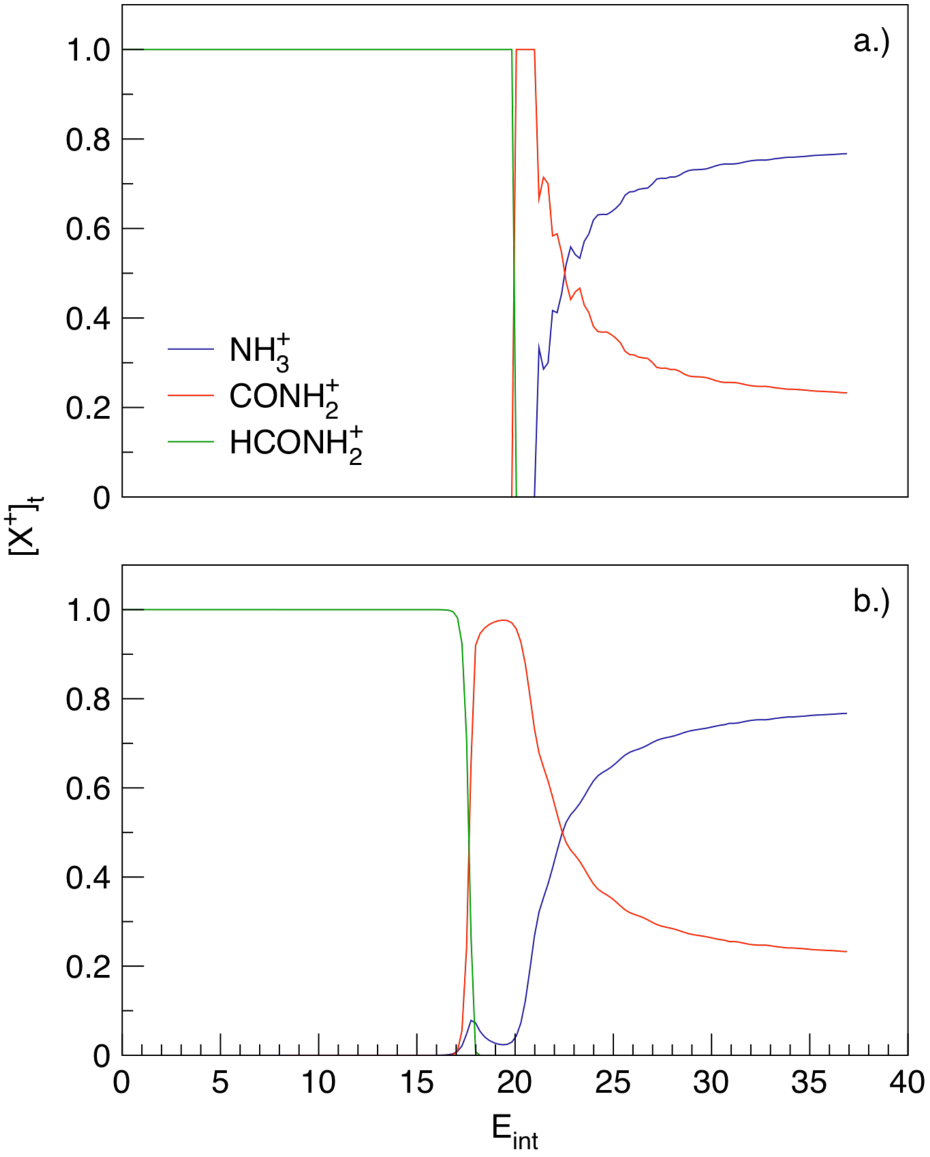

Figure 3.10. Breakdown graphs for Ar* + $HCONH_2$. a.) With the tunneling correction. b.) Without the tunneling correction. Green represents $[HCONH_2^+]_t$, blue represents $[NH_3^+]_t$, and red represents $[CONH_2^+]_t$ in both graphs.

3.6.3 The Energy Deposition Function and Calculated Ar* Spectrum

The breakdown graphs may be converted into mass spectra if the distribution of internal energy ($P(E_{int})$) of P^+ is known. E_{int} is equal to the total internal energy less the zero point vibrational energy. In the field of mass spectrometry, $P(E_{int})$ is known as the deposition function[77]. For electron ionization, the deposition function is typically estimated from photoionization spectra. However, this approximation is quite uncertain since electron ionization mass spectra and photoionization spectra are not collected from similar processes. For Penning ionization, the deposition function can be estimated using the PIES spectrum for the target molecule. Since Penning ionization mass and electron spectra are collected using the same chemical reaction the uncertainty in the estimation of the deposition function is greatly reduced.

For the Penning ionization reaction, the energy conservation relationships may be represented by the following equation:

$$\varepsilon + E_{\text{int}} + E'_{rel} = \varepsilon_0 + E_{\text{int},0} + E_{rel} \tag{21}$$

The terms on the right side of the equation describe the energy of the system before ionization and the terms on the left describe the energy of the system after ionization. E_{rel} and E'_{rel} are the initial and final relative kinetic energy of the metastable noble gas atom and its target species, respectively. $E_{int,0}$ and E_{int} are the initial and final internal energy of the target species, respectively. The kinetic energy of the ejected electron is denoted as ε and ε_0 is equal to the excitation energy of the metastable atom less the ionization potential of the target molecule. All of the energy components are distributed except ε_0; however, the distributions for E'_{rel}, E_{rel}, and $E_{int,\,0}$ are quite narrow and may be approximated by their average values.

Since all of the energy terms are proportionate, the distributions of ε and E_{int} are complementary. Therefore, $P(E_{int})$ can be approximated as the following:

$$P(E_{\text{int}}) = P_{\varepsilon}(\varepsilon = \varepsilon_0 - [\langle E_{\text{int},0}\rangle + \langle \Delta E_{rel}\rangle] - E_{\text{int}}) \tag{22}$$

The average translational energy change $\langle \Delta \mathrm{E}_{\mathrm{rel}} \rangle$ is assumed to be equal to the negative of the PIES peak energy shift. Therefore the peaks in the input PIES spectrum are corrected for this shift. $E_{int,0}$ shifts $P(E_{int})$ to higher energy by the same amount. Since only vibrational states are being considered in these calculations and $HCONH_2$ has one normal mode that has a frequency comparable to k_bT, the computed $\langle E_{int,0} \rangle$ of 0.026 eV provides a small correction.

The PIES spectrum from He* (2^3S) + $HCONH_2$ measured by Keller et al.[65] was used in the approximation of $P(E_{int})$ since it was conveniently partitioned into electronic contributions from high lying molecular orbitals. The PIES spectrum was simulated using a sum of Gaussian functions with heights and widths that best fit the original data. One Gaussian function was used for each electronic state and two additional diffuse functions were used to fill in the valleys between peaks. The simulated PIES spectrum is shown in Figure 3.11.

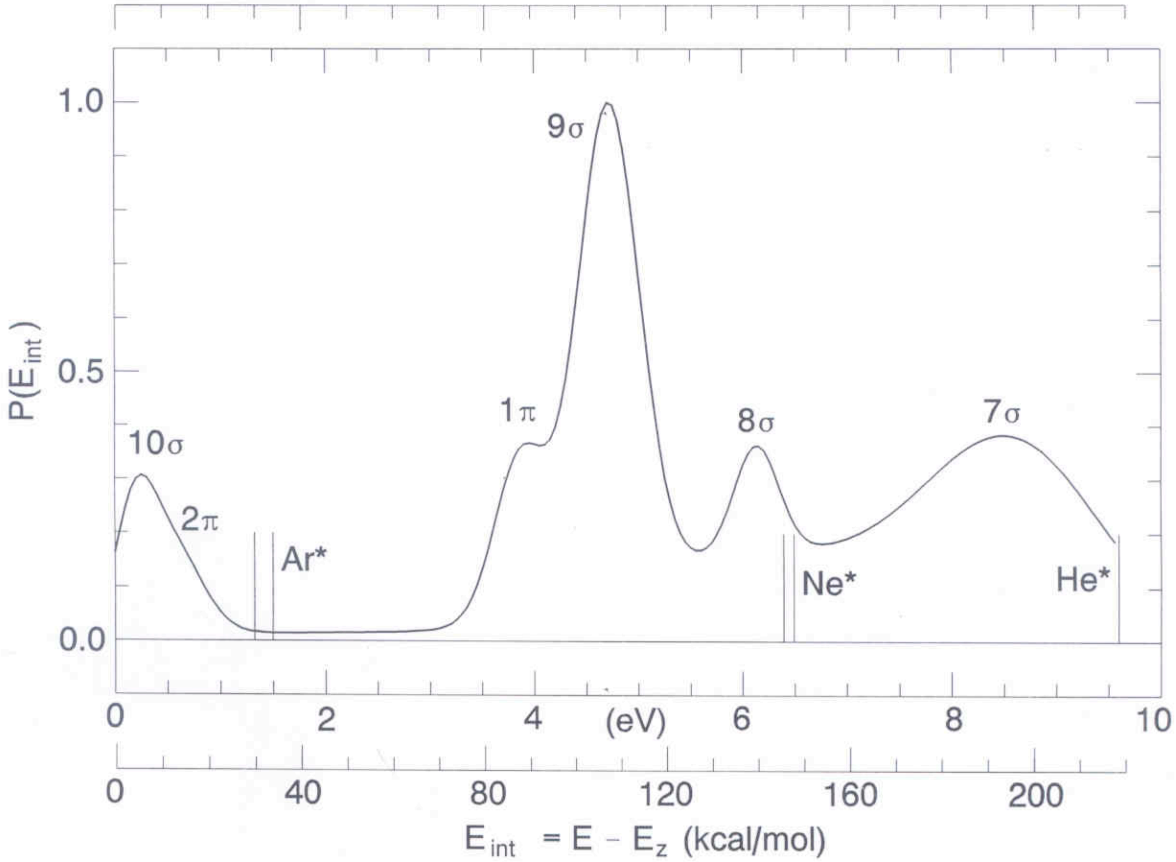

Figure 3.11. Gaussian parameterization of the PIES for He* (2^3S) + HCONH$_2$ from Ref. 65

To use this spectrum for Ar*, it is assumed that the PIES spectrum for Ar* + $HCONH_2$ is identical to the He* spectrum except when it comes to ε_0 which results in the truncation of the spectrum when E_{int} exceeds the available energy. This assumption may seem questionable but there are very few measured PIES for metastable atoms other than He* for any given molecule. However a study of the He* and Ne* PIES for H_2[78-79] show that the spectra are similar except for the energy cutoff in Ne* which occurs in the midst of the H_2^+ (X) vibrational progression. Therefore this assumption may hold for other target species.

The relative abundance ($A(D_i^+)$) of an ion produced from PI with a Ng* beam containing two metastable states of relative population p_k can be calculated using the following equation

$$A(D_i^+) = \sum_{k=1}^{2} p_k \int_{0}^{\varepsilon_{0K}} D_i^+\left(E_{\text{int}} + E_Z\right) P(E_{\text{int}}) dE_{\text{int}} \tag{23}$$

Following this calculation for all ions in the Ar* + $HCONH_2$ spectrum, the abundances were converted to percent ionization. The percent ionizations for the simulated spectra (for both the tunneling and non-tunneling cases) compared to the experimental yields are given in Table 3.5.

Table 3.5. Comparison of theoretical and experimental ion yields.

Channel	m/z	% Yield	
		Theory	Expt.[h]
$HCONH_2^{+\bullet}$	45	88.7 (92.9)	88.6
$H + CONH_2^+$	44	7.1 (3.5)	6.0
$CO + NH_3^{+\bullet}$	17	4.2 (3.6)	5.4

3.6.4 Comparing the Experimental and Theoretical Ar* + $HCONH_2$ Spectra

Ruttink et al. studied the decarbonylation of the formamide radical cation in 1995.[49] It was suggested that as the C─N bond stretches, there is a crossing onto the excited surface of the radical cation. This is possible because the valence molecular orbitals of the formamide radical cation are close in energy. This causes the electron to move from the 10a′ to the anti-bonding π orbital of formamide (3a″). This allows for the NH_2 group to rotate out of the plane of the molecule as the bond stretches. The proton on the carbon atom then transfers to the nitrogen atom forming an ammonia radical cation and carbon monoxide. The structure of the transition state for this pathway is close to that calculated in Ruttink article. Also, as suggested in the Ruttink article, decarbonylation has a slightly lower energy barrier than the hydrogen atom loss.

The closeness of the two barrier heights makes for a competitive fragmentation; whether or not tunneling is included. The channel rates cross twice, once in the tunneling region and

---

[h] Renormalized to exclude the m/z 29 peak

once in the non-tunneling region. The crossing of the rates can be explained by the differences in transition structures. Reactions that do not require molecular rearrangement proceed through "loose" transitions structures. Loose transition structures have internal rotational degrees of freedom not possessed by the reactant molecule and, as a result, have a very low or no barrier for the reverse reaction. Fragmentation pathways that involve direct bond cleavage (such as H atom loss in this system) proceed through loose transition structures. In contrast, reactions that proceed through "tight" transition structures require a certain molecular geometry in order to proceed. The transition structure either has the same or less internal rotational degrees of freedom as the reactant and a well defined reverse reaction barrier. Isomerizations and decompositions proceed through tight transition structures. The decarbonylation of $HCONH_2^{+\cdot}$ proceeds through a tight transition structure.

The threshold energy for bond cleavage reactions is higher than that of rearrangements because a certain amount of energy needs to be deposited into the bond in order to cleave it. Rearrangements have lower threshold energies because the energy required to break the old bond is usually recovered when a new bond is formed. Therefore, *k(E)* for rearrangements approaches the limit more quickly than that for bond cleavage, allowing for the *k(E)* for bond cleavage to "over run" that for rearrangement. This explains the crossing of the rates for H atom loss and decarbonylation in the tunneling region of the plot. However the second crossing does not follow this explanation. This could be due to the barriers for the two pathways being extremely close (within 0.2 kcal/mol). Also, according to the IRC calculation for the decarbonylation reaction, the proton transfer occurs while the C—N bond is cleaving instead of before it, which makes the transition state more "loose" than in a traditional rearrangement reaction. This may also account for the closeness of the *k(E)* expressions for the two pathways. The role of the 3a″

state of the molecular ion in decarbonylation may also prevent *k(E)* from reaching the rate limit quickly and helping it to once again overtake *k(E)* for bond cleavage.

The competition between the pathways is reflected in the breakdown graph, which shows at lower internal energy, the molecular ion dominates. At higher internal energy, both $NH_3^{+\bullet}$ and $CONH_2^+$ begin to appear, however as $[CONH_2^+]_t$ begins to increase $[NH_3^{+\bullet}]_t$ decreases immediately after it appears resulting in a small "hill". However as $[CONH_2^+]_t$ starts to decrease, $[NH_3^{+\bullet}]_t$ begins to increase once again.. The energy deposition function peaks at 5, kcal/mol, where the breakdown graph shows the domination of the molecular ion. The appearance of $CONH_2^+$ and $NH_3^{+\bullet}$ occurs as $P(E_{int})$ is declining. This would correspond to the majority of the ion yield being molecular ion and low yields for the $CONH_2^+$ and NH_3^+ with a slightly higher yield for $CONH_2^+$ since $[CONH_2^+]_t$ peaks in that internal energy range. Integration over $P(E_{int})$ gives the yields 45 / 44 / 17 = 88.7 / 7.1 / 4.2 (92.9 / 3.5 / 3.6 without tunneling). The experimental spectrum reported in Table 3.1 is 88.6 / 6.0 / 5.4. Given the experimental error bars, as well as the inherent error of the CBS-QB3 method[67], the RRKM results agree with the experimental mass spectral results for Ar* + $HCONH_2$. It also shows that approximately 15% of the yield of $NH_3^{+\bullet}$ and 50% of the yield of $CONH_2^+$ can be attributed to tunneling.

3.7 CONCLUSION

In this work, we have presented the first mass spectra from the PI of formamide by He*, Ne*, and Ar*. These spectra show different ion yields when compared to the standard 70 eV EI spectrum for formamide, which can be accounted for by analyzing the dynamics of the PI reaction. The number and identity of observed ions in these spectra depend on the excitation energy of Ng* as well as the ΔE_0 values for the fragmentation channels that include them. We have also calculated the ion yields for the Ar* + $HCONH_2$ spectrum. These yields are in excellent agreement with our experimental yields. RRKM theory also allowed us to determine the fraction of our ion yields that can be attributed to tunneling. Future measurements of these spectra with formamide – d_3 would allow us to experimentally determine how much of the ion yield comes from tunneling. Our plans for future work had included collecting mass spectra for five other amides, systematically growing alkyl chains from the carbonyl carbon and nitrogen atoms and doing similar RRKM calculations for these systems. Preliminary data for Ng* + CH_3CONH_2 are presented in Appendix B. We also had hoped to collect PIES spectra for these systems in order to have more accurate energy deposition functions for ion yield calculations. The calculation of ion yields using unimolecular rate theory is often a difficult task because of the difficulty in obtaining the internal energy distribution for the molecular ion in question. The ease in obtaining the energy deposition function for a molecular ion produced by PI makes this task less daunting. PI mass spectrometry then provides a great venue for the application of RRKM-QET theory to the calculation of ion yields.

4.0 INTRODUCTION TO CHARGE TRANSPORT IN ORGANIC MATERALS

4.1 ORGANIC MATERIALS IN ELECTRONIC DEVICES

The use of organic semiconductor materials in electronic devices is a relatively new idea, gaining a large amount of interest in the early 21st century. However, the discovery that organic materials can conduct electricity is rather old. The earliest report of an organic conductive material was in 1862 by H. Letheby, who obtained a conductive material by oxidizing aniline in sulfuric acid using electrochemistry.[80] Nearly 50 years later, the photoconductivity of anthracene crystals was reported.[81-82] However, it was the discovery that doped polyacetylene was highly conductive[83] that lead to the development of organic electronics as a promising field. This discovery earned the 2000 Nobel Prize in Chemistry.

Electronic devices made from organic materials have several advantages over silicon-based devices. Organic devices can be made at a lower cost; most devices are fabricated by depositing thin films of the organic material from solution or by using inkjet printing. Organic electronics are also very flexible, making them ideal for thin, large area devices. In addition, their optical properties are very useful for solar energy harvesting. Because of these properties, organic semiconductors are being used to make a variety of commercial electronic devices such as thin film transistors,[84-87] organic light emitting diodes (OLEDs),[88-89] and photovoltaics.[90-92]

Organic semiconductors fall into two categories: molecular and polymeric materials. Both types of materials consist of π conjugated systems. Besides molecular weight, the major difference between the two lies in how they are processed to make electronic devices. Thin films of molecular materials can be deposited using sublimation or evaporation techniques while polymeric thin films are often deposited from solution or by using inkjet printing. Figure 4.1 shows some examples of organic semiconductors from each category.

The quantity that is used to characterize charge transport is the mobility (μ). In the presence of an applied electric field, μ can be defined as the ratio between the velocity of the charge carrier (v) and the magnitude of the electric field (E),

$$\mu = \frac{v}{E} \tag{24}$$

Typical values of μ for disordered organic materials range between 10^{-6}-10^{-1} cm^2/Vs.

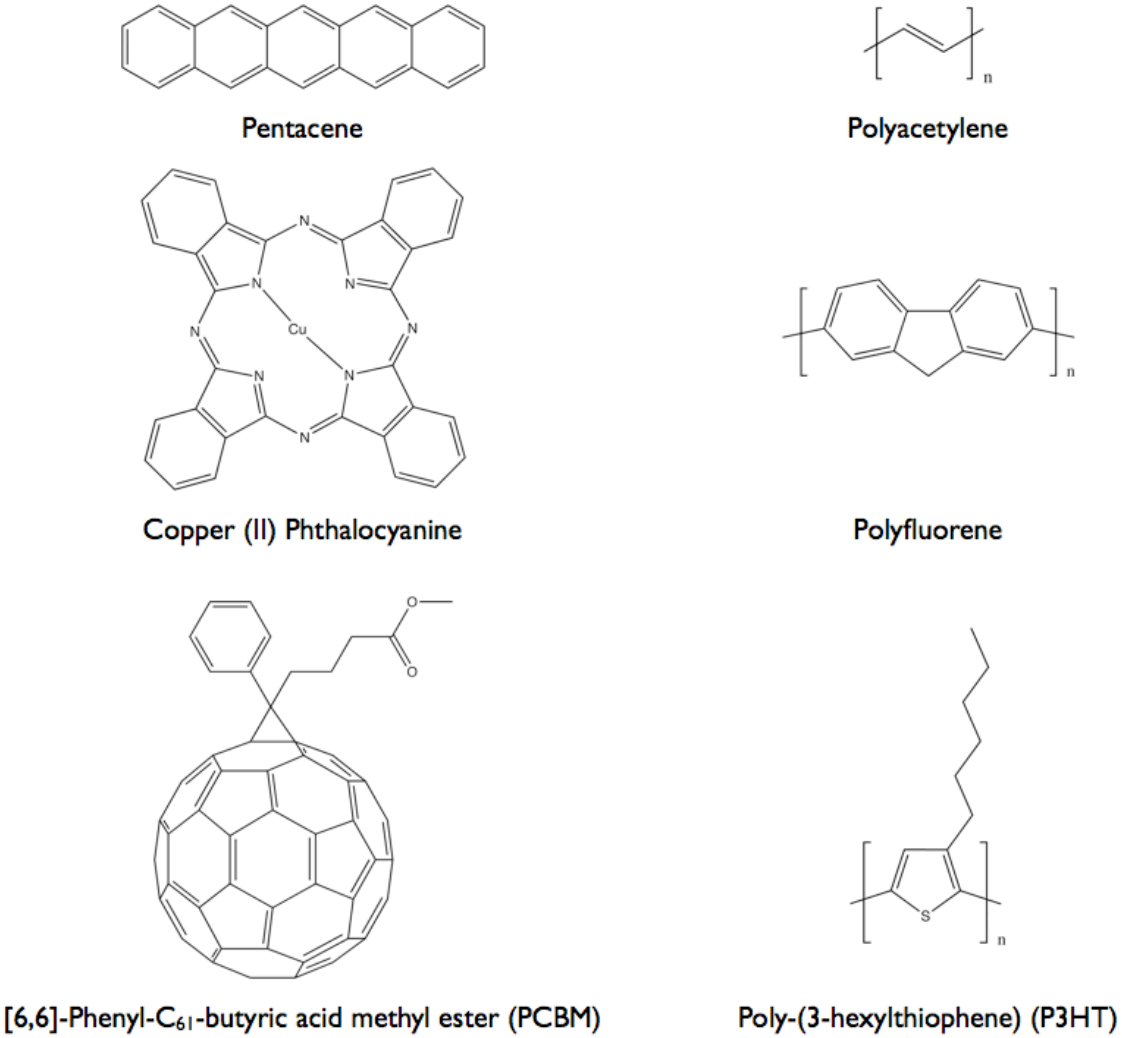

Pentacene

Polyacetylene

Copper (II) Phthalocyanine

Polyfluorene

[6,6]-Phenyl-C_{61}-butyric acid methyl ester (PCBM)

Poly-(3-hexylthiophene) (P3HT)

Figure 4.1. Examples of common organic semiconductors. Molecular materials are on the left and polymeric materials on the right.

4.2 CHARGE TRANSPORT MODELS

The mechanism of charge transport in organic semiconductors tends to fall in-between two extremes: band and hopping transport. Band transport occurs at low temperatures in highly pure, crystalline organic materials. The valence band is formed from the combination of the highest occupied molecular orbitals (HOMOs) of all molecules in the crystal while the conduction band is formed from the combination of the lowest unoccupied molecular orbitals (LUMOs). The width of the valence and conduction bands is equal to $4H_{ab}$ for an infinite 1D crystal where H_{ab} is the electronic coupling matrix element. This is similar to band transport in metals and inorganic semiconductors, however due to weak van der Waals interactions, bandwidths in organic materials are typically very narrow, resulting in lower carrier mobilities.[93]

In amorphous organic materials, the high amount of disorder combined with weak electronic interactions cause band states to localize on individual molecular sites. Consequently, charge transport occurs through a thermally activated hopping mechanism. Hopping transport in disordered organic materials can be described using variable range hopping (VRH), which was first described by Mott[94]. In VRH models, the hopping rate depends on both the energy difference and distance between two molecular sites. There are two commonly used expressions for the hopping rate. The Miller-Abrahams rate[95] is given by,

$$k_{ij} = \nu_0 \exp\left(-2\gamma R_{ij}\right) \begin{cases} \exp\left(-\dfrac{\varepsilon_j - \varepsilon_i}{k_B T}\right), & \varepsilon_j > \varepsilon_i \\ 1, \quad \varepsilon_j < \varepsilon_i \end{cases} \tag{25}$$

Here, v_0 is the "attempt to hop" frequency, γ is the overlap factor, R_{ij} is the distance between sites and ε_i and ε_j are the energies of sites i and j respectively. The Miller-Abrahams expression allows for "long distance" hops between molecular sites with similar energies due to the presence of the two exponential terms.

A more realistic expression for the hopping rate for disordered organic materials comes from Marcus-Hush theory[96],

$$k_{ij} = \frac{2\pi\langle H_{ab}\rangle^2}{\hbar}\frac{1}{\sqrt{4\pi\lambda k_B T}}\exp\left(-\frac{(\varepsilon_j - \varepsilon_i + \lambda)^2}{4\lambda k_B T}\right) \tag{26}$$

In this expression, λ is the total reorganization energy that is associated with the geometric change that accompanies the charge transfer process (see Figure 4.2). If entropic contributions are neglected, the energy difference (ε_j - ε_i) can be approximated as the free energy change (ΔG). The Marcus-Hush expression predicts a maximum rate when $\Delta G = -\lambda$, which is the well-known Marcus "inverted region".[97]

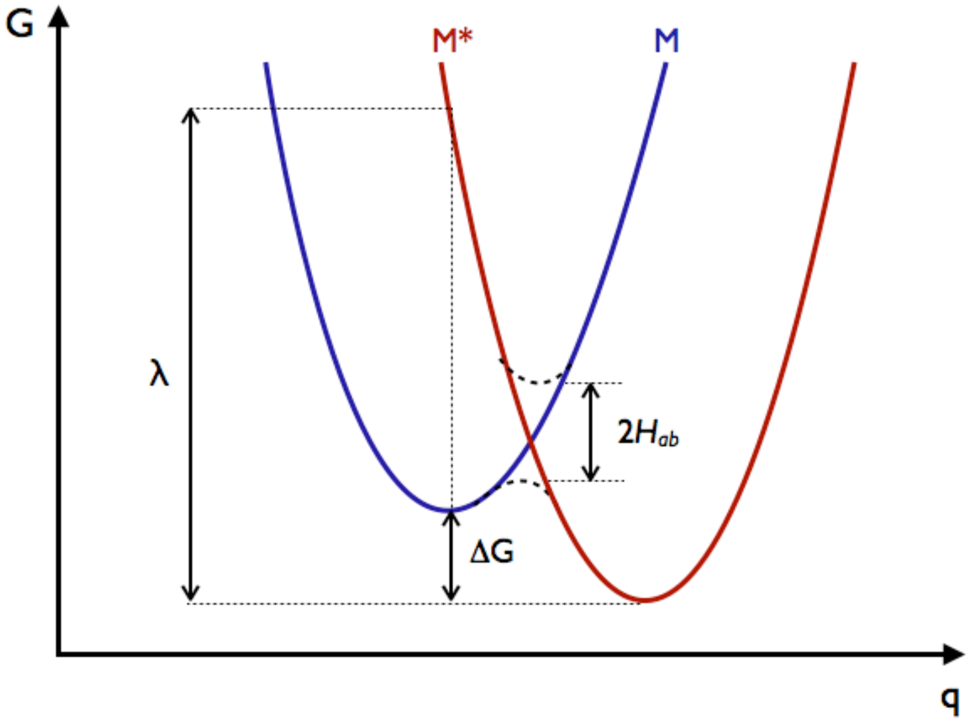

Figure 4.2. Potential energy profile for an electron transfer reaction. *G* represents the Gibbs free energy and *q* represents the reaction coordinate

Both rate expressions are dependent on temperature however the Miller-Abrahams rate is useful for low temperatures while the Marcus-Hush rate is used for high temperatures. Also, the effects of an applied electric field can be incorporated into the rate expressions by adding an additional term to the exponential terms containing the site energy difference. This is useful for studying organic electronics such as transistors or OLEDs, where an electric field is applied to lower the hopping barrier for charge carriers.

4.3 COMPUTER SIMULATIONS OF CHARGE TRANSPORT IN ORGANIC SEMICONDUCTORS

Computer simulations, in particular those that use Monte Carlo (MC) methods have proven very useful in studying charge transport in disordered organic semiconductors. The most common MC simulation method uses the Gaussian Disorder Model (GDM), which was developed by Bässler[98] to model hopping transport in disordered organic solids. The GDM takes the site energy (ε) from a Gaussian distribution of energies,

$$g(\varepsilon) = (2\pi\sigma^2)^{-1/2} \exp\left(-\frac{\varepsilon^2}{2\sigma^2}\right) \tag{27}$$

Here σ is the standard deviation of the distribution and ε is measured relative to the center of the distribution. A Gaussian distribution is used, mainly because it approximates the shape of absorption bands for organic materials. The hopping rate that is used in the GDM is the Miller-Abrahams rate. The overlap parameter (2γ) is also chosen from a distribution to account for its dependence on site orientation as well as the changes in the distance between sites due to disorder.

MC simulations that use the GDM have been used mainly to study the temperature and field dependence on the carrier mobility in disordered organic materials. For disordered materials, hopping is thermally activated and higher temperatures improve the carrier mobility. In some cases, the temperature dependence on the mobility follows an Arrhenius-type expression,[99-100]

$$\mu \propto \exp\left(-\frac{E_a}{k_B T}\right) \tag{28}$$

where E_a is the activation energy, which increases as the amount of disorder increases. A number of simulations that use the GDM have found that the temperature dependence follows a slightly different expression[101-103],

$$\mu \propto \exp\left(-\frac{T_0}{T}\right)^2 \tag{29}$$

Here, T_0 describes the amount of disorder in the system. There is no theoretical explanation for either of these expressions, however both fit experimental data rather well.[104-105]

The applied electric field allows for charge carriers to overcome hopping barriers due to charge traps. MC simulations have found that the mobility depends on the square root of the electric field as follows,[106-107]

$$\mu \propto \exp\left(\gamma_T \sqrt{E}\right) \tag{30}$$

Here, γ_T is a temperature dependent parameter. This is known as Poole-Frenkel behavior and is usually observed experimentally at field strengths between 10^4-10^6 V/cm.[108-111] At lower field strengths, the mobility is roughly constant.

The effects of charge traps have also been studied using the GDM and MC simulations.[112] Traps are modeled by introducing a second Gaussian distribution for the energies of trap sites that is offset from the center of the "normal" hopping site energy distribution by the depth of the traps. This model has been used to simulate the mobility as a function of trap concentration. In addition, temperature and field dependences on mobility were studied in the presence of traps at various concentrations. The simulation results agree with experimental behavior[113-114] and have been described using an effective medium theory.[115-116]

4.4 RESEARCH DESCRIPTION

The next three chapters of this dissertation describe computational work done in order to understand charge transport in electronic devices made from semiconductors. The first two chapters describe course grained MC simulations of charge transport through a model monolayer organic field effect transistor (OFET). These studies are focused on understanding the effects of defects, traps and electrostatic interactions on charge carrier mobility. The simulation model that is being used differs from many of those in the current literature in that Gaussian disorder is not assumed. Instead, disorder is introduced by explicitly adding defect or trap sites. Chapter 5 is focused on the effects on unreactive defects and electrostatic interactions while Chapter 6 focuses on the effects of charge traps.

The third chapter takes a look at one of the major assumptions made in existing VRH models; that charge carriers in disordered organic materials are localized on individual molecular sites. This is studied by performing two sets of quantum chemistry calculations on a series of positively charged bithiophene clusters. Constrained density functional theory (CDFT) calculations were used to force a single positive charge on a molecule in the cluster. The HOMO energies from these calculations were compared to those calculated with standard DFT, which allows the charge(s) to delocalize throughout the entire cluster. The effects of electrostatic interactions on the ability for a molecular site to localize a charge were also examined.

5.0 CHARGE TRANSPORT IN IMPERFECT ORGANIC FIELD EFFECT TRANSISTORS: EFFECTS OF EXPLIT DEFECTS, AND ELECTROSTATICS[i]

5.1 INTRODUCTION

Although many experimental and theoretical studies have given into the effects of electric field and temperature on charge transport in organic semiconductors, the exact roles of defects are not always well understood.[118-121] In contrast to inorganic semiconductors, it is more difficult to remove defects from organic semiconductors used in electronic devices; both chemical and physical impurities are inevitable. In addition, some applications, such as OLEDs and organic photovoltaics, require charge transport through mixed films (i.e., high "defect" concentrations). Therefore, a detailed understanding of how defects influence charge transport in these materials is required.

Defects in organic semiconductor devices take a number of forms. Most of them arise from the fabrication of the device, which typically involve the deposition of single or multiple layers of the organic semiconductor of choice to form thin films. Solvent molecules and/or other chemical impurities may become trapped in the film, where they can act as electron or hole traps, hindering charge transport.[122-123] It is also difficult to form ordered films of organic semiconductors, especially in the case of polymeric materials. The underlying silicon-dielectric

---

[i] Based on published work[117]

layer can also have a variety of pinhole charge defects, which would influence the organic semiconductor on top.[124-125] As a result, the charge mobility in organic semiconductors is often much lower than in crystalline inorganic semiconductors, and in contrast to inorganic semiconductors; some categories of defects are intrinsic.

To study how molecular defects affect charge transport, the identity of the defects needs to be known to determine the parameters that govern the hopping rate. In most cases, the identities, quantities, and electronic properties of impurities in semiconductor films are at least partially unknown. Therefore, experimental and theoretical studies to identify defects, or to intentionally manipulate them, are important steps in understanding the fundamental mechanisms of charge transport.

Very few studies of FET devices include the effects of Coulomb interactions between the charge carriers, or between carriers and charged defects.[99, 126-127] This is not possible to study experimentally, and is often excluded from theoretical studies since including these interactions is computationally taxing, although some previous work has addressed Coulomb effects in other types of transport.[128-130] However, as illustrated in recent literature,[126] there are several reasons why the inclusion of Coulomb interactions are important for understanding charge transport in organic materials. First, because charge carriers in these materials are assumed to be localized on individual molecular sites, they can be regarded as point charges. Secondly, the dielectric constants for most organic materials tend to be small, and Coulomb interactions are long range, so both the applied field in an FET device and the electric field due to the charge carriers significantly affect local charge transport. Finally, charge carrier densities near the semiconductor-insulator interface of organic FETs are large so the average distance between charge carriers will be small. As the potential energy due to electrostatic interactions increases with decreasing distance, the electric field from Coulomb interactions will play an even larger role in charge transport. For these reasons, it is crucial to include Coulomb interactions in theoretical studies of charge transport in organic semiconductors, as we will show.

In this chapter, we discuss the effects of explicit defects on charge transport in imperfect FET devices made with metal phthalocyanines, which our group is currently studying experimentally. To this end, we use Monte Carlo (MC) dynamics to examine the theoretical effects of defects on transport mechanisms. Experimentally, we add known defects to our semiconductor films; in this work we are using nickel (II) phthalocyanine (NiPc) with arbitrary unreactive defects where the concentration of the defects will be controlled. We have "frozen out" the commonly used approximation of Gaussian disorder of site energies (which implicitly treat the effects of defects) in favor of exact interactions with explicitly included defect sites. We will address the effect of defects on charge transport, as well as whether the Gaussian disorder model reflects the correct statistics of explicit defects. We will also look at how the inclusion of Coulomb interactions significantly affects the dependence of charge transport on the source drain voltage (V_{SD}), as well as defect and carrier concentrations.

5.2 COMPUTATIONAL METHODS

As discussed in Section 4.2, charge transport in organic semiconductors is assumed to occur through some form of variable range hopping that is based fundamentally based on a bimolecular charge transfer step. Many studies use the Miller-Abrahams charge transfer rate [99, 126-127, 131] for simulations of charge transfer in organic materials, here we use the Marcus-Hush rate,[132-138]

$$k_{et} = \underbrace{\frac{2\pi\left\langle H_{ab}\right\rangle^{2}}{\hbar}}_{\text{coupling}} \underbrace{\frac{1}{\sqrt{4\pi\lambda k_B T}}}_{\text{reorganization}} \underbrace{e^{\frac{-\left(\lambda+\Delta G^{0}\right)^{2}}{4\lambda k_B T}}}_{\text{activation barrier}} \tag{31}$$

where ΔG^0, H_{ab}, and λ are the difference in energy between molecular sites, the electronic coupling matrix element between the orbitals involved, and the total reorganization energy of the reaction. H_{ab} has been shown to be dependent on the intermolecular distance, making Equation 31 an example of variable range hopping.[137, 139-140] The reorganization term describes the classical density of states and the exponential term describes the population of molecules that posses the energy required to traverse the electron transfer barrier[141]. In principle, ΔG^0, H_{ab}, and λ can be calculated from first principles quantum calculations, and used in our coarse-grained MC dynamics model to simulate electron transport through a thin film. As stated earlier, this presents the opportunity to directly compare the results from these computational studies (with no free parameters) with experimentally obtained results to directly validate the variable-range hopping model. The use of first principles quantum chemistry, in particular density functional theory, to calculate the parameters of k_{et} and use them to explain experimental charge transport results has been demonstrated in the literature. [132-138]

We have calculated orbital energies, H_{ab}, and λ using density functional theory[117] with the B3LYP functional[142-143] and the Lan2DZ basis set and effective core potentials[144-147] as implemented in Gaussian 03[148]. In this work, we considered hole transport through a film of copper (II) or nickel (II) phthalocyanine. Our results imply an intrinsic charge transfer step of ~1 ps. However, the exact charge transfer rate only affects the electrical currents computed by our model (i.e., a systematic scaling factor) and not the trends discussed in the following sections

Since our goal is to provide a direct comparison between experimental and theoretical results, our simulation code has been written to be scalable to large grids via multithreading. In this work, we consider a finite conducting channel of 256x1024 sites. Our grid spacing is ~1 nm and is based on the size if the phthalocyanine molecules. Consequently, our model considers a monolayer OFET with a width of 0.25 μm and a length of 1.02 μm. This is slightly smaller than typical OFETs, however it provides essentially a 1:1 correspondence between grid sites and individual molecules.[149]

Our code has been written in an object-oriented manner, to facilitate explorations of different types of molecular sites (e.g., neutral and charged defects, mixtures of semiconducting molecules, short and long-lived traps, etc). This design also takes full advantage of multi-core clusters, scaling well to dual cores without Coulomb interactions, and quad cores or more when Coulomb interactions were calculated. A square lattice was assumed for the film, and each site was considered to have at most four nearest neighbors, as shown in Figure 5.1.

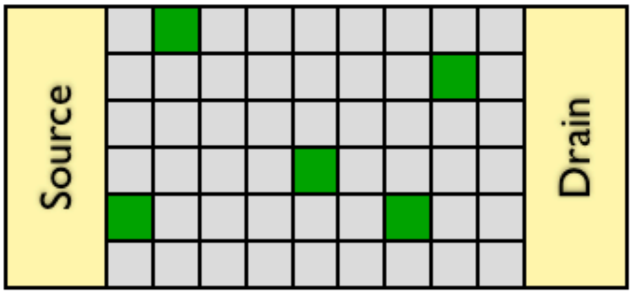

Figure 5.1. Schematic of a charge transport grid for our simulation, where green sites indicate defects.

As with many MC simulations, the initial conditions of the system have a large effect on its behavior. At the beginning of each simulation, the charge density is set to a constant, however there are two ways to achieve the desired charge concentration: random seeding of the system to the desired concentration or injection of charges from the source into the system until the desired concentration is reached (i.e., “warm-up”). The former is much faster and more likely to represent the system at equilibrium. Both methods were explored and are discussed in Section 5.3.1.

For each time step in the simulation there is a serial phase in which calculations on the overall state of the system are performed, and a parallel phase where the agents consider their local neighbors. The majority of the computational time is spent on the latter. This approach allows for the execution of multiple agents (one per core normally) across the entire grid. As illustrated in Figure 5.2, a charge carrier (or “agent”) will consider the surrounding neighborhood when considering potential moves. . The potential energy difference between the current site and neighbors is computed, optionally including Coulomb interactions. A charge cannot move to a site that is already occupied.

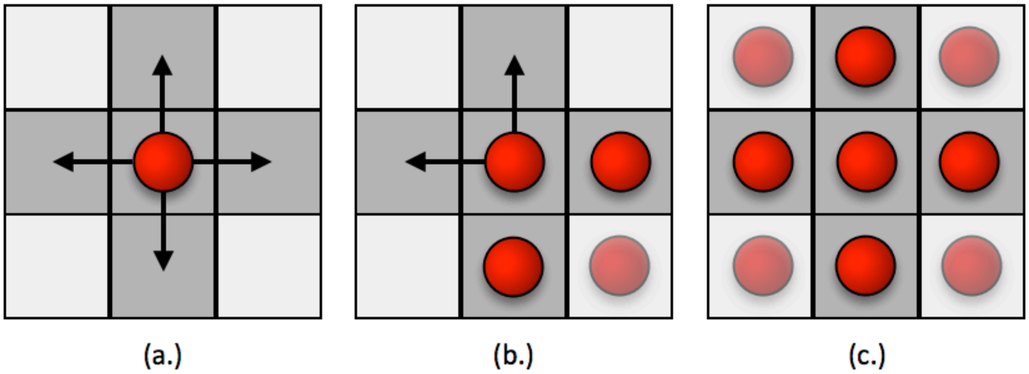

Figure 5.2. Local environment of a charge carrier (red spheres)**.** Each carrier considers 4 sites (dark gray) when deciding on a move. (a) All possible sites are "open". (b) Two sites are occupied by carriers and the electric field of the carrier in the light gray square affect the potential move. (c) All neighboring sites are occupied by agents, and all moves are blocked.

Prospective moves to sites with lower potential energy were accepted one third of the time. This enforces some probability of the carrier remaining on a site. For prospective moves to sites with higher potential energy, the following Boltzmann probability was calculated:

$$P(\Delta E_{pot}) = p_{tm} e^{-\frac{\Delta E_{pot}}{kT}} \tag{32}$$

Here, ΔE_{pot} is the potential energy difference between the two sites, p_{tm} is the transmission probability (1/3), T is the absolute temperature (300K), and k is the Boltzmann constant. The move is accepted if $P(\Delta E_{pot})$ is greater than a generated random number. If the charge landed on the drain electrode, it was always removed from the grid.

It was necessary to employ a cutoff when calculating Coulomb interactions to scale to larger systems. The cutoff distance was set to 50 nm after examining Coulomb pair potentials as a function of distance. In test simulations this cutoff produced comparable numerical results to those performed without any such cutoff. A relative permittivity of $3.5\varepsilon_0$ was employed for the phthalocyanine films, comparable to literature values.[150-151]

5.3 RESULTS AND DISCUSSION

First, we will discuss the two methods of adding charges to the simulation grid (warm up and seeding) and compare them. Second, the simulation of the current as a function of the source drain voltage (V_{SD}) will be compared to experimental measurements for real FET devices. Next will be a discussion of the simulation of the current as a function of V_{SD} when electrostatic interactions are included and in the presence of neutral defects. The simulation of the current as a function of neutral defect and carrier concentration will then be discussed. The simulation of current as a function of charged defect concentration will then be discussed. Finally the effects of Coulomb interactions on charge transport in our simulations will be addressed.

5.3.1 Grid Charging Methods: Charge Injection vs. Random Seeding

As mentioned in the previous section, our simulation code has two methods for placing charges on the FET grid. The "warm-up" method injects charges from the source electrode until the desired charge concentration is reached. Figure 5.3 demonstrates that I_{SD} increases as the simulation progresses and reaches its equilibrium state after 1000 ns (1,000,000 time steps) when electrostatic interactions are not included and 500 ns (500,000 time steps) with electrostatic interactions. At the beginning of the simulation, the carrier density is very high near the source electrode. Without electrostatic interactions, carrier mobility is diminished since carriers cannot "hop" to sites that are already occupied (the site exclusion effect). However, when including Coulomb interactions, the potential energy due to electron-electron repulsion will be very high near the source electrode at the beginning of the simulation. This provides an added Poole-Frenkel-like mobility. In addition, there is a lateral electric field associated with the front of charge carriers, which will also drive carriers across the grid.[152] At the start of the warm-up procedure, this amounts to a potential of approximately 5.8 mV across a 1 μm channel. In short, simulations ignoring Coulomb interactions suggest an unrealistically long "turn-on" timescale.

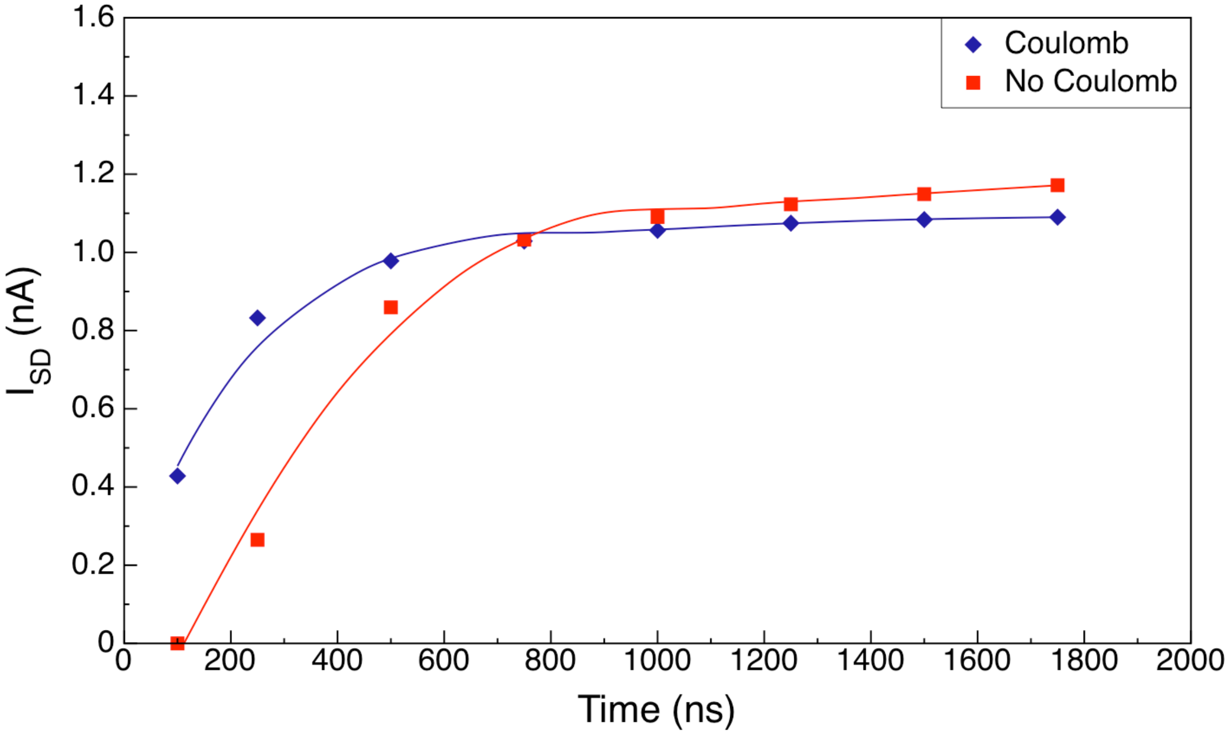

Figure 5.3. I_{SD} vs. simulation time from one representative simulation. Adapted from Figure C.1 in Appendix C.

As shown in Figure 5.3, equilibration takes a long time when the warm up method is used. The alternative to this is to randomly seed the grid with charge carriers. In contrast to the warm-up method, random seeding takes a shorter time to reach equilibrium. This allows us to use a smaller number of iterations for each data point, decreasing the total simulation time. The plots in Figure 5.4 show that the results are similar for both methods at equilibrium. Therefore, unless otherwise indicated, random seeding has been used in our calculations.

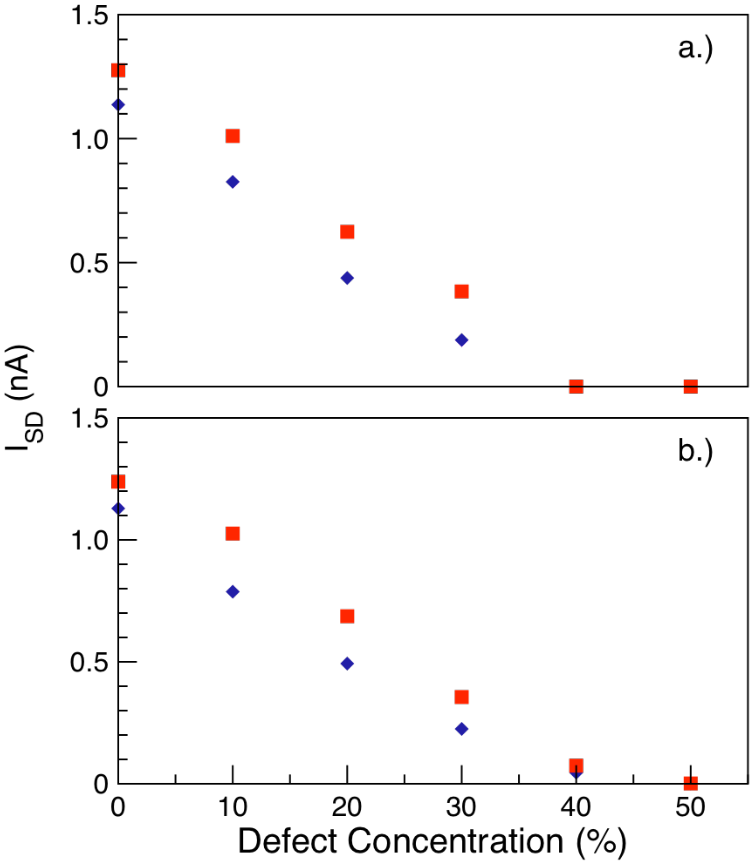

Figure 5.4. Comparison of grid charging methods. Shown are plots of I_{SD} vs. defect concentration resulting from simulations using a.) The warm-up procedure (after 1, 750, 000 iterations) or b.) Random seeding (after 50,000 iterations).

5.3.2 Field dependence of charge transport (ignoring electrostatics or defects)

To compare our model with experiment, simulations of source-drain current (I_{SD}) as a function of V_{SD} were performed at various carrier concentrations. The results of these simulations are shown in Figure 5.5. These results are similar to experimentally measured *I-V* curves for FETs;[153-155] I_{SD} increases as a function of V_{SD} and saturates at high V_{SD}. I_{SD} also increases as the carrier concentration is increased. The carrier concentration can be related to the voltage applied between the source electrode and gate (V_{SG}) in real FET devices.[99] Higher V_{SG} allows more charge carriers to be introduced into the semiconductor film, which results in a higher I_{SD}.

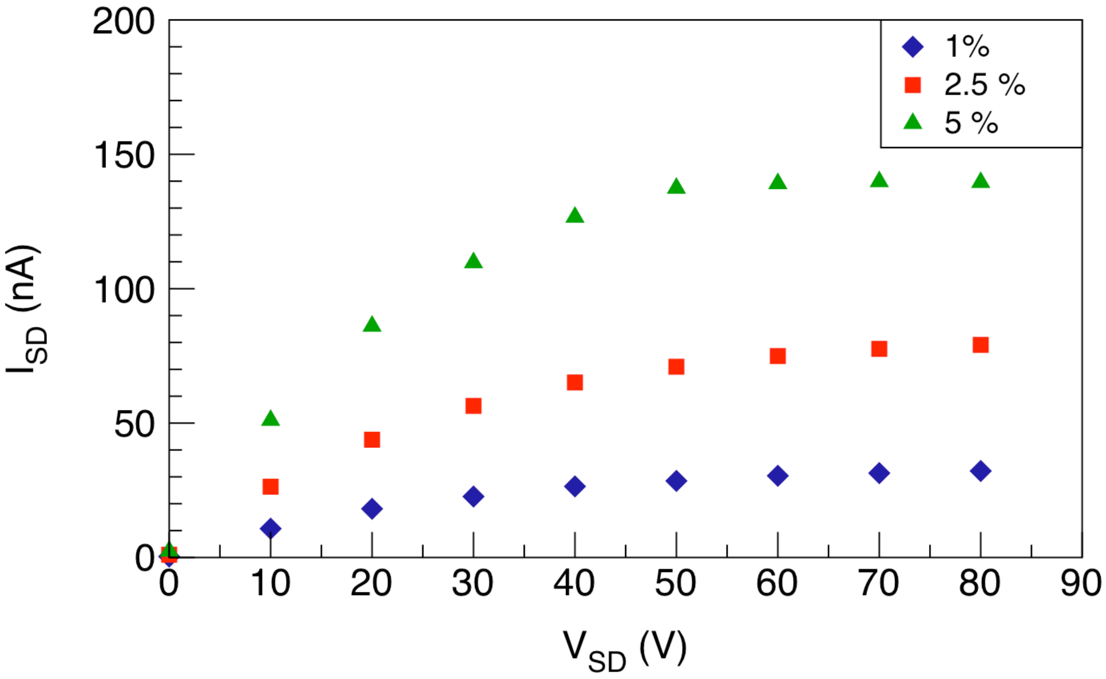

Figure 5.5. I_{SD} vs. V_{SD} at different carrier concentrations.

There are two ways to model the *I-V* curves. The first method is to use a standard equation derived for inorganic FETs, which fits the region of the curve where $V_{SD} < V_{SG}$ to a linear expression[87]. However, this does not take the variation in charge density along the conduction channel into account. Including this effect transforms the linear expression into a quadratic expression for I_{SD} when $V_{SD} < V_{SG}$[156].

$$I_{SD} = \frac{\mu\varepsilon W}{LD}\left[(V_{SG} - V_0)V_{SD} - \frac{V_{SD}^2}{2}\right] \tag{33}$$

Here, ε is the permittivity of the dielectric, D is the thickness of the dielectric, V_0 is the threshold voltage, and W and L are the width and length of the conduction channel respectively. This expression describes the region near the saturation region of the curves more accurately. The mobility (μ) can be calculated from Figure 5.5 and Equation 25. When $V_{SD} > V_{SG}$, I_{SD} is independent of V_{SD} and the I-V curve saturates. To account for this using Equation 25, V_{SD} is set equal to $V_{SG} - V_0$. Taking the square root of I_{SD} yields the following linear equation,

$$\sqrt{I_{SD}} = \sqrt{\frac{\mu\varepsilon W}{2LD}}(V_{SG} - V_0) \tag{34}$$

The mobility may be obtained from the slope of a plot of $\sqrt{I_{SD}}$ vs. V_{SG}, where V_{SG} can be determined for each carrier concentration using the following equation,[99]

$$V_{SG} = \frac{eND}{\varepsilon A} \tag{35}$$

N is the number of charge carriers, which may be calculated from the carrier concentration, A is the area of the device and e is the elementary charge. Our model FET device has a width and length of 256 nm and 1024 nm respectively. For our experimental FETs, the dielectric material is SiO_2 , so $\varepsilon \approx 4\varepsilon_0$ and $D = 300$ nm. For carrier concentrations of 1%, 2.5%, and 5%, V_{SG} is 15.7 V, 39.3 V, and 78.6 V respectively. Using these parameters, μ was calculated to be 6.14×10^{-3} cm^2/Vs, in outstanding agreement with the experimental value for NiPc ($\mu = 8.9 \times 10^{-3}$ cm^2/Vs)[84], demonstrating the success of our model and assumptions.

The results presented in Figure 5 reflect devices with no defects present in the film. It should also be noted that the *I-V* curves that result from simulations that include electrostatic interactions do not appreciably differ from those shown in Figure 5.5 when no defects are present. However, this is not the case when defects are present in the film.

5.3.3 Field dependence of charge transport in the presence of electrostatic interactions and neutral defects

Figure 5.6a shows the results of the simulation of *I-V* curves when the neutral defect concentration is 20% at low V_{SD}. These results show that the current is slightly lower when electrostatic interactions are included, because of surface trapping at the edges of the channel. As electrons are introduced to the film, electron-electron repulsion forces them to migrate to the sides of the film rather than to the drain electrode (i.e. an effect not explicitly included in our code). Eventually, a narrow conduction channel is formed and electrons are able to migrate to the drain electrode, resulting in lower current. Surface trapping is more pronounced at lower V_{SD} since the electrical potential of the charge carriers are more competitive in this case, whereas at high V_{SD}, surface trapping is more easily overcome.

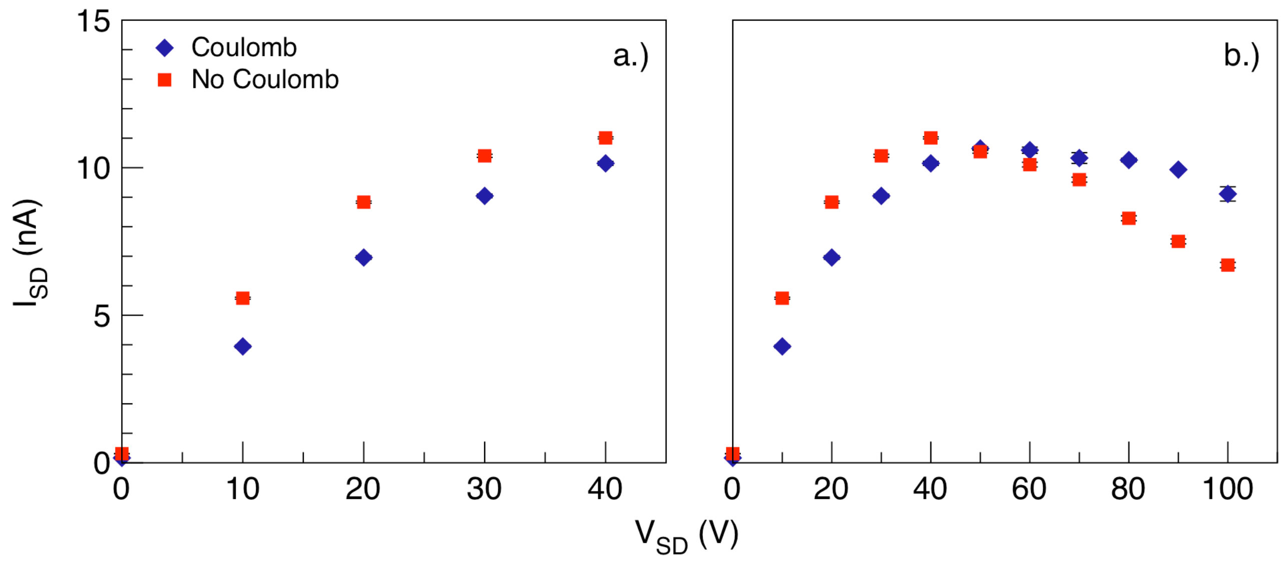

Figure 5.6. I_{SD} vs. V_{SD} with 20% defects a.) at low V_{SD} and b.) extended to high V_{SD}. Note that error bars are included for all points but may be smaller than the symbol.

Figure 5.6b shows the same *I-V* curves extended to high V_{SD}. When Coulomb interactions are not included in the simulation. I_{SD} reaches a maximum and then decays at high V_{SD}. This behavior is indicative of negative differential resistance (NDR), which is when the slope (resistance) of a region of an *I-V* curve for a device is negative. To our knowledge, NDR has not been observed in experimental measurements of *I-V* curves for microscale organic FETs.

At high V_{SD}, the charge carriers are more likely to follow a linear trajectory, directly from source to drain, and will be more likely to “pile up” in a line behind a defect or occupied site, decreasing current. If electrostatic interactions are included, I_{SD} is predicted to saturate (within error bars) at high V_{SD}. Since repulsive interactions between the charges give them a better ability to “avoid one another”, charge transport is correctly predicted to continue at high V_{SD}, as illustrated in Figure 5.7.

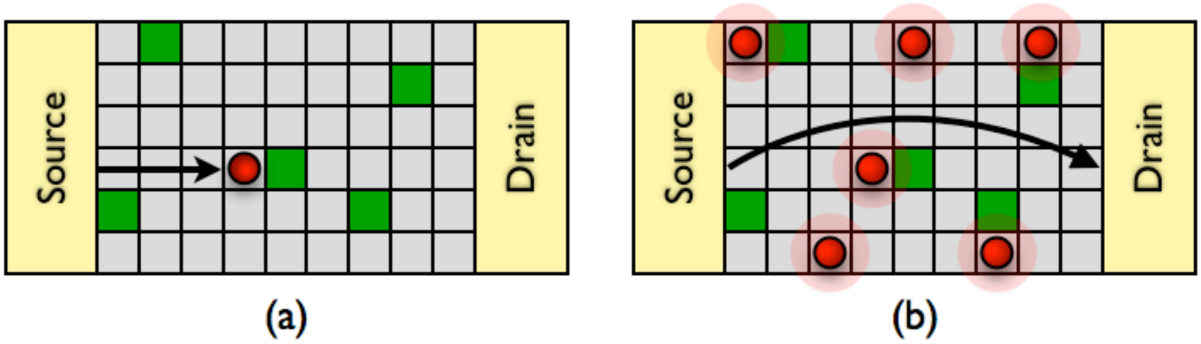

Figure 5.7. Charge transport in an FET with defects (green) for (a) Non-interacting charges and (b) interacting charges (bright red).

5.3.4 Effects of defect and carrier concentration on charge transport

Figure 5.8 shows the results of the simulation of I_{SD} as a function of defect concentration. Regardless of the inclusion of Coulomb interactions, I_{SD} decreases roughly linearly as a function of the neutral defect concentration, and approaches zero at ~50%. In our current simulation results, defect sites do not accept charge carriers, which could correspond to vacancies in the semiconductor lattice, dust, or other impurities in experimental FET devices. As the number of these defects increases, the number of sites that accept charge carriers decreases until all charge transport channels are completely shut down (i.e., based on simple percolation theory). Although the charge transport channels decreases as the defect concentration increases, the average mobility remains approximately constant, even when Coulomb interactions are included. Figure 5.6a illustrates this. At low V_{SD}, the difference in I_{SD} with and without Coulomb interactions is small and the mobility only differs by approximately 34%. This shows that the effect of scattering by trapped carriers on the mobility is small.

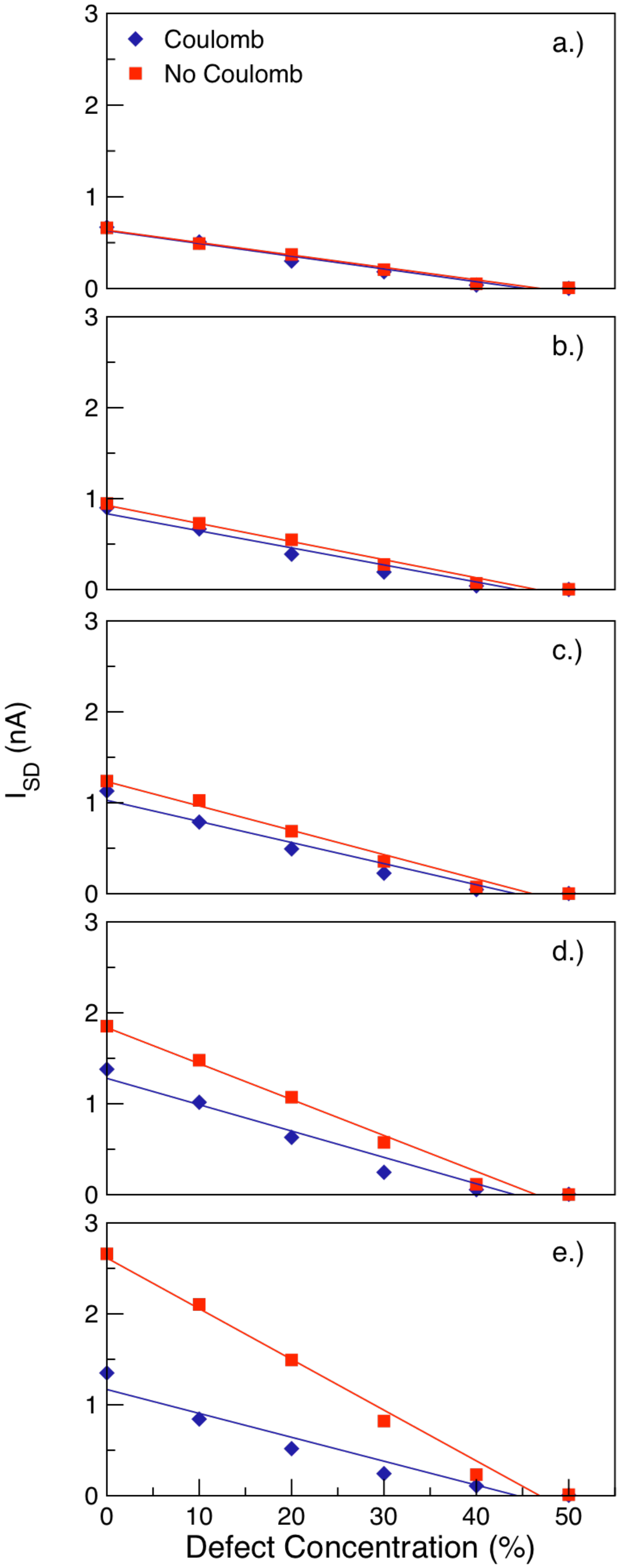

Figure 5.8. I_{SD} vs. defect concentrations at carrier concentrations of (a) 0.5%, (b) 0.75%, (c) 1%, (d) 1.5%, and (e) 2%.

The effects of carrier concentration are shown in Figure 5.9. When Coulomb interactions are neglected, I_{SD} increases as a function of the carrier concentration, approximately linearly at low carrier concentrations, and appears to saturate as the carrier concentration approaches 100%. The functional form of the curve matches Michaelis-Menton or Langmuir-Hinshelwood kinetics;[157] the latter relates reaction rate of a surface catalyzed reaction to the concentration of a reactant species. The equation of the fit is,

$$I_{SD}(in\ nA) = \frac{82.18nA}{1+\dfrac{56.59}{x_c}} \tag{36}$$

Here x_c is the carrier concentration. Similarly to Langmuir-Hinshelwood kinetics at low x_c, I_{SD} increases in proportion to x_c and the number of unoccupied sites. However at high carrier concentrations I_{SD} becomes independent of x_c because the semiconductor grid becomes saturated. Although charge transport becomes limited by percolation, there is still an appreciable I_{SD} since carriers in sites adjacent to the drain electrode can still move to a drain site. As a result, I_{SD} approaches a limiting value at higher carrier concentrations.

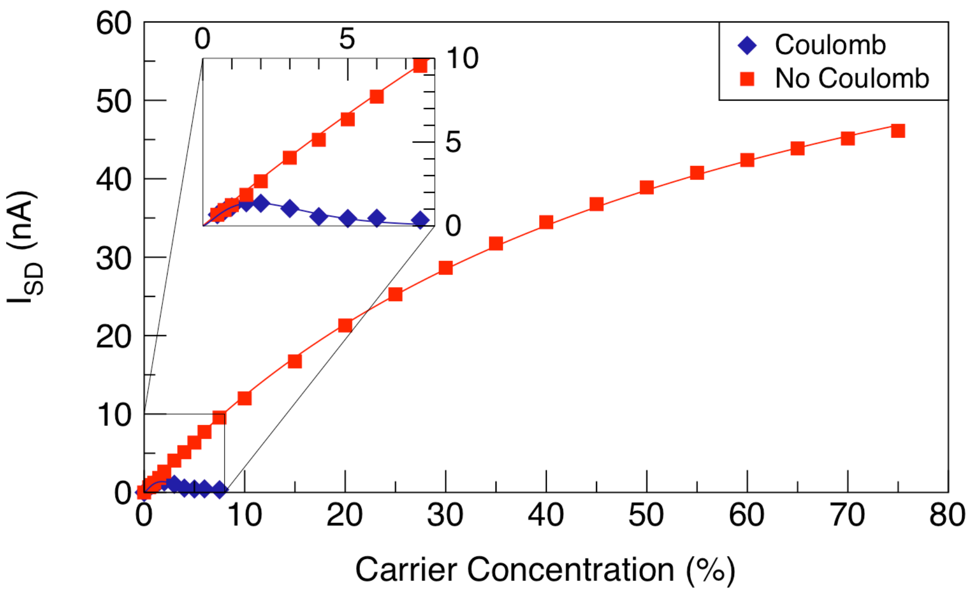

Figure 5.9. I_{SD} vs. carrier concentration (excluding defects).

However, when Coulomb interactions are included, I_{SD} peaks when the carrier concentration is approximately 2% and then decays exponentially. According to Zhou et. al,[126] the electric field caused by the charge carriers causes the site energies (i.e. the HOMO energies) to shift randomly based on the local charge density. This results in an increase in the average effective hopping barrier and a random distribution of "trap states" in the film. Higher carrier concentrations increase the number of these trap states as well as the magnitude of the energy shift. Our model does not explicitly include this process; it is a direct consequence of including electrostatic interactions between carriers. This trapping effect causes I_{SD} to decay at higher carrier concentrations. Also, due to the long-range nature of electrostatic interactions, the carrier concentration does not need to be very high in order to force a site exclusion effect, further decreasing I_{SD}, as observed in our results. This behavior is not observed experimentally, although experimental transistor devices are typically multilayers, so increases in the gate potential need not only affect the nearest molecular monolayer. Instead, we believe our model suggests that experimental gate potentials increases result in increasing I_{SD} because additional conduction channels open in layers above the monolayer closest to the gate and *not* because the carrier concentration increases in the 2D channel.

5.3.5 Effects of charge defects

Figure 5.10 compares the dependence of I_{SD} on neutral and charged defect concentration. For these calculations, we considered singly charged defects (i.e. $\pm$ 1*e*). Our results show that I_{SD} is lower than in the neutral defect case at defect concentrations between 1-20%. In this range, I_{SD} remains roughly constant. At concentrations greater than 20%, I_{SD} decreases and approaches zero at 50% similar to the trend followed with neutral defects. Charge carriers can screen oppositely charged defects as shown in Figure 11a. As a result, regardless of charge, a defect can act as a repulsive charged defect. As shown in Figure 11b, a charge carrier will have a decreased mobility (μ) as it approaches a bare or screened defect. As the charge carrier moves away from the defect, it will have an increased μ. These two effects will, on average, cancel each other out, resulting in a static I_{SD} at low carrier concentration. This effect has also been observed experimentally.[158] The enhanced site exclusion effect decreases I_{SD} in both cases. At high defect concentrations, charge transport reaches a percolation limit regardless of whether or not the defect is charged.

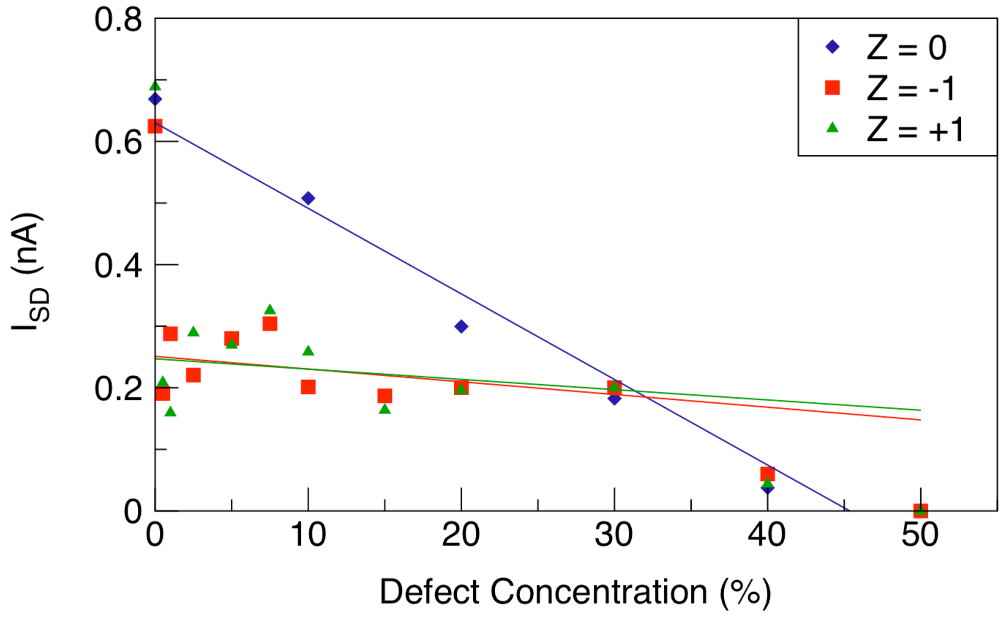

Figure 5.10. I_{SD} vs. neutral and charged defect concentration.

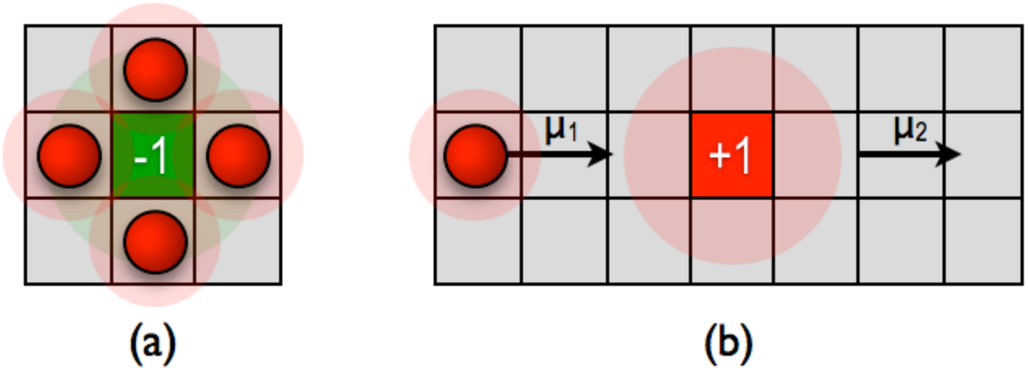

Figure 5.11. Schematics of (a) a shielded negatively charged defect after capturing several hole carriers and (b) indication that mobility near a charged defect will be affected by the electrostatic field.

Much like the case of electrostatic interactions between carriers, interactions between carriers and charged defects cause shifts in site energies. With the concentrations considered here (i.e., up to ~30%), the distances between carrier sites and defects have a Poisson distribution causing the energy shifts to take a reciprocal Poisson distribution.[117] Most importantly, the distribution of site energies has a long tail at low energies. While the presence of charged defects increases all site energies, there always remain low-energy pathways available for transport

5.3.6 Coulomb interactions and charge transport

Our simulations have shown several ways in which electrostatic interactions affects charge transport in organic semiconductors. Electrostatic interactions between charged defects and charge carriers cause I_{SD} to be roughly constant at low defects concentrations. This effect is similar for both positively and negatively charged defects due to screening (see Figure 5.11). Also, electrostatic repulsion between carriers causes a dramatic decrease in I_{SD} at high carrier concentrations when considering a monolayer OFET. This effect is not observed experimentally since most OFETs are fabricated from multi-layered thin films of organic semiconductors and increases in the gate potential will affect layers above the first monolayer.

Our simulations of *I-V* curves show that neglecting electrostatic interactions incorrectly predicts NDR at high V_{SD} when neutral defects are present. This occurs because carrier paths are nearly linear at high V_{SD} and as a consequence, are more likely to encounter a defect. In contrast, the inclusion of electrostatic interactions correctly predicts I_{SD} saturation at high V_{SD}. Finally, when using the time dependent warm-up procedure, I_{SD} is higher at the beginning of the simulation when electrostatic interactions are included. At the start of a simulation (when the carrier concentration is low), the electrostatic repulsion between carriers increases the effective mobility due to field-dependent hopping.

5.4 CONCLUSION

In this work, we have pursued the specific mechanisms of charge transport in organic semiconductors in the presence of explicit defects. In particular, considering photovoltaic materials and OLEDs as "defective" mixed films, we have shown the effect of neutral and charged explicit defects as a function of defect concentrations. We have shown that the inclusion of electrostatic interactions accurately predicts the saturation of I_{SD} at high V_{SD} in the presence of defects. We have also shown that I_{SD} decreases linearly with increasing neutral defect concentration and the average mobility is nearly unaffected by the scattering of charges at low V_{SD}, even when electrostatic interactions are considered. Also, there is still considerable charge transport at 5-15% defects. In contrast, for charged defects, predicted currents are much lower than in defect-free materials, but largely unaffected by defect concentration until almost all pathways are blocked. In practice this means that the difficulty in removing impurities from semiconductor films should not adversely reduce the current in devices fabricated from them, unless the quantity of defects is very high.

Through the use of explicit charged defects, we computed the exact energy distribution due to electrostatic repulsion. The disorder was shown to be a reciprocal Poisson distribution with a long tail at lower energies. These low-energy pathways are responsible for charge transport in the presence of charged defects. This is different than the exponential tail in the energy distribution of crystalline materials[159] and the Gaussian distribution used for polymeric materials[98]. This suggests that the Gaussian disorder model may not always be appropriate to describe non-polymeric organic materials. In the near future, we will simulate charge transport in mixed semiconductor films, which will coincide with the experimental work underway in our group.

6.0 CHARGE TRANSPORT IN IMPERFECT ORGANIC FIELD EFFECT TRANSISTORS: EFFECTS OF CHARGE TRAPS

6.1 INTRODUCTION

As discussed in Section 4.2, weak electronic interactions combined with a greater degree of disorder in amorphous organic semiconductors results in the localization of charge carriers on molecular sites. The natural tendency for charge carrier localization makes charge transport through organic semiconductors more sensitive towards charge traps, which cause carriers to localize in a region of the material for an extended period of time. For this reason, a fundamental understanding of how charge traps affect charge transport in organic semiconductors is essential.

There are several origins of trap states, some of which are discussed in Section 5.1. Also, changes in site energies due to structural defects[160] and electronic effects such as polarization can cause charge traps. In addition, if both holes and electrons are present, as they are in OLEDs and photovoltaics, the low dielectric environment can cause "Coulomb traps" to form from bound hole-electron-pairs.[161] Trap energies are located in the HOMO-LUMO gap of the material; hole traps have higher energies than the highest occupied molecular orbital (HOMO) while electron traps have lower energies than the lowest unoccupied molecular orbital (LUMO) (see Figure 6.1).

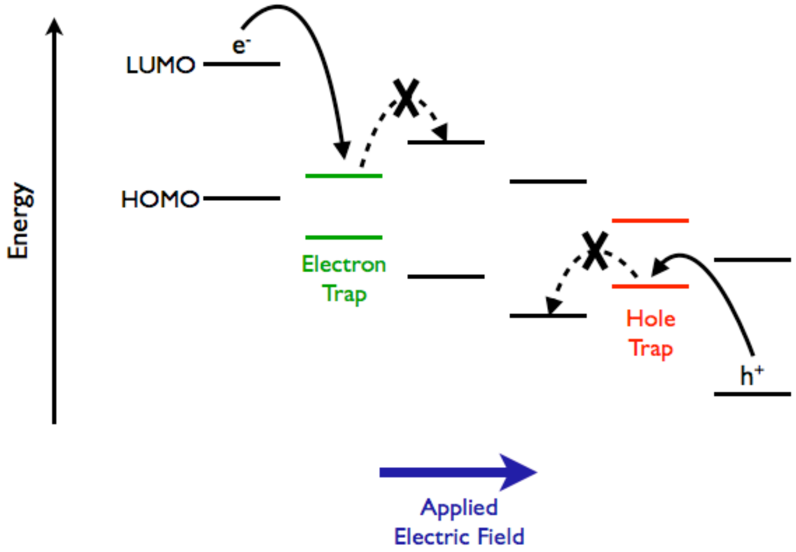

Figure 6.1. Energy landscape of an organic semiconductor showing electron and hole traps.

It is very difficult to determine the energetic and spatial distribution of charge traps in organic semiconductors. Many simulation models that include charge traps assume that trap energies follow a Gaussian distribution (see Section 4.4) and that trap states are uniformly distributed throughout the material. However, it is difficult to directly determine this information experimentally. There is some evidence that traps can have a non-uniform spatial distribution; a number of experimental studies show evidence of “metallic islands”, which are highly ordered regions within amorphous polymeric materials.[162-164] While it has been suggested that these metallic islands enhance charge transport by allowing charge carriers to travel over longer distances, others have suggested that these highly conductive regions act as charge traps.[165] Theoretical studies of how the distribution of trap states alters charge transport in organic materials would provide a great deal of insight into such phenomena.

In this chapter, the effects of explicit traps on charge transport in an imperfect OFET device consisting of a monolayer of molecular sites (see Figure 5.1) are studied using Monte Carlo simulations. As in the previous chapter, we have "frozen out" the Gaussian disorder approximation, which treats the effects of trap states implicitly. This work will address the effects of trap concentration and energy on charge transport. We will also look at how the distribution of trap sites in the OFET alters the dependence of the device current on trap concentration.

6.2 COMPUTATIONAL METHODS

The simulation code described in Section 5.2 was used for these calculations with a few modifications to include trap sites. In our simulation model, we differentiate between defect and trap sites. Defect sites are unable to accept of charge carrier but instead act as a "wall" to charge transport. In contrast, trap sites are able to accept a charge carrier, but have a different orbital energy. Trap sites are created by taking a specified number of grid sites and adding $\Delta\varepsilon$ to the potential energy due to the applied field. To create trap sites that are higher in energy a positive $\Delta\varepsilon$ is used; similarly a negative $\Delta\varepsilon$ is used to create trap sites that are lower in energy (see Figure 6.2).

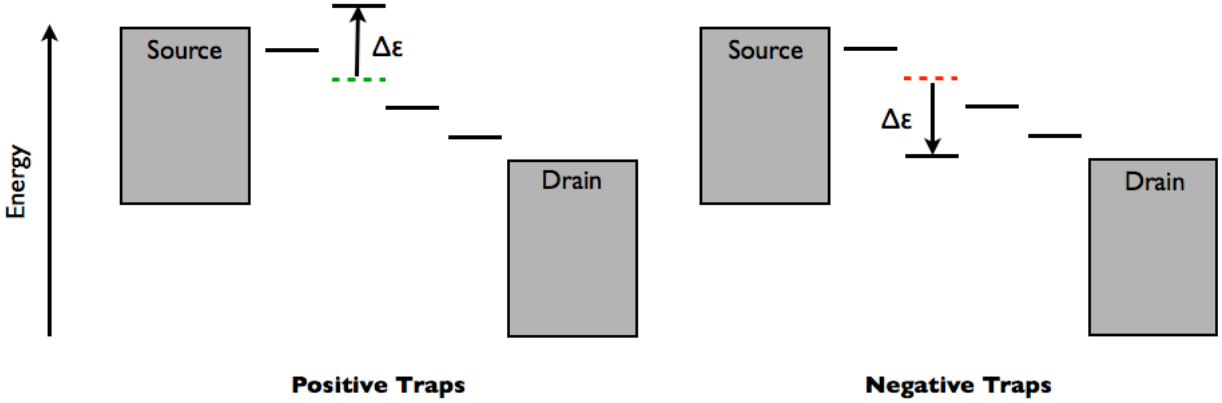

Figure 6.2. Energy diagram showing the creation of charge traps.

By default, our code chooses grid sites at random to create traps, which results in a uniform or homogeneous distribution of trap sites. A non-uniform, heterogeneous distribution of trap sites is achieved by first seeding the grid with a number of trap sites and then looping over the trap seeds to grow them into "islands" of trap sites (see Figure 6.3). As illustrated in Figure 6.4, the number of trap seeds controls the distribution of trap sites; less trap seeds create a more heterogeneous distribution of trap sites.

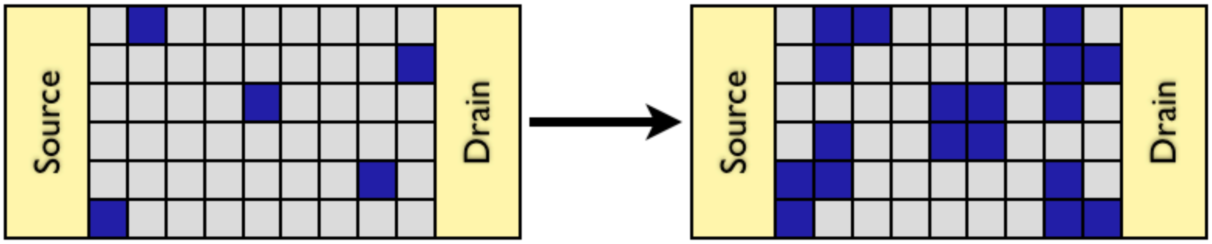

Figure 6.3. Creating a heterogeneous distribution of traps by seeding the grid with a small number of traps (left), then adding trap sites around the seeds.

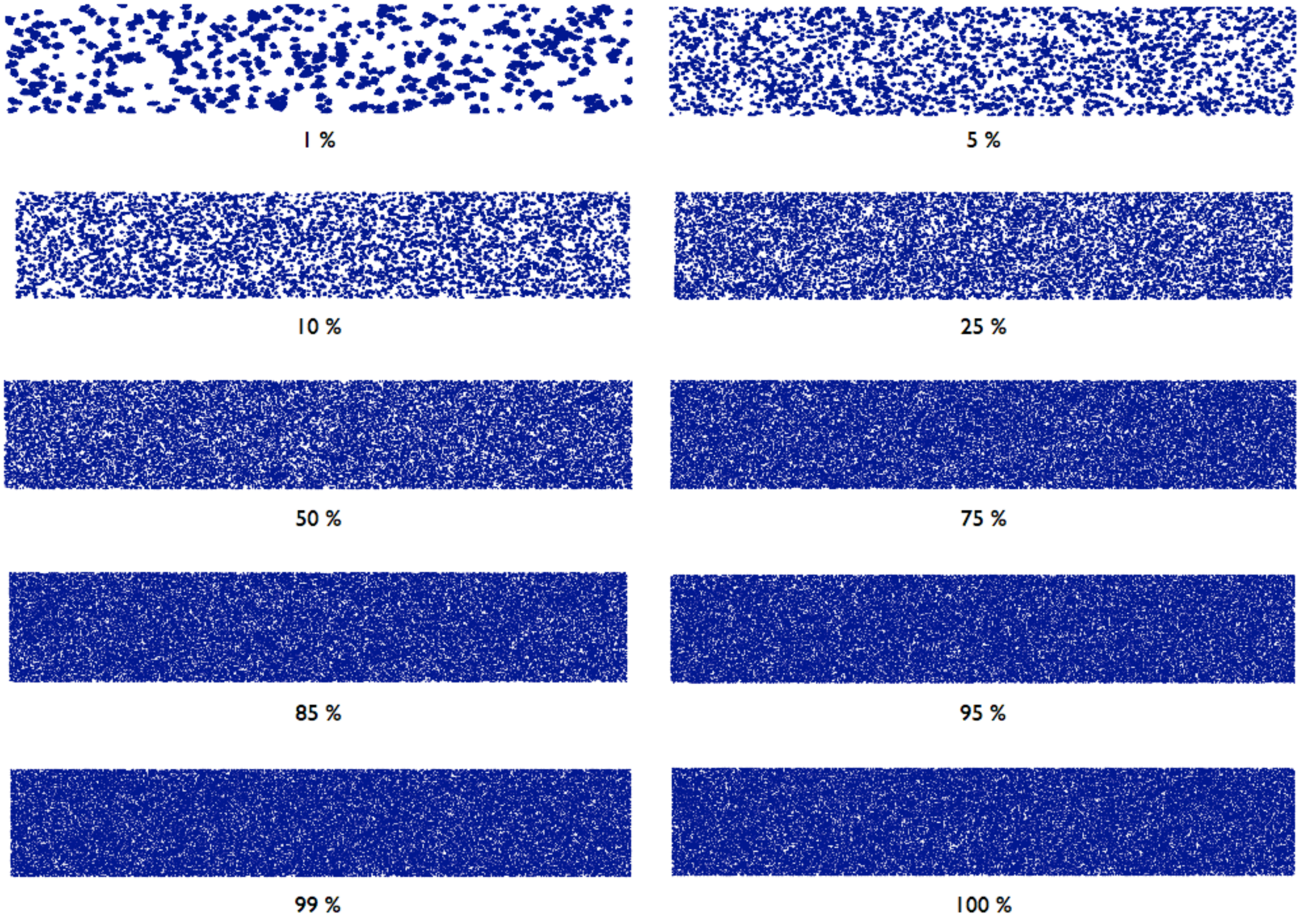

Figure 6.4. Spatial distribution of trap sites (blue areas) at different seed percentages, all with a total trap concentration of 20%.

6.3 RESULTS AND DISCUSSION

6.3.1 Homogeneous Traps

Figure 6.4 show the results from the simulation of the source drain current (I_{SD}) as a function of the homogeneous trap concentration for both positive and negative values of $\Delta\varepsilon$. In both cases, I_{SD} decreases as the trap concentration increases, reaches a minimum, and increases as the trap concentration approaches 100%. As the absolute value of Δε increases, the I_{SD} minimum decreases. The energy difference between the trap sites and the "normal" transport sites causes a charge transfer barrier, which reduces the carrier mobility. As the trap concentration is increased, I_{SD} decreases until it reaches a minimum, which can be explained by simple percolation theory. However, as more trap sites are added, charge transfer between "trap sites" is possible and I_{SD} recovers.

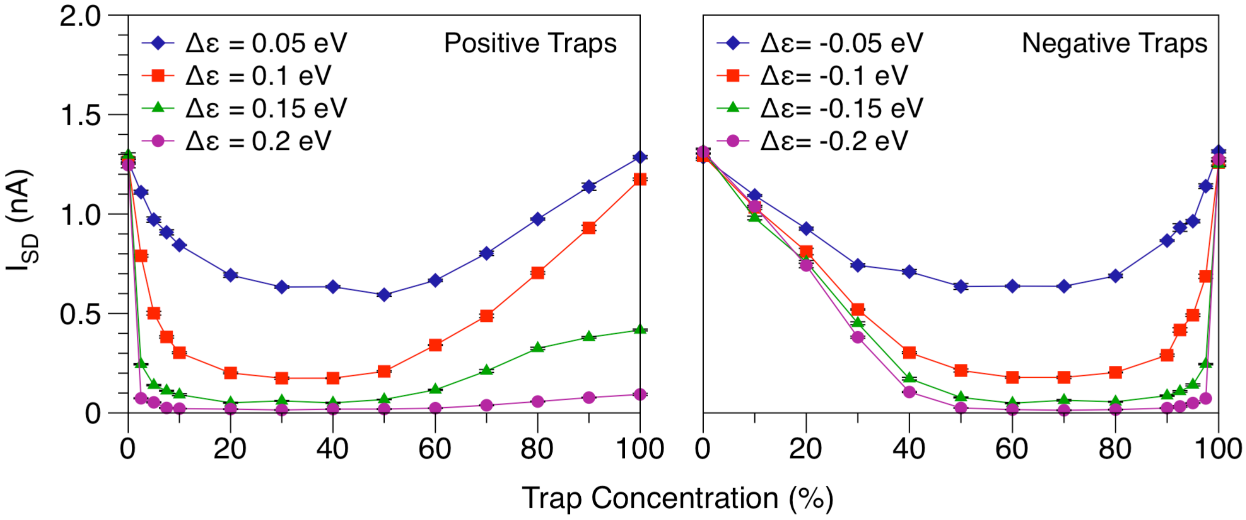

Figure 6.5. I_{SD} vs. homogeneous trap concentration for positive (left) and negative traps.

Percolation theory predicts that I_{SD} should reach a minimum when the trap concentration is approximately 50%. However, our simulations predict that the I_{SD} minimum is shifted towards lower concentrations (~20-30%) when Δε is positive and higher concentrations (~60-70%) when *Δε* is negative. The asymmetry in the plots agree with experimental results[113-114] as well as simulations and theoretical studies that use the Gaussian Disorder Model.[112, 115-116] Numeric kinetics simulations were employed in an attempt to explain the asymmetry in the plots shown in Figure 6.5, however they gave little insight into this feature (See Appendix D).

Our simulation model assumes that the grid sites have the same conductivity regardless of them being traps or not. Therefore, it is expected that I_{SD} is similar at trap concentrations of 0% and 100%. Although this is the case for negative traps, I_{SD} decreases at 100% traps as $\Delta\varepsilon$ increases when positive traps are used. When the trap concentration is 100%, all of the sites neighboring the source electrode are trap sites. Since the trap sites are higher in energy than the source electrode, there is a barrier for charge carriers to be injected from the source electrode onto the grid, which lowers the charge injection probability. This “charge injection barrier” increases as $\Delta\varepsilon$ increases. In contrast, the drain electrode always accepts charge carriers, which prevents a similar problem from occurring when negative charges are used.

6.3.2 Heterogeneous Traps

To examine the effects of the trap heterogeneity on charge transport, I_{SD} was simulated as a function of the trap concentration while varying the seed percentage between 1% and 100%. The results of these simulations are shown in Figures 6.6 and 6.7 for positive and negative traps respectively. Both figures show that at seed percentages less than 75%, I_{SD} decreases as a function of the trap concentration, approaching zero when the trap concentration is ~60% when the seed percentage is less than 50%. However, at seed percentages greater than 75%, I_{SD} at 100% traps begins to recover, with a complete recovery when the seed percentage is above 90%. Again, we believe that the lack of I_{SD} recovery at 100% traps is an artifact of our current simulation model due to the charge injection barrier. Nevertheless, the minimum I_{SD} tends to shift towards higher trap concentrations as the system becomes more heterogeneous for positive charges and (slightly) towards lower trap concentrations for negative traps.

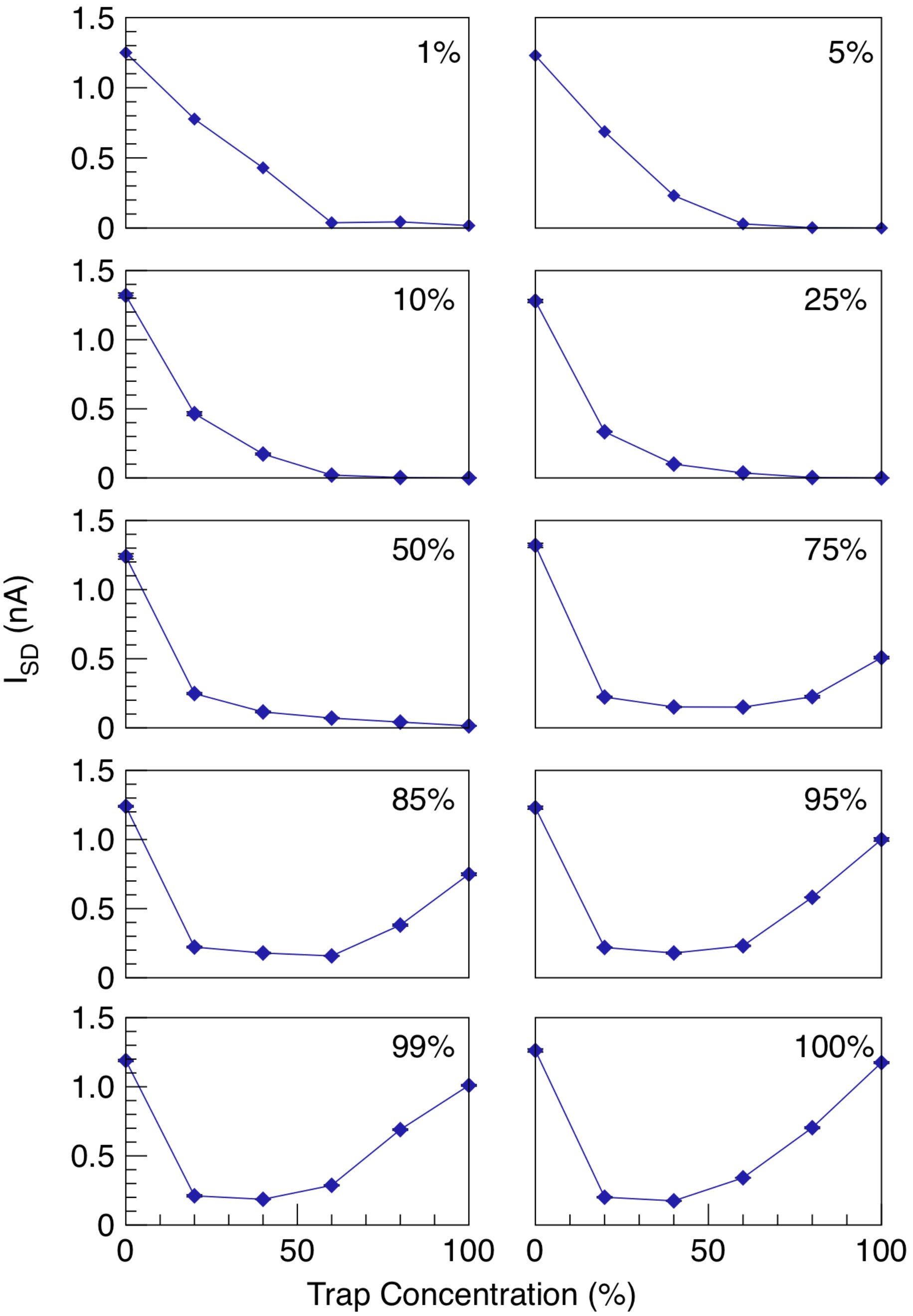

Figure 6.6. I_{SD} vs. trap concentration profiles for different seed percentages. $\Delta\varepsilon = 0.1$ eV.

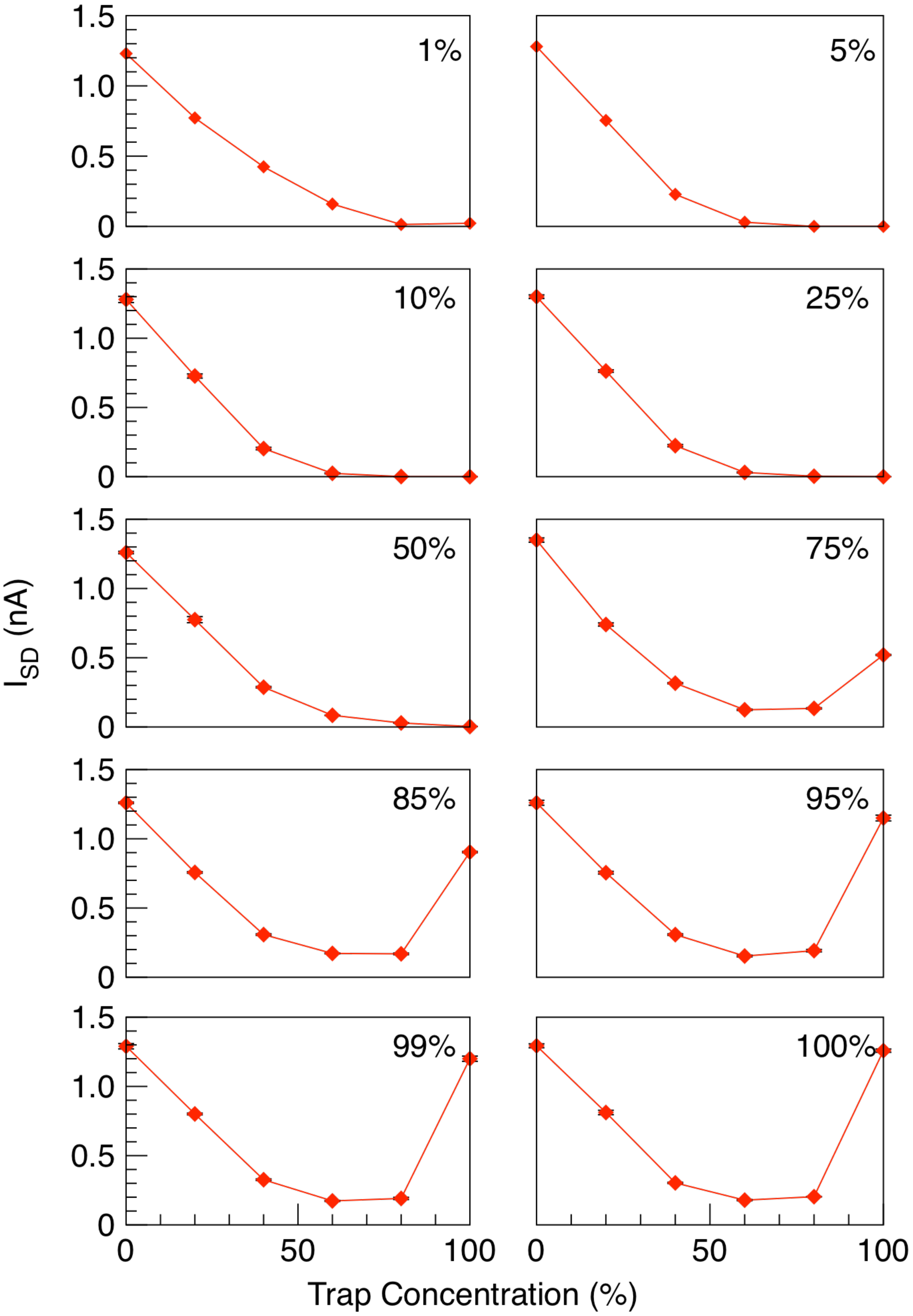

Figure 6.7. I_{SD} vs. trap concentration profiles for different seed percentages. $\Delta\varepsilon$ = -0.1 eV

In order to gain insight into the effect of trap distribution on the concentration dependence of I_{SD}, we examined the distance and energy distributions between carriers and trap sites. Figure 6.8 shows the distribution of distances for a 1024 x 256 grid (red curve). Aside from some subtle differences, the distribution is the same for the seed percentages considered. However, there is a geometric dependence on the distance distribution; the distances between carriers and traps in the 1024 x 256 grid gives a Poisson distribution while the 512 x 512 grid gives a Gaussian distribution

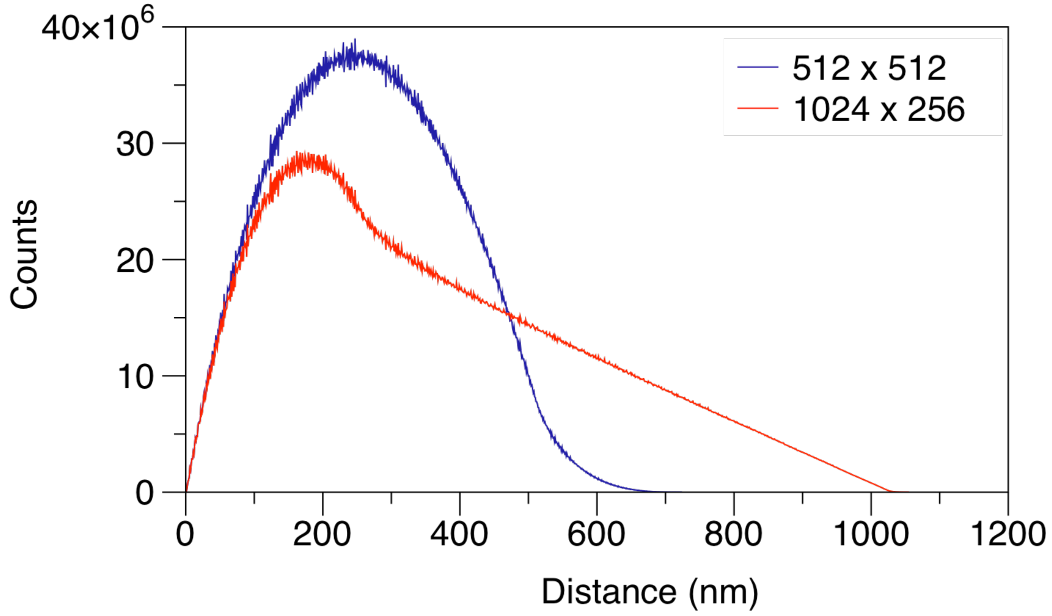

Figure 6.8. Distribution of distances between charge carriers and trap sites for different grid geometries, homogeneous seeding, and a 20% trap concentration.

Although the distribution of distances between the carriers and trap sites does not depend on the seed percentage, Figure 6.9 shows that the potential energy distribution does. The potential energy between carriers and trap sites for more heterogeneous systems has a Gaussian-like distribution. However, as the system becomes more homogeneous, the energies take on a reciprocal Poisson distribution, with only subtle differences in the energy distribution as the homogeneity of the system increases. The energy distribution also changes with the geometry of the grid; the energy distribution for "square" grid is shifted towards higher potential energies (see Figure 6.10).

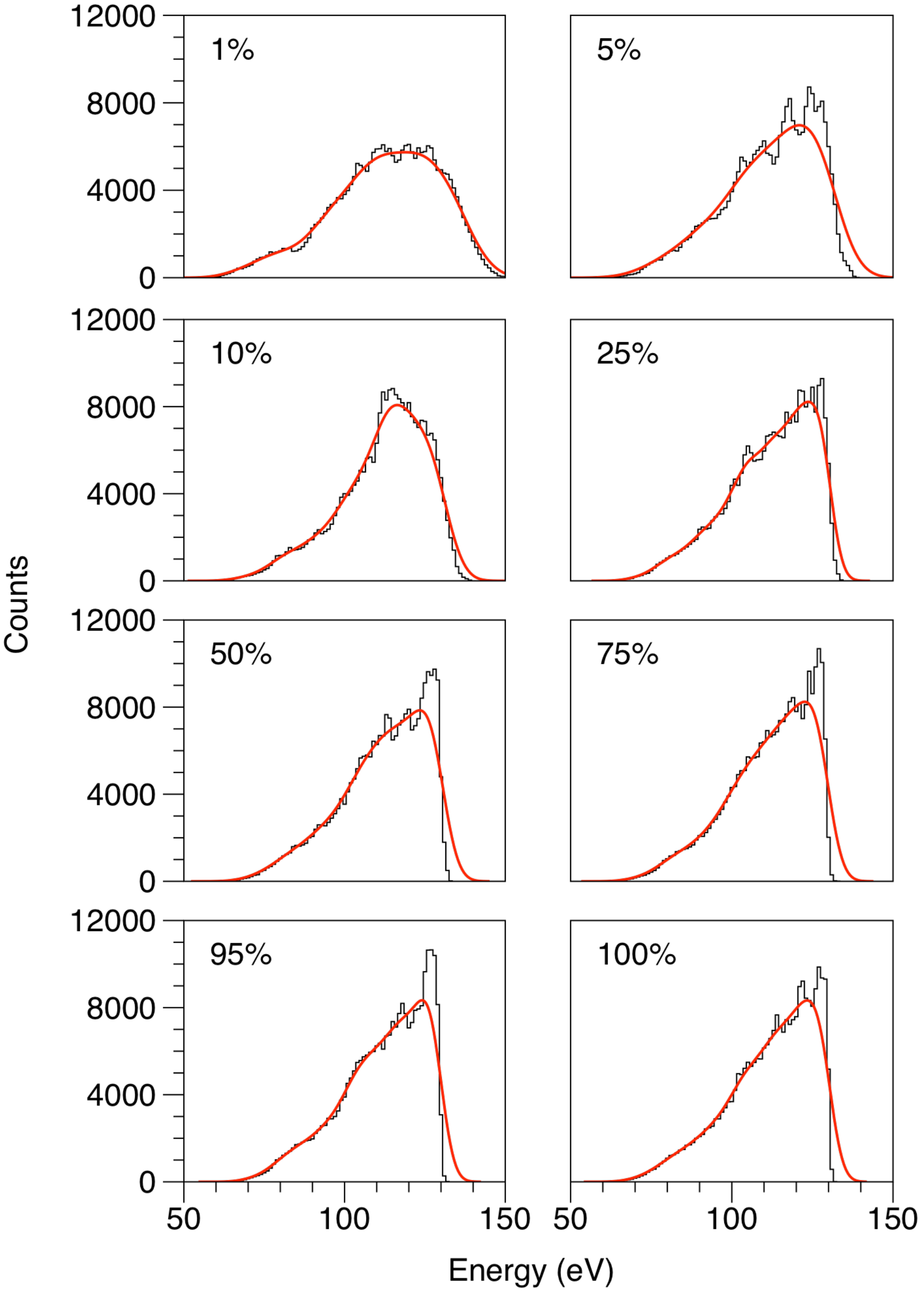

Figure 6.9. Distribution of potential energy between charge carriers and trap sites at different seed percentages.

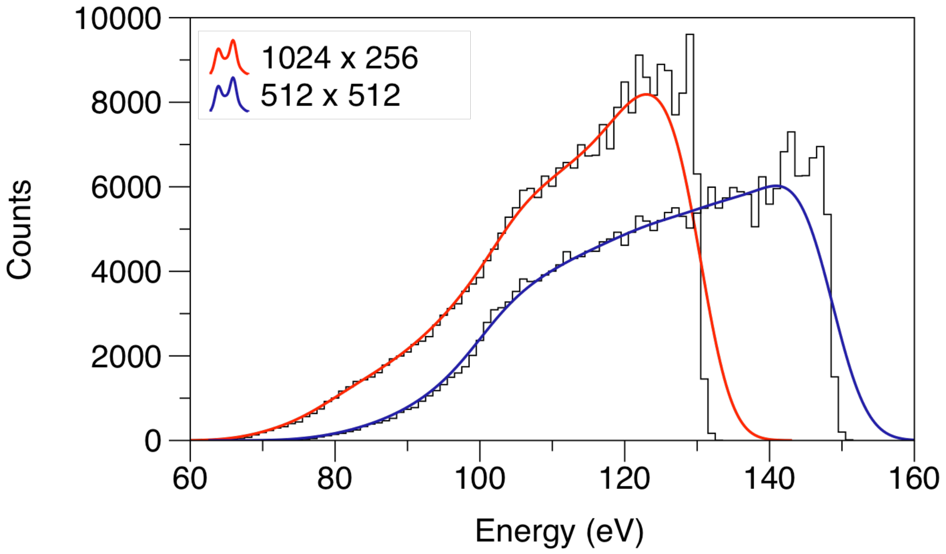

Figure 6.10. Distribution of potential energy between charge carriers and trap sites for different grid geometries, homogeneous seeding, and a 20% trap concentration.

These results suggest that although spatial distribution of traps has little effect on the distribution of distances between carriers and trap sites, it significantly affects the potential energy distribution. These differences in the energy distribution impact the dependence of I_{SD} on the trap concentration, as illustrated in our simulation results.

6.4 CONCLUSION

In this chapter, we explored charge transport in organic semiconductors in the presence of charge traps. Through the use of explicit heterogeneous traps, we have shown that charge transport decreases at low concentrations, reaches a minimum, and increases as the trap concentration approaches 100%. Our simulations produce results that match experimental and previous simulation results that use the Gaussian Disorder Model when we assume a homogeneous distribution of traps. However, we have also shown that a homogeneous distribution of traps gives a non-Gaussian distribution of energies.

We have also shown that the trap concentration dependence of charge transport can vary with the spatial distribution of traps in our model OFETs. Our results indicate that there is no charge transport at high trap concentrations when the spatial trap distribution is highly heterogeneous. We have also shown that differences in the spatial distribution of traps affect the distribution of potential energy between carriers and trap sites more than the distribution of distances. In addition, these distributions depend on the geometry of the device. These distributions are shown to be more Gaussian for very heterogeneous trap distributions while taking on a Poisson distribution as the spatial trap distribution becomes more homogeneous. This is in opposition to what is intuitively assumed about disorder in organic materials; that trap states are randomly, but uniformly distributed throughout the material and that the energies follow a Gaussian distribution. These results suggest that when considering disorder in organic materials, we must consider the geometric distribution of trap states as well as the geometry of the device.

In practice, the distribution of trap sites in an organic semiconductor device is often uncontrolled. Our simulations indicate that this information can be determined by studying the dependence of charge transport on the concentration of intentionally added charge traps. There are few studies that have accomplished this experimentally by making devices from mixtures of organic materials; more studies along these lines will allow us to gain more insight into the spatial distribution of traps in organic electronics. Our group is currently doing such experimental work by making OFETs from mixtures of metal phthalocyanines.

7.0 THE EFFECTS OF CHARGE LOCALIZATION ON THE ORBITAL ENERGIES OF BITHIOPHENE CLUSTERS

7.1 INTRODUCTION

An underlying assumption in the theory and computational simulation of charge transport in organic semiconductors is that charge carriers are typically localized on a single molecular site. As a consequence, charge transfer occurs through variable range hopping (VRH: see Section 4.2). The VRH model assumes that charge carriers remain localized on an individual molecular site between charge transfer events that are discrete and independent of each other. The VRH model has been through numerous experimental studies, including temperature-dependent single-crystal measurements.[166-168] Although not inherent of VRH itself, many studies, including those presented in Chapters 5 and 6, assume that all molecular sites are identical, although with some amount of energetic disorder.[98] In addition, it is assumed that the interactions between molecular sites are identical.

However, there is evidence to suggest that these fundamental assumptions made in charge transfer theory and computer simulations require revision. Dimers of charged, π stacked oligomers are known to exist in solution.[169-171] In addition, dimers and larger-sized clusters of charged, π-stacked aromatic molecules have been observed in gas phase experiments.[172-174] This suggests that charge carriers can delocalize throughout several molecular sites.

Recent studies have also addressed the effects of electrostatic polarization on site energies, indicating that these effects are dependent on the geometry of the molecules in the lattice.[175] It has also been shown that electrostatic interactions between charge carriers and charged defects can also affect carrier mobility.[117] Finally, several groups have addressed variations in electronic coupling due to molecular dynamics and lattice vibrations[176-178] in addition to anisotropic interactions due to the structure of the solid state.

The evidence presented above shows that VRH models must be expanded so that the charge transfer rates depend also on the state of the local neighborhood, which would include electrostatic interactions and polarization effects as well as charge delocalization. In essence, simulations would consider the electronic structure of clusters of molecular sites instead of treating the organic material as a grid of independent sites.

In this work, we examine how charge localization and delocalization affect orbital energies of clusters of bithiophene clusters using first principles quantum chemistry calculations. Since most oligothiophenes are p-type conductors, our calculations will focus on positively charged (+1 and +2) bithiophene clusters. To make this comparison, constrained density functional theory (CDFT)[179] is used to intentionally localize a unit of charge on one or more molecular sites in the clusters. CDFT has recently been used to calculate charge transfer parameters[180-185] but has not been used to study how orbital energies are affected by charge localization. The CDFT calculations will be compared to standard DFT calculations, which allow the charge to delocalize over several molecular sites. We will specifically look at how the geometry of the molecular sites affect how charge is distributed throughout the clusters.

7.2 COMPUTATIONAL METHODS

The bithiophene clusters (see Figure 7.1) were generated from the experimental crystal structure obtained from the Cambridge Crystal Structure Database[186]. The clusters were generated using large super cells and removing unwanted molecular molecules using the Avogadro program.[187] Single point energy calculations were carried out using Q-Chem v. 3.2,[188] which has an implementation of CDFT, using the B3LYP[142-143] and the M06-2X[189] functionals and a 6-31G(d) basis set. Although the orbital eigenvalues obtained from DFT calculations are unphysical, it has been shown that the highest occupied Kohn-Sham orbital eigenvalue is approximately equal to the negative of the ionization potential.[190] We found that including an empirical dispersion correction[191] had no effect on the orbital eigenvalues.

To set up the CDFT calculations, a constraint operator must be specified to enforce the charge constraints. This was done by determining a series of coefficients (c_i) that give a total constraint value for the system. The constraint value (C) is given by,

$$C = \sum_{i=1}^{n} c_i m_i \tag{37}$$

where m_i is the charge on each bithiophene molecule in a cluster of size n, which is determined by taking the difference in the number of electrons and protons in the molecule. The coefficients are chosen so that the total charge on the cluster (+1 or +2) is satisfied and the total charge was constrained on the desired bithiophene molecule(s) in each cluster. An example Q-Chem input file is included in Appendix E.

7.3 RESULTS AND DISCUSSION

7.3.1 Comparing the Orbital Energies of Neutral, Singly, and Doubly Charged Bithiophene Clusters

We first examined how the addition of positive charges affects the highest occupied molecular orbital (HOMO) of two series of bithiophene clusters (see Figure 7.1) using standard DFT. In Series 1, the end molecules are parallel to the x-axis and in Series 2 the end molecules are tilted with respect to the x-axis. This comparison serves two purposes. First, it allows us to determine the DFT localization lengths for the charged clusters. In addition, we are able to determine the ionization potential for an infinite one-dimensional cluster, which is not possible with lattice calculations using periodic boundary conditions. Both of these tasks can be accomplished by plotting the HOMO energies as a function of *1/N* where *N* is the number of bithiophene molecules in the cluster. The localization length can be estimated by finding the cluster size at which the HOMO energy appears to saturate. The ionization potential of an infinite one-dimensional cluster can be estimated by the "y-intercept" of the plot, where *1/N* equals zero (i.e., where *N* approaches infinity).

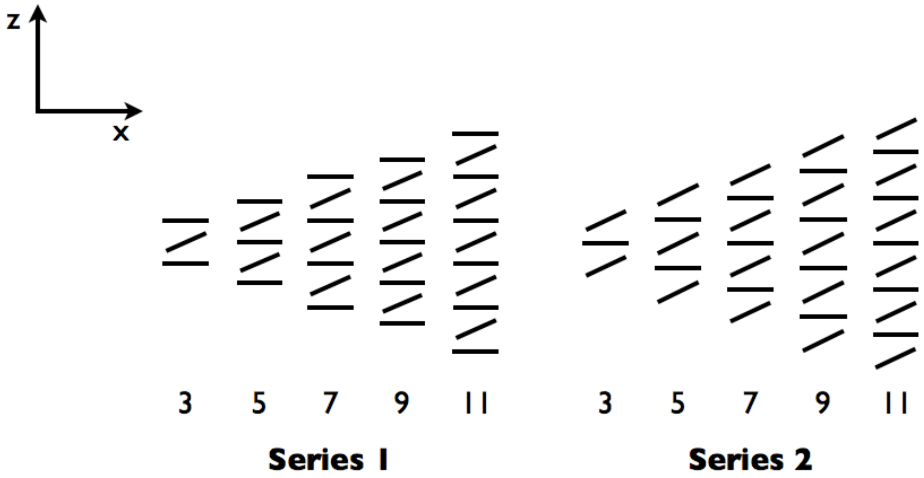

Figure 7.1. Bithiophene series for calculations shown in Figure 7.2.

Figure 7.2 shows plots of the HOMO energies of our clusters as a function of 1/N for using the B3LYP and M06-2X functionals. For the neutral clusters, the HOMO energies remain roughly constant as the cluster size increases. However for the charged clusters, the HOMO energies increase linearly as the cluster size increases, with the plots for the doubly charged clusters having a more negative slope. These trends are seen for both series and when the calculations are performed with both the B3LYP and M06-2X functionals, although the M06-2X energies are lower (e.g., -4.98 eV using B3LYP and -6.26 eV using M06-2X for the Series 1 three molecule cluster).

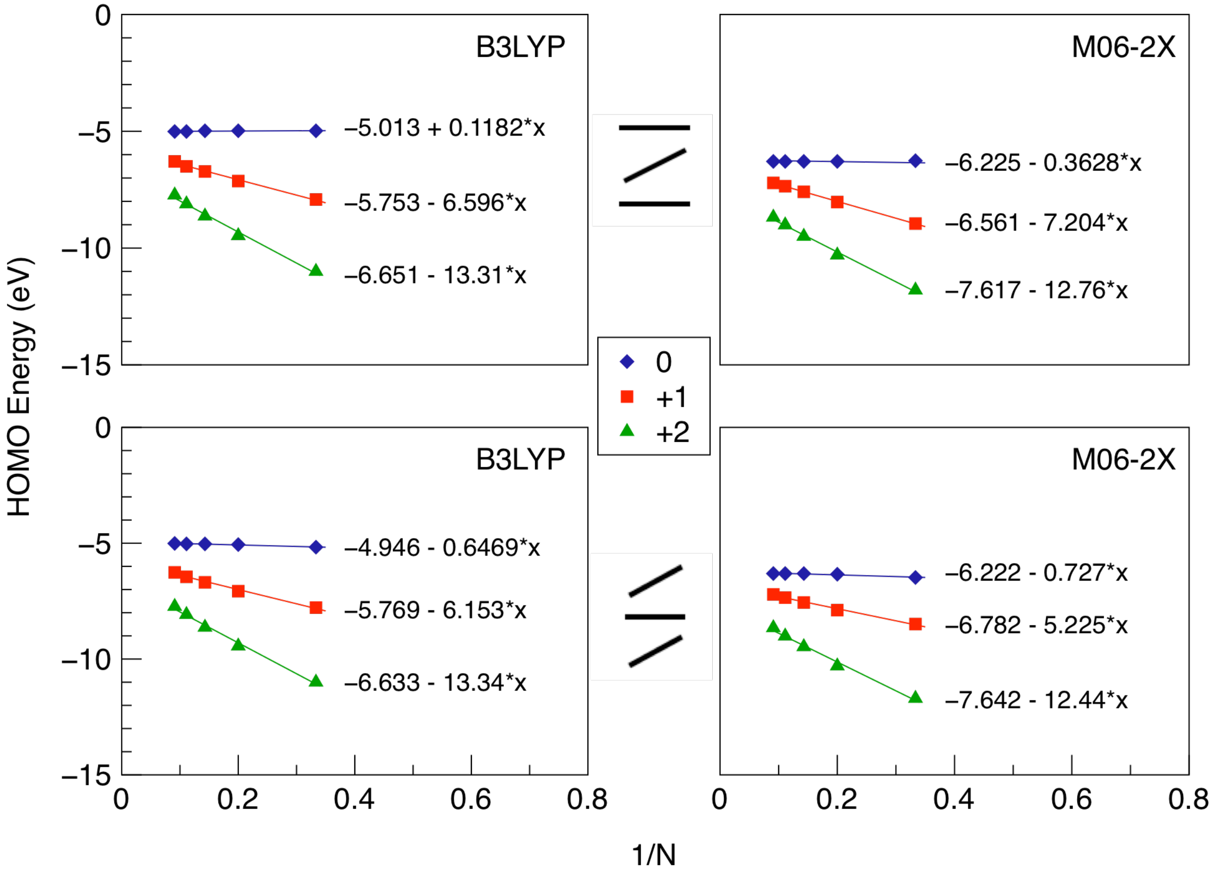

Figure 7.2. HOMO Energy vs. 1/N for neutral, singly, and doubly charged bithiophene clusters**.** Shown are B3LYP (left) and M06-2X results for Series 1 (top) and Series 2. Blue diamonds represent neutral clusters, red squares represent singly charged clusters, and green triangles represent doubly charged clusters.

The plots for the charged clusters do not saturate at large N values, which suggests that at least for these widely used functionals, the localization length for charged clusters is at least 11. To help estimate the localization length, we performed Hartree-Fock (HF) calculations on our clusters using the same basis set. It is known that DFT tends to delocalize charges while HF tends to localize charges,[192-193] so the degree of charge delocalization should lie somewhere between these extremes. Figure E.1 shows the HF calculations for the neutral and charge cluster series depicted in Figure 7.2. These illustrate that the positive charge localizes over approximately 8 molecules.

As mentioned, we can estimate the ionization potential of an infinite one-dimensional cluster from the equations of the best-fit lines for our plots. The equations in Figure 7.2 show that the y-intercept becomes more negative as more charge is added to the clusters. As a consequence, assuming Koopmans' theorem, the ionization potential is increasing by ~0.7-0.9 eV when B3LYP is used and ~0.3-1.1 eV when M06-2X is used for each positive charge added to the clusters. These results indicate that the ionization of an infinite one-dimensional lattice changes significantly with addition of charge carriers.

7.3.2 Singly charged bithiophene clusters

We examined the effects of localizing a single positive charge on a bithiophene molecule in two series of clusters (Figure 7.3). For the CDFT calculations, the charge was localized on the central molecule in all of the clusters composed of 3 or more molecules. In Series 1, the center molecule is tilted with respect to the x-axis and in Series 2 the center molecule is parallel to the x-axis.

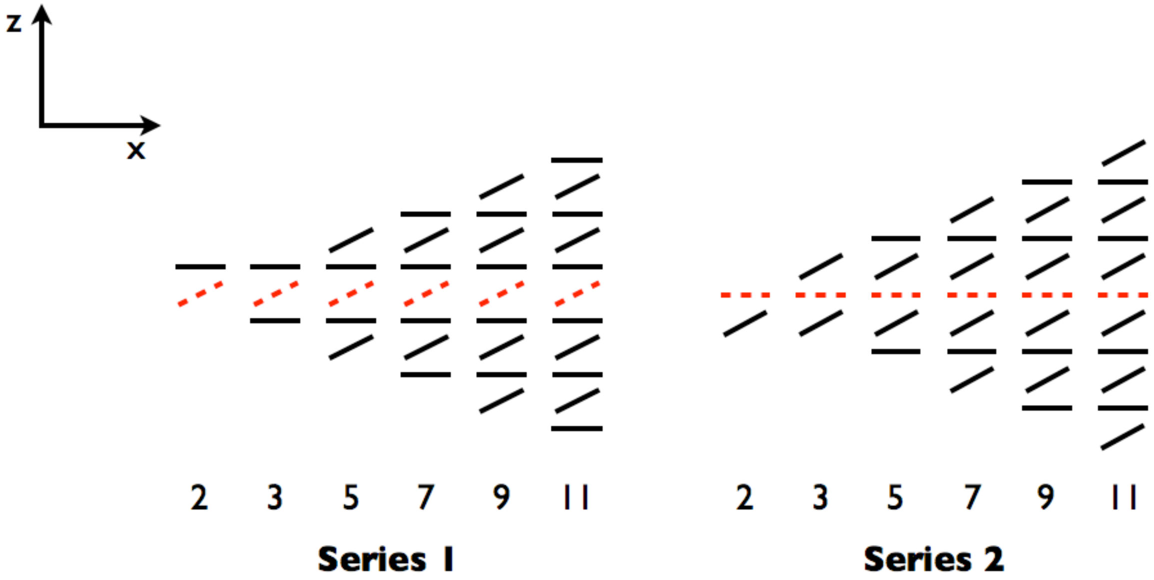

Figure 7.3. Bithiophene Series for Figure 4. A red dashed line represents the molecule at which the charge is localized in CDFT calculations.

Figure 7.4 shows the HOMO energies plotted as a function of 1/N. For Series 1, the HOMO eigenvalues increase as the size of the cluster increases when DFT is used. This is predicted by standard band theory; as more molecules are added to the bithiophene cluster, the orbitals from each added molecule mix causing the HOMO of the cluster to increase in energy. As a result, the positive charge to delocalize throughout the entire cluster. However, when CDFT is used, the HOMO energies remain roughly constant over the cluster size range used. This is expected; adding more molecules to the bithiophene stack should not change the HOMO energy if the charge is localized on one molecule. This trend holds when both the B3LYP and M06-2X functionals are used, although the M06-2X energies are slightly lower.

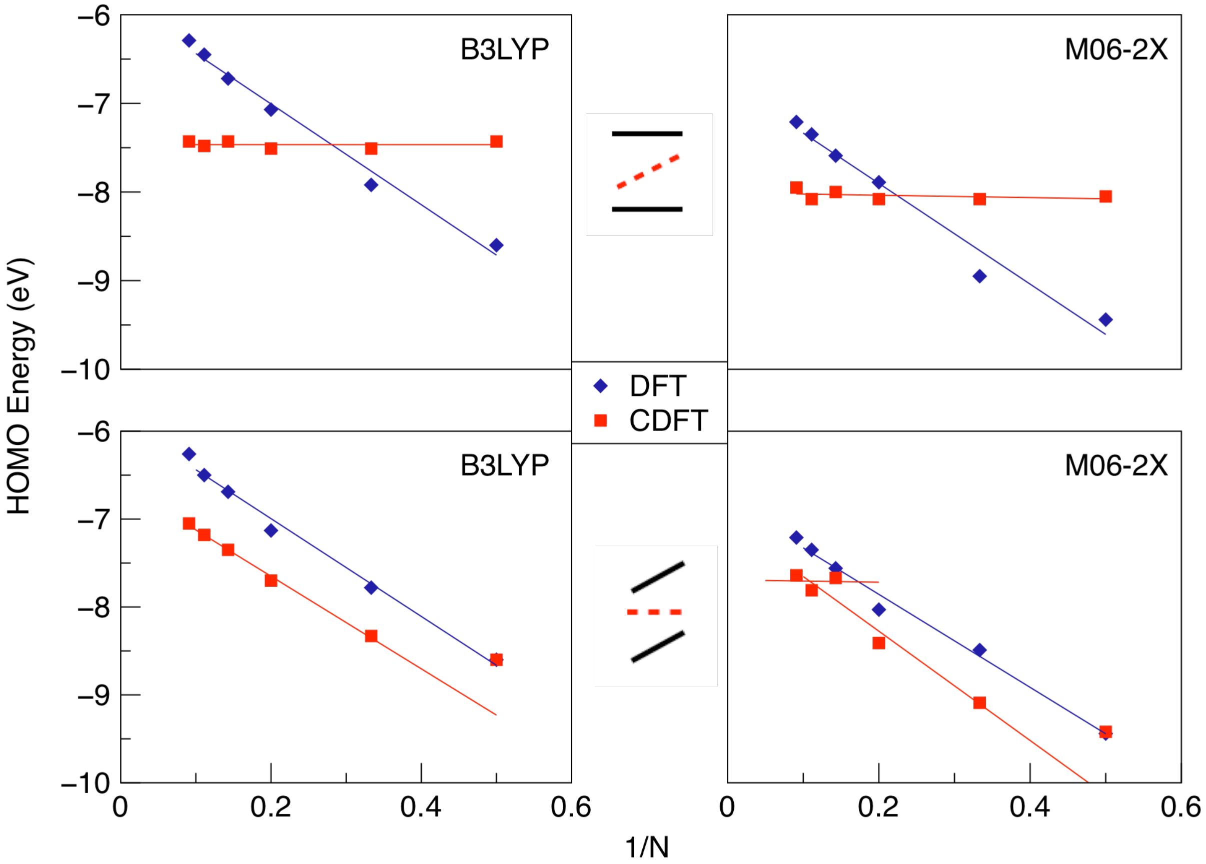

Figure 7.4. HOMO Energy vs. 1/N for singly charged bithiophene clusters. Shown are B3LYP (left) and M06-2X results Series 1 (top) and Series 2. Blue diamonds represent DFT calculations and red squares represent CDFT calculations.

For Series 2, the HOMO energies increase linearly as the size of the cluster increases regardless of whether DFT or CDFT is used when the B3LYP functional is used. When the M06-2X functional is used, the plot appears to saturate for cluster sizes larger than 7 molecules. Also, there is less difference in the HOMO energies when DFT is used versus CDFT. This suggests that it is difficult to localize the positive charge on the center molecule if it is parallel to the x-axis.

We examined the average Mulliken charge on the carbon atoms in each bithiophene molecule in the clusters to help explain this result. Figure 7.5 show plots of the average Mulliken charge as a function of the molecule in the 7-molecule clusters for each series. For the DFT calculations, the average charge on the carbon atoms of the tilted molecules is slightly less negative than for those molecules that are parallel to the x-axis. For the CDFT calculations, both series show that the central molecule bears the majority of the positive charge (as expected from the constraint), however the charge is noticeably more positive for Series 1. Furthermore, in Series 1, the molecules next to the positive localized charge gain a noticeably larger negative charge, which is not observed in Series 2. These results indicate that it is easier to localize a positive charge on a molecule that is tilted than one that is parallel to the x-axis.

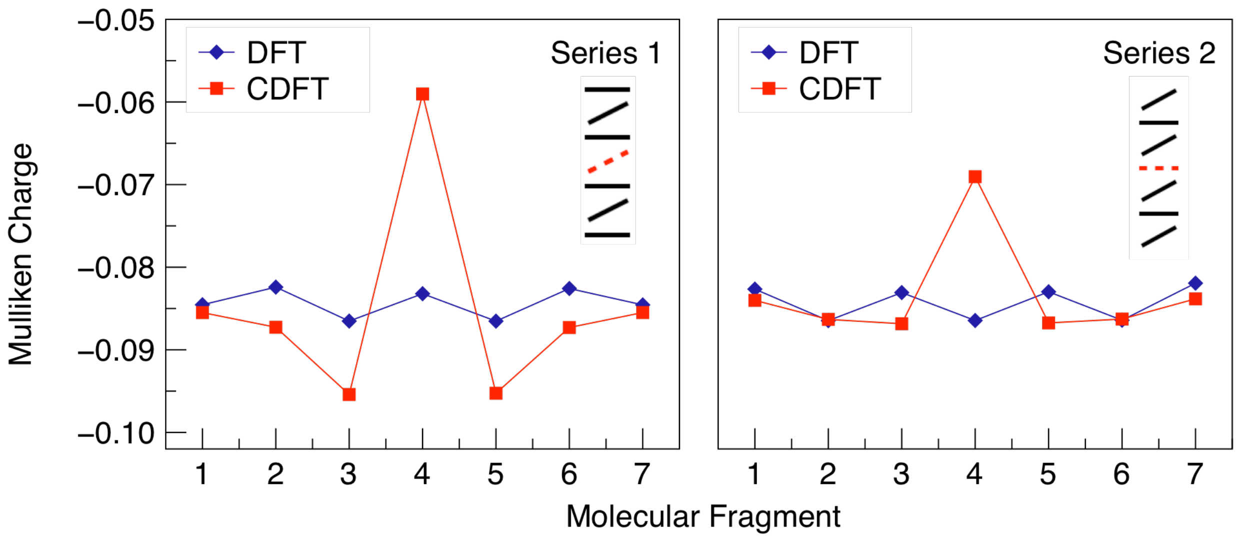

Figure 7.5. Average carbon Mulliken charge vs. molecular fragment for the 7-molecule singly charged cluster in Series 1 (left) and Series 2. Blue diamonds represent DFT calculations and red squares represent CDFT calculations (B3LYP).

This is likely due to electronic polarization, which has been shown to affect orbital energies in dimers and clusters of π systems.[175] The molecules in the clusters adopt a "herringbone" packing arrangement in order to allow for favorable quadrupolar electrostatic interactions between the π cloud of the "parallel" molecules and the edges of the "tilted" molecules, which bear a partial positive charge.[140] Localizing a positive charge on a parallel molecule depletes the electron density of the π cloud. As a consequence, the electrostatic interaction will be destabilized since the edges of the tilted molecule are now interacting with a π cloud with less electron density. This destabilization should diminish if the charge is localized on a tilted molecule since its π cloud does not interact directly with the edge of another molecule. Consequently, in Series 2 less positive charge is localized on the central molecule in the bithiophene clusters when compared to Series 1.

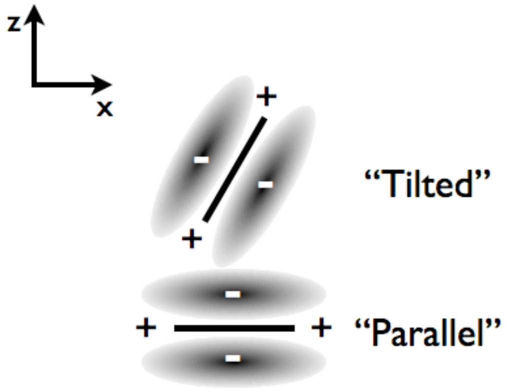

Figure 7.6. Packing arrangement for bithiophene.

7.3.3 Doubly charged bithiophene clusters

To look at the effects of charge localization when multiple positive charges are present, we performed calculations on two series of doubly charged clusters. For this set of calculations, a +1 charge is placed on both end molecules of each cluster (see Figure 7.6). In Series 1, the end molecules are parallel to the x-axis and in Series 2, the end molecules are tilted with respect to the x-axis.

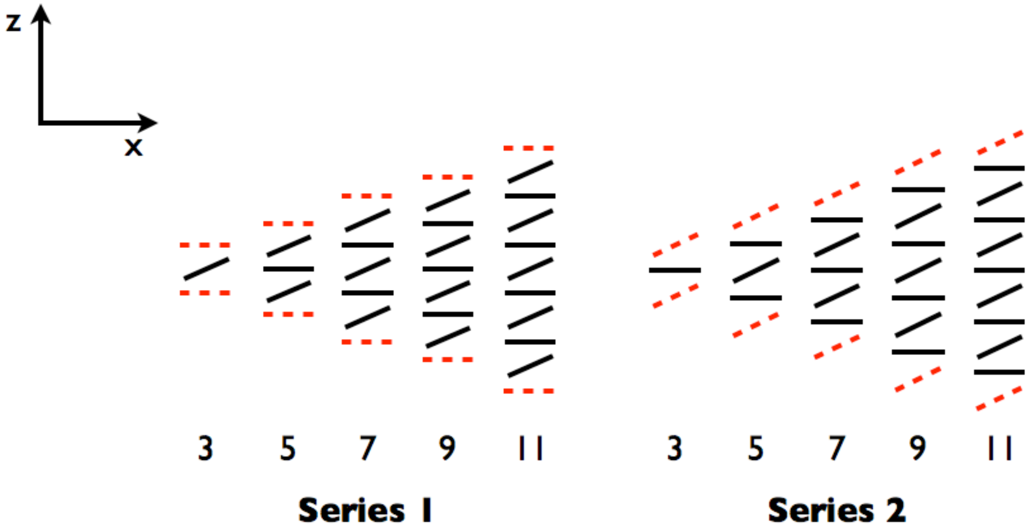

Figure 7.7. Bithiophene Series for Figure 5. A red dashed line represents the molecule at which the charge is localized in CDFT calculations.

Figure 7.7 shows the HOMO energies plotted as a function of 1/N. For Series 1, the HOMO energies increases linearly as the cluster size increases regardless as to whether or not CDFT is used, suggesting no localization occurs within the cluster sizes considered. Also, there is very little difference in the DFT and CDFT energies. For Series 2, the DFT HOMO energies increase as the cluster size increase, which indicates charge delocalization. However, when CDFT is used, the HOMO energies appear to saturate for clusters with more than 7 molecules with B3LLYP, but to a significantly lesser degree with M06-2X. This saturation indicates that the positive charges are more likely to localize on the end molecules in larger clusters. Based on our results with singly charged clusters, this is not surprising since localization did not appear until ~7 molecules.

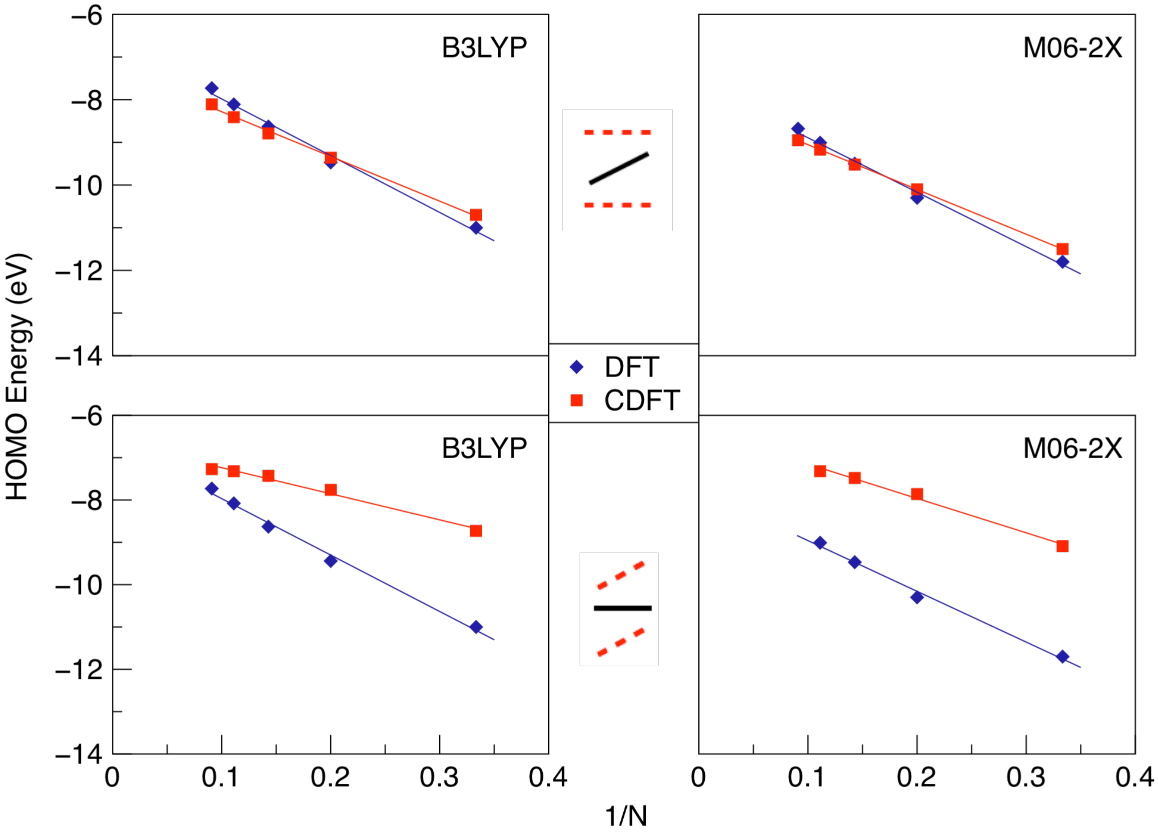

Figure 7.8. HOMO Energy vs. 1/N for doubly charged bithiophene clusters**.** Shown are B3LYP (left) and M06-2X results for Series 1 (top) and Series 2. Blue diamonds represent DFT calculations and red squares represent CDFT calculations.

As before, we examined the average charge of the carbon atoms for each molecular fragment in the clusters. Figure 7.8 shows the charge plotted as a function of the molecular fragment in a 7-molecule cluster for both Series. Again, we found that the average charge on the tilted molecules is more positive than for those that are parallel to the x-axis when standard DFT is used. When CDFT is used, the charge is much more positive on the end molecules as expected. For the Series 1 cluster, the charge difference between the DFT and CDFT calculations is smaller when compared to the singly charged cluster. Again, this is likely due to polarization effects, which makes it difficult to localize the positive charges on the “parallel” ends, which is reflected in the top plots of Figure 7.2. The small change in charge throughout the cluster between the DFT and CDFT calculations may also account for the small difference in HOMO energies for Series 1.

For Series 2, the charge difference is significantly larger, especially between the end molecules and their closest neighbors. This indicates that it is easier to localize the positive charge on the end molecule, again due to polarization effects between the tilted and parallel sites.

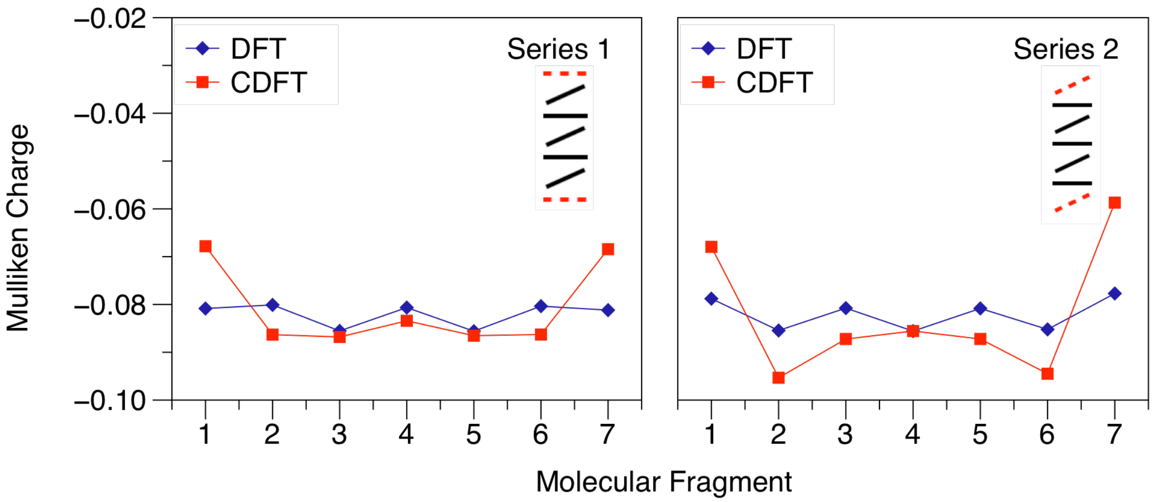

Figure 7.9. Average carbon Mulliken charge vs. molecular fragment for the 7-molecule doubly charged cluster in Series 1 (left) and Series 2. Blue diamonds represent DFT calculations and red squares represent CDFT calculations (B3LYP).

7.4 SINGLY CHARGED 2D BITHIOPHENE CLUSTER

Finally, we examined the effects of localizing a single positive charge on a two dimensional bithiophene cluster. For these calculations, a nine-molecule fragment was extracted from the crystal structure and the positive charge was localized on the center molecule for the CDFT calculations (see Figure 7.10b). The HOMO energies calculated using standard and constrained DFT were -6.94 eV and -8.30 eV respectively. As for the 1D clusters, we plotted the average Mulliken charge on the carbon atoms in each bithiophene molecule as a function of the molecular fragment (Figure 7.10a). Unlike for the 1D clusters, the average charges on each bithiophene molecule are nearly equivalent when DFT is used, although there appears to be slightly more positive charge on molecules **1** and **9**. As expected, the positive charge on the center molecule (**5**) is significantly higher when CDFT is used. However, the localized charge does not affect the neighboring sites equally. The charge on molecules **2** and **8** are affected more by the positive charge on molecule 5 than the remaining molecules. This result suggests that the effects of a charge carrier localized on one or more sites in a crystal lattice can be anisotropic.

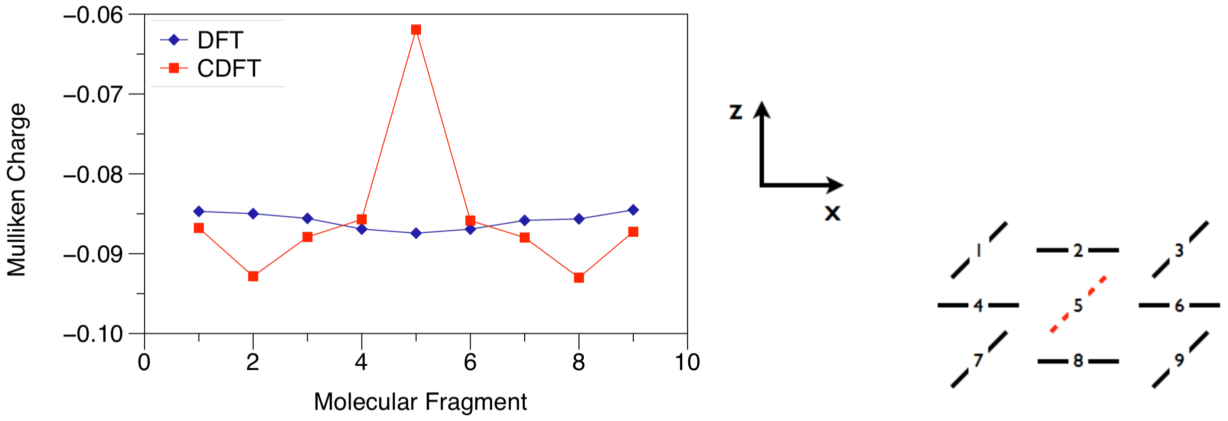

(a) (b)

Figure 7.10. (a) Average carbon Mulliken charge vs. molecular fragment for the 2D 9-molecule cluster (b). Blue diamonds represent DFT calculations and red squares represent CDFT calculations (B3LYP).

7.5 CONCLUSION

We have used standard and constrained DFT calculations to examine the assumption of charge carrier localization in existing VRH models. Our results show that a positive charge can delocalize over at least 7 molecules. This suggests that VRH models may need to change to account for the possibility that a charge carrier is delocalized over several molecular sites. Not doing so may result in misinterpretations of charge transfer events. For example, if a charge carrier is truly delocalized over several sites, a short distance "hop" of the delocalized charge can be misinterpreted as a long distance hopping event.

We have also shown that positive charge is less likely to localize on the tilted molecules than those that are parallel to the x-axis in our ID bithiophene clusters due to polarization effects. For the 2D cluster, the positive charge localized on the center molecule was shown to affect the molecules directly above and below it (molecules **2** and **8** respectively). Even when the charge is allowed to delocalize throughout the cluster, molecules **1** and **9** have slightly more positive charge than the other molecules in the cluster. This suggests that charge carriers in a film or crystal can affect the local neighborhood anisotropically. These results not only illustrate the importance of including electrostatic interactions in existing models for charge transport in organic semiconductors but also suggest that these interactions cannot be assumed to be isotropic.

In practice, both delocalized charge carriers and polarization effects should be incorporated into computer simulation models for charge transport in organic semiconductors. Due to the size of the clusters involved, this would likely require performing quantum chemistry calculations on clusters that represent a section of the grid considered for the simulation. Such calculations would help us to determine how much a charge carrier will delocalize and examine polarization effects. These calculations would then be used to set up additional parameters to model charge transport through disordered materials in a more realistic manner.

8.0 SUMMARY

In this dissertation, experimental work combined with theoretical calculations were used to study the dynamics of charge transfer, molecular collisions, and ion fragmentation, which are among the most fundamental processes in chemistry. The research present in this dissertation not only gives insight into these processes, but also demonstrates how such insight can be useful in a variety of applications including proteomics and the fabrication of electronic devices.

Chapter 1 gave an introduction to the Penning ionization reaction and what is known about its dynamics. This introductory chapter also discussed the application of Penning ionization to mass spectrometry and how it may be used in conjunction with quantum chemistry calculations and unimolecular kinetics to study molecular ion fragmentation. The chapter concludes with an overview of the research presented in the following two chapters.

Chapter 2 described the experimental methods used to study the Penning ionization of formamide and acetamide by excited stated noble gases. A detailed description of the crossed beam apparatus is given as well as details concerning data acquisition.

Mass spectra from the Penning ionization of formamide by He*, Ne*, and Ar* were discussed in Chapter 3. When compared with the standard 70 eV electron ionization spectrum, the He* and Ne * spectra showed higher yields of ions resulting from α bond cleavage, which can be attributed to the differences in the dynamics of the two ionization methods. Also, the Ar* spectrum only shows the molecular ion, and ions resulting from H-atom elimination and decarbonylation. The fragmentation pathways in the Ar* spectrum were then analyzed using quantum chemistry and RRKM calculations. These calculations were used to predict ion yields, which were in good agreement with the experimental Ar* spectrum.

Chapter 4 served as an introduction to the remaining chapters, which focus on charge transport in organic semiconductor materials. This chapter introduced the history and types of organic semiconductors as well as their application to electronic devices. A brief outline of charge transport models and a review of computer simulation studies is also given. The chapter concludes with an overview of the remaining three chapters of this work.

In Chapter 5, the effects of defects and electrostatic interactions on charge transport in a model organic field effect transistor are discussed. These effects are studied using a course-grained Monte-Carlo simulation that treats disorder by explicitly adding defect sites. The simulations show that electrostatic interactions are essential in studying the field and carrier concentration dependence on charge transport in devices that contain defects. Without the inclusion of electrostatic interactions, simulations of I-V behavior show negative differential resistance, an unphysical effect. The results also show that while charge transport decreases as a function of neutral defect concentration, it is roughly constant at low charged defect concentrations.

Chapter 6 discusses the effects of traps on charge transport in the model system discussed above. Charge traps are also explicitly treated in the simulation model. The simulations show that charge transport decreases as a function of trap concentration, reaches a minimum, and recovers at high trap concentrations when the distribution of trap sites is homogeneous. Also, the dependence of charge transport on trap concentration was shown to depend on the distribution of trap sites. For highly heterogeneous trap distributions, charge transport decreases at low trap concentrations but does not recover at high trap concentrations. However, as the distribution of trap sites becomes more uniform, charge transport begins to recover at high trap concentrations.

Finally, the effects of charge localization on the orbital energies of positively charged bithiophene clusters are discussed in Chapter 7. Standard and constrained DFT calculations are used to make this comparison. The results show that the positive charge delocalizes over at least seven molecules. It is also shown that for 1D clusters, it is easier to localize the positive charge on “tilted” rather than “parallel” molecules due to polarization effects. In addition, it was shown that a positive charge affects sites anisotropically in 2D clusters.

The results presented in Chapters 5-7 suggest that variable range hopping (VRH) models for charge transport need several changes to better describe charge transport in organic semiconductors. First, the possibility that charge carriers may be delocalized over several molecular sites must be considered in order to accurately describe the distance over which a hopping event occurs. Also, we must consider that energy and distance distributions depend on a variety of variables. Finally, VRH models should consider the local neighborhood in which a charge transfer event occurs. This work has shown that electrostatic interactions can significantly affect charge transport in organic materials, especially when considering charged and neutral defects.

APPENDIX A

SUPPORTING INFORMATION FOR CHAPTER 3

A.1 TABLES OF RELATIVE ABUNDANCES AND ION YIELDS FOR NG* + $HCONH_2$

The following tables show the results from the least squares fitting for individual Ng* + $HCONH_2$ spectra.

Table A.1. Relative abundances from the least squares fitting of He* + $HCONH_2$ spectra .

Date of Experiment	8/25/2006		8/11/2008		9/30/2008		10/2/2008	
m/z	Relative Abundance	Error	Relative Abundance	Error	Relative Abundance	Error	Relative Abundance	Error
15	0.00535	0.00135					0.00233	0.00119
16	0.38511	0.02118	0.18557	0.02495	0.31747	0.03394	0.205	0.02254
17	0.60483	0.03009	0.31064	0.03787	0.47581	0.0465	0.31894	0.03209
18	0.41027	0.02223	0.0561	0.00938	0.07796	0.01232	0.04063	0.00687
27	0.01114	0.00259	0.00643	0.00327			0.00503	0.00282
28	0.13277	0.01163	0.08683	0.01859	0.02608	0.00691	0.03143	0.00822
29	0.8268	0.04327	0.45668	0.06281	0.49782	0.05198	0.54938	0.06035
42	0.02078	0.00467	0.04848	0.02092	0.02215	0.00962	0.02652	0.01166
43	0.36611	0.02751	0.38788	0.0787	0.39241	0.05735	0.40152	0.06375
44	0.54676	0.03645	0.56364	0.10236	0.5443	0.07217	0.55682	0.08025
45	1	0	1	0	1	0	1	0
46	0.02238	0.00486	0.04242	0.01934	0.00633	0.0043	0.02273	0.01068

Table A.1 Continued

Date of Experiment	12/15/2008		12/18/2008		Average	Standard Deviation
m/z	Relative Abundance	Error	Relative Abundance	Error		
15	0.00596	0.00355			0.00455	0.00194
16	0.2486	0.05317	0.34047	0.04708	0.28037	0.07954
17	0.36149	0.0729	0.50534	0.06506	0.42951	0.11799
18	0.06666	0.01888	0.05268	0.01163	0.11738	0.14404
27					0.00753	0.00320
28	0.54063	0.13009	0.20741	0.04118	0.17086	0.19338
29	0.48489	0.11943	0.77307	0.11105	0.59811	0.16010
42			0.07857	0.03033	0.03930	0.02463
43	0.46154	0.15824	0.37143	0.08291	0.39682	0.03435
44	0.61538	0.19416	0.63571	0.12113	0.57710	0.03870
45	1	0	1	0	1	0
46	0.01923	0.0219	0.01429	0.01131	0.02123	0.01206

Table A.2. Percent yields from the least squares fitting of He* + $HCONH_2$ spectra.

Date of Experiment	8/11/2008		9/30/2008		10/2/2008		12/15/2008		Average	Standard Deviation
m/Z	Number of Counts	Percent Yield	Number of Counts	Percent Yield	Number of Counts	Percent Yield	Number of Counts	Percent Yield		
16	881	6.18	1406	9.54	843	6.61	772	7.67	7.50	1.50
17	1474	10.34	2108	14.30	1312	10.29	1126	11.19	11.53	1.89
18	240	1.68	345	2.34	167	1.31	207	2.06	1.85	0.45
29	2168	15.21	2206	14.96	2260	17.73	1507	14.97	15.72	1.34
42	230	1.61	98	0.66	109	0.86		0.00	0.78	0.66
43	1841	12.91	1738	11.79	1652	12.96	1434	14.25	12.98	1.00
44	2675	18.77	2411	16.35	2291	17.97	1912	19.00	18.02	1.20
45	4746	33.29	4430	30.05	4114	32.27	3107	30.87	31.62	1.44
Total Counts	14255		14742		12748		10065			

Table A.3. Relative abundances from the least squares fitting of Ne* + $HCONH_2$ spectra.

Date of Experiment	8/18/2006		8/29/2006		9/07/2006		3/23/2009		
m/z	Relative Abundance	Error	Relative Abundance	Error	Relative Abundance	Error	Relative Abundance	Error	Renormalized Relative Abundance
15	0.00099	0.00046	0.00099	0.00046					
16	0.09733	0.00621	0.097	0.00618	0.25811	0.02054	0.0767	0.00703	0.094944
17	0.83643	0.0286	0.83358	0.0285	0.84612	0.05099	0.69152	0.03046	0.85619
18	0.50052	0.01934	0.49881	0.01928	0.59675	0.03867	0.18134	0.01209	0.224525
20	0.86418	0.03043	0.86349	0.03042	0.80713	0.03867	1	0	
21	0.00277	0.0085	0.00276	0.00085					
22	0.07009	0.00533	0.07004	0.00533	0.07497	0.00903	0.09592	0.00803	
27	0.00171	0.00079	0.00171	0.00079					
28	0.04026	0.00446	0.04026	0.00446	0.04021	0.00868	0.07012	0.00852	0.086748
29	1	0	1	0	1	0	0.69399	0.03637	0.859131
30	0.01604	0.00264	0.01604	0.00264					
43	0.02838	0.0045	0.02833	0.00453			0.02292	0.00602	0.028452
44	0.9149	0.03961	0.92176	0.04002	0.91836	0.07948	0.80771	0.04916	1
45	0.8548	0.03773	0.8634	0.0382	0.85076	0.0753	0.78074	0.04806	0.9666
46	0.02115	0.00382			0.00932	0.005	0.01214	0.00429	0.014999

Table A.3 Continued

Date of Experiment	3/24/2006			3/25/2006			3/27/2006		
m/z	Relative Abundance	Error	Renormalized Relative Abundance	Relative Abundance	Error	Renormalized Relative Abundance	Relative Abundance	Error	Renormalized Relative Abundance
15									
16	0.06777	0.008	0.077418	0.0633	0.00737	0.07394	0.05236	0.00741	0.08574
17	0.68898	0.03717	0.787542	0.66637	0.03417	0.77818	0.50997	0.03282	0.83502
18	0.08441	0.00914	0.096572	0.09721	0.00955	0.11348	0.10403	0.01129	0.17043
20	1	0		1	0		1	0	
21									
22	0.09306	0.00961		0.08939	0.0084		0.08793	0.01052	
27									
28	0.11937	0.0176	0.136488	0.06881	0.01267	0.0804	0.05534	0.01199	0.09067
29	0.72347	0.05386	0.826976	0.78583	0.05503	0.91751	0.61076	0.05172	1
30									
43				0.02882	0.01152	0.03364	0.0228	0.01083	0.03741
44	0.87746	0.09395	1	0.85646	0.07813	1	0.60203	0.06901	0.98571
45	0.8265	0.09074	0.944793	0.80705	0.07531	0.94241	0.57923	0.06738	0.9483
46	0.0181	0.01089	0.020763	0.00412	0.00421	0.00475	0.00456	0.00469	0.00753

Table A.3 Continued

	Average	Standard Deviation
m/z		
15	0.00099	0.00000
16	0.11207	0.06508
17	0.82472	0.02977
18	0.31444	0.21016
20	0.84493	0.03274
21	0.00277	0.00001
22	0.07170	0.00283
27	0.00171	0.00000
28	0.07358	0.03606
29	0.94337	0.07543
30	0.01604	0.00000
43	0.03124	0.00413
44	0.96296	0.04209
45	0.91015	0.05109
46	0.01309	0.00696

Table A.4. Percent yields from the least squares fitting of Ne* + $HCONH_2$ spectra.

Date of Experiment	8/18/2006		8/29/2006		9/7/2006		3/23/2009	
m/z	Counts	Percent Yield	Counts	Percent Yield	Counts	Percent Yield	Counts	Percent Yield
16	924	2.58	923	2.56	1396	6.60	614	2.44
17	7942	22.17	7928	22.03	4576	21.62	5537	22.00
28	382	1.07	383	1.06	217	1.03	561	2.23
29	9496	26.51	9511	26.42	5408	25.55	5556	22.07
43	270	0.75	269	0.75		0.00	184	0.73
44	8688	24.26	8767	24.36	4966	23.46	6467	25.69
45	8117	22.66	8212	22.82	4601	21.74	6251	24.84
Total Counts	35819		35993		21164		25170	

Table A.4 Continued

Date of Experiment	3/24/2009		3/25/2009		3/27/2009		Average	Standard Deviation
m/z	Counts	Percent Yield	Counts	Percent Yield	Counts	Percent Yield		
16	481	2.05	389	1.93	330	2.15	2.90	1.65
17	4893	20.87	4094	20.34	3214	20.97	21.43	0.71
28	848	3.62	423	2.10	349	2.28	1.91	0.95
29	5138	21.92	4827	23.98	3849	25.11	24.51	1.92
43		0.00	177	0.88	144	0.94	0.58	0.40
44	6213	26.50	5261	26.14	3794	24.75	25.02	1.11
45	5870	25.04	4958	24.63	3650	23.81	23.65	1.27
Total Counts	23443		20129		15330			

Table A.5. Relative abundances from the least squares fitting of Ar* + $HCONH_2$ spectra.

Date of Experiment	9/14/2006		9/25/2006		10/2/2006	
m/z	Relative Abundance	Error	Relative Abundance	Error	Relative Abundance	Error
17	0.08253	0.00251	0.20164	0.0066	0.06814	0.00259
29	0.00324	0.0006	0.00292	0.00029	0.01065	0.00168
40	0.21711	0.00706	0.28185	0.00054	0.53976	0.01566
44	0.05987	0.00351	0.06352	0.01103	0.06617	0.00457
45	1	0	1	0	1	0
46	0.02071	0.0019	0.02326	0.00223	0.02133	0.00236

Table A.5 Continued

Date of Experiment	1/27/2009		1/29/2009		Average	Standard Deviation
m/z	Relative Abundance	Error	Relative Abundance	Error		
17	0.05343	0.00126	0.04349	0.00164	0.08985	0.06422
29	0.00882	0.00074	0.00969	0.00114	0.00706	0.00370
40	0.52448	0.01218	0.58961	0.02079	0.43056	0.16861
44	0.0702	0.00449	0.07647	0.00703	0.06725	0.00639
45	1	0	1	0	1.00000	0.00000
46	0.01759	0.00201	0.01941	0.00316	0.02046	0.00212

Table A.6. Percent yields from the least squares fitting of Ar* + $HCONH_2$ spectra.

Date of Experiment	9/14/2006		10/2/2006		1/27/2009		1/29/2009		Average	Standard Deviation
m/z	Counts	Percent Yield	Counts	Percent Yield	Counts	Percent Yield	Counts	Percent Yield		
17	6679	7.20	3152	5.95	9923	4.72	5058	3.85	5.43	1.46
29	262	0.28	493	0.93	1637	0.78	1127	0.86	0.71	0.29
44	4845	5.23	3061	5.78	13038	6.20	8894	6.77	5.99	0.65
45	80919	87.29	46262	87.34	185735	88.31	116318	88.52	87.86	0.64
Total Counts	92705		52968		210333		131397			

A.2 CALCULATION OF ENTHALPY OF FORMATION USING QUANTUM CHEMISTRY CALCULATIONS

The standard enthalpy of formation (ΔH_f) for a given species may be estimated using atomization energies and quantum chemistry calculations when an experimental value is not available.[194] ΔH_f is defined as the enthalpy change when one mole of a species is produced from its constituent elements in their standard states (1 bar and 298K). For example, the formation reaction for HCNH is,

$$\mathrm{H}_{2\,(g)} + \frac{1}{2}\mathrm{N}_{2\,(g)} + \mathrm{C}_{(s)} \rightarrow \mathrm{HCNH}_{(g)} \tag{38}$$

To calculate ΔH_f, the atomization enthalpy (ΔH_{atom}) is needed, which is the enthalpy change when a species is dissociated into its constituent atoms in the gas phase. This may be calculated using enthalpies obtained from quantum chemistry calculations. For, example, ΔH_{atom} for HCNH is,

$$2\mathrm{H}_{(atom)} + \mathrm{N}_{(atom)} + \mathrm{C}_{(atom)} \rightarrow \mathrm{HCNH}_{(g)} \tag{39a}$$

$$\Delta H_{atom} = H_{HCNH} - 2H_H - H_N - H_C \tag{39b}$$

To get the ΔH_f , the experimental atomization enthalpies for the constituent elements of the species are added to ΔH_{atom},

$$\Delta H_f^\circ = \Delta H_{atom} + \sum \Delta H_{atom,elements}^\circ \tag{40}$$

Thus, ΔH_f can be estimated using a thermodynamic cycle constructed from the atomization and formation reactions for any given species.

APPENDIX B

PRELIMINARY RESULTS FOR NG* + ACETAMIDE (CH_3CONH_2)

B.1 MASS SPECTRA

The following are representative mass spectra from the Penning ionization (PI) of acetamide (CH_3CONH_2) by He*, Ne*, and Ar*. Only the He* + CH_3CONH_2 spectrum has been fit using the least squares fitting procedure described in Section 3.2. Figures B.1 and B.2 show the simulation of the raw He* + CH_3CONH_2 spectrum and its corresponding "histogram" spectrum respectively. The 70 eV electron ionization (EI) spectrum from the NIST Webbook is included in Figure B.2 for comparison. Figures B.3 and B.4 show representative raw mass spectra from the PI of CH_3CONH_2 by Ne* and Ar*.

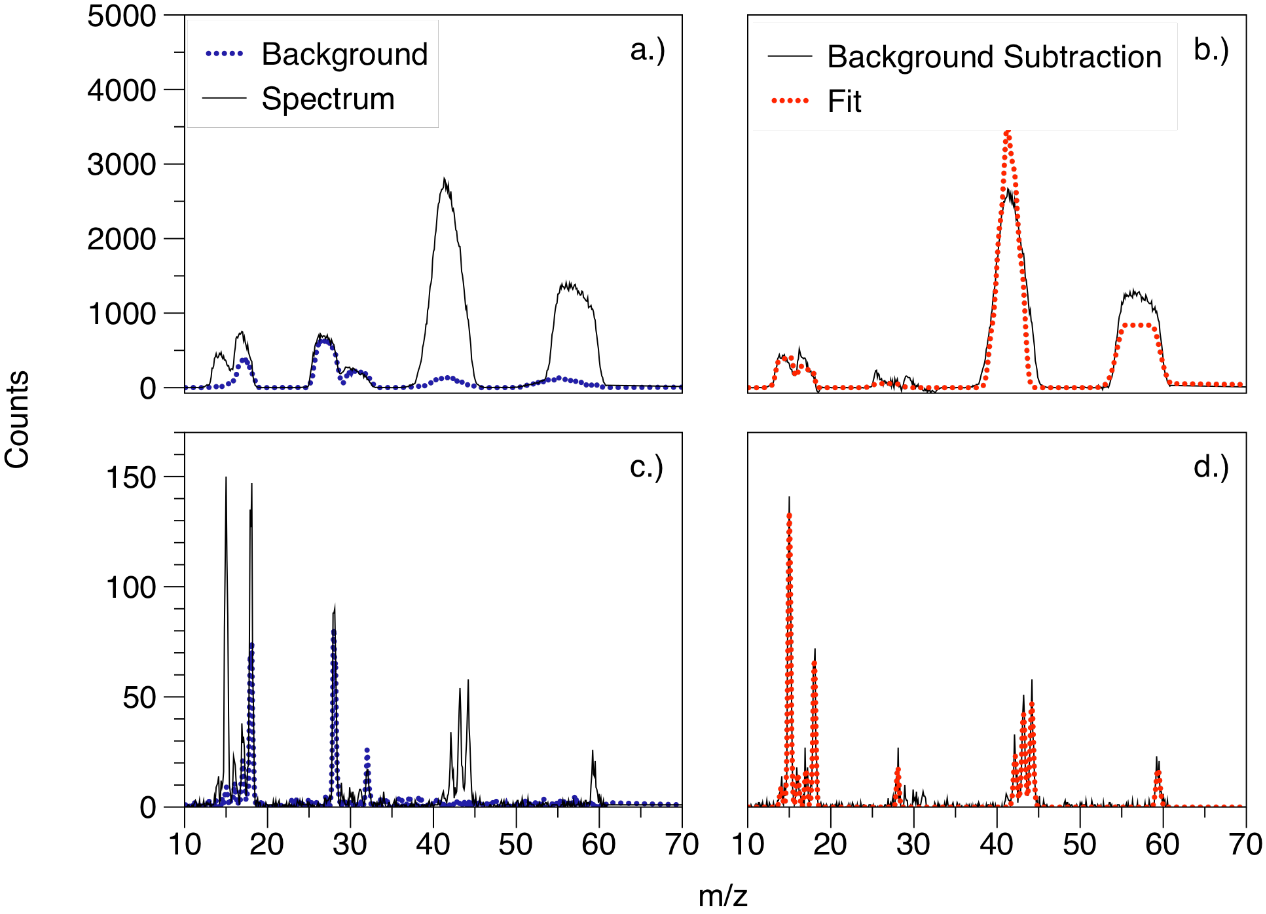

Figure B.1. Simulation of He* + CH_3CONH_2 Spectrum. .) Raw low resolution spectra, b.) Background subtraction and least squares fit for low resolution spectrum, c.) Raw high resolution spectra, d.) Background subtraction and least squares fit for high resolution spectrum.

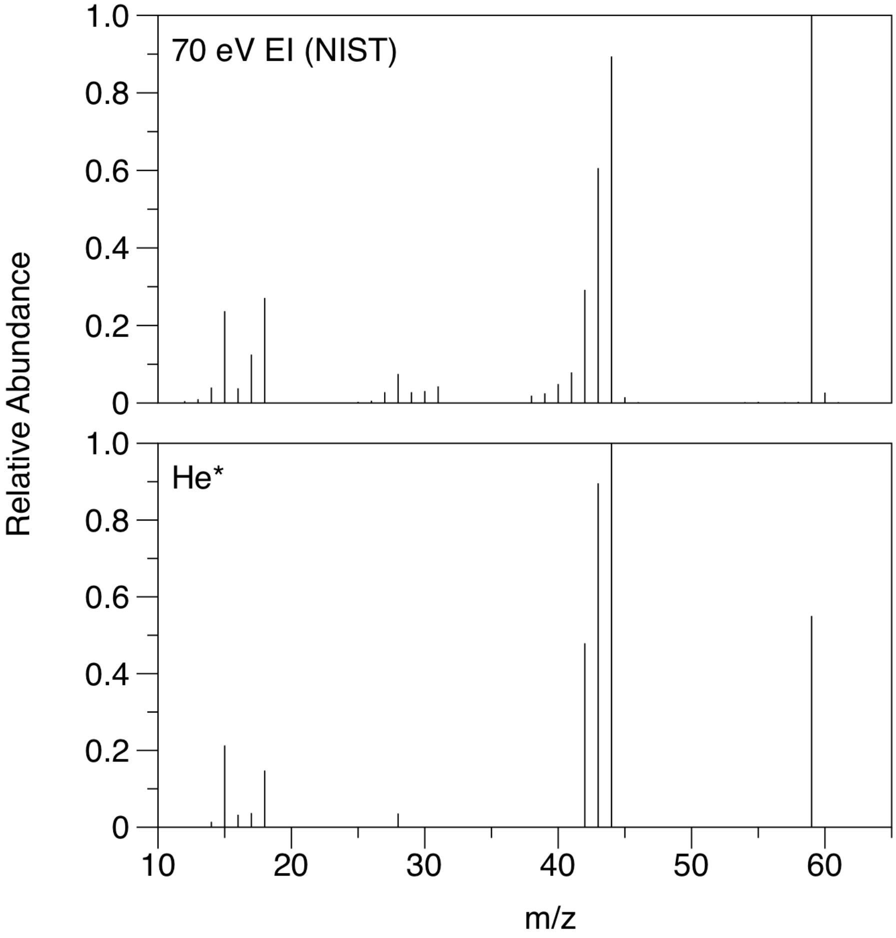

Figure B.2. Mass spectrum for He* + CH_3HCONH_2. The 70 eV EI stick spectrum (top) is included for comparison.

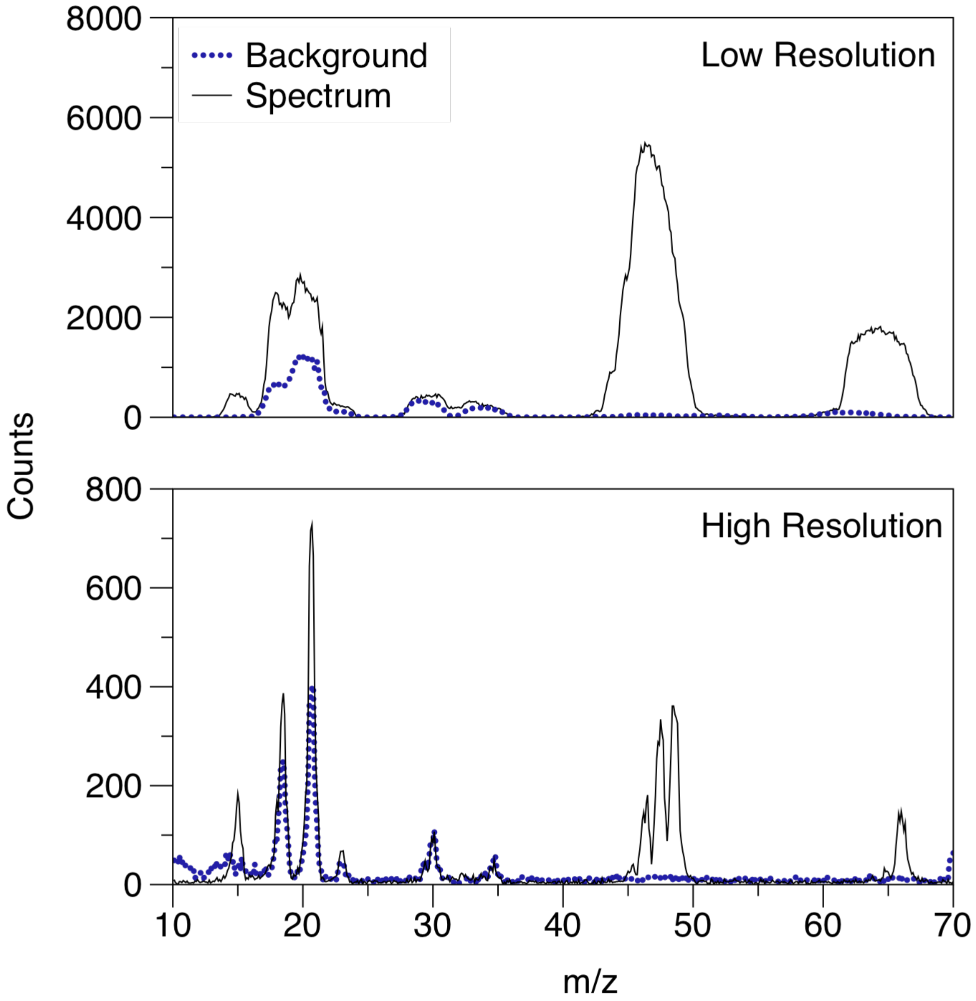

Figure B.3. Raw Ne* + CH_3CONH_2 mass spectra**.**

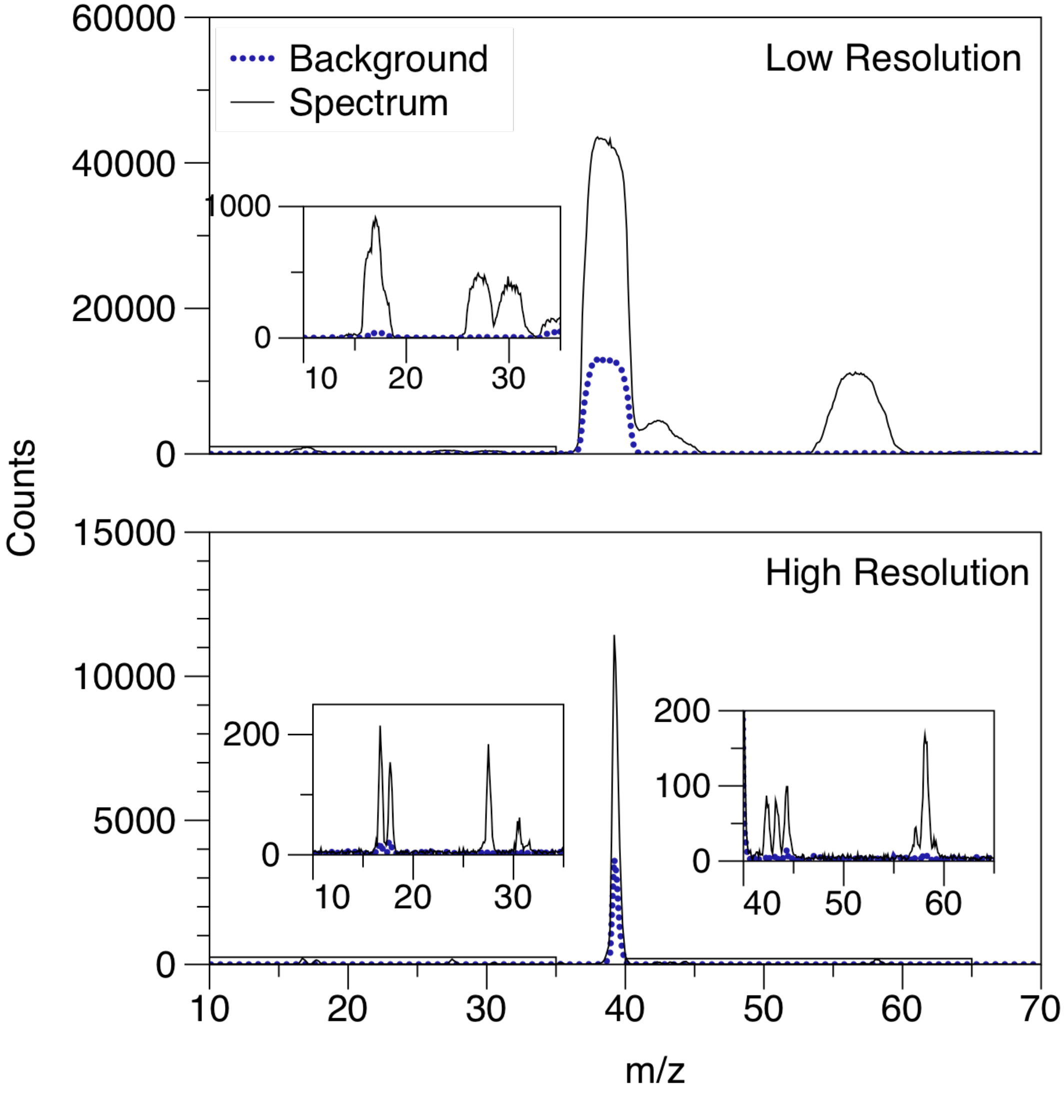

Figure B.4. Raw Ar* + CH_3CONH_2 mass spectra.

B.2 ION FRAGMENTATION ENERGETICS

Tables B.1-B.3 show the calculated reaction endothermicities at 298K for possible fragmentation pathways for CH_3CONH_2. Note that all fragmentation channels listed in the table preceding that of each noble gas are open to that noble gas. For example, all of the fragmentation channels that are open for the Ar* spectrum are also open for the Ne* spectrum.

Table B.1. Reaction endothermicities for open fragmentation pathways in the Ar* + CH_3CONH_2 spectrum.

		$\Delta H_{f,\ 298K}$		$\Delta H_{rxn,\ 298K}$	m/z
D_1	D_2^+	D_1	D_2^+		
-	$CH_3CONH_2^+$			166.5	
CO	$CH_2NH_3^+$	-26.417	203.567	234.1	31
H_2O	CH_2CNH^+	-57.7978	256	255.2	41
CH_3	$CONH_2^+$	34.821	164.453	256.2	44
NH_3	CH_2CO^+	-10.98	210.4	256.4	42
NH_2	CH_3CO^+	45.5	159	261.5	43
CH_2CO	NH_3^+	-11.4	220	265.6	17

Table B.2. Reaction endothermicities for open fragmentation pathways in the Ne* + CH_3CONH_2 spectrum.

		$\Delta H_{f,\ 298K}$		$\Delta H_{rxn,\ 298K}$	m/z
D_1	D_2^+	D_1	D_2^+		
OH	$CH_2CNH_2^+$	9.319	213.2637	279.5	42
H_2CO	CH_2NH^+	-27.701	254	283.3	29
CH_4	$CONH^+$	-17.89	244.2	283.3	43
CH_3CO	NH_2^+	-2.9	231.1	285.2	16
HCN	$CH_3COH^=$	32.299	200	289.3	32
CH_3CH_2	NO^+	28.4	208.8	294.2	30
H_2O	CH_3CN^+	-57.7978	299.07	298.2	41
CH_2CN	H_2O^+	17.7	233.200	301.9	30
N	CH_3CHOH^+	112.97	140	306.7	16
$CONH_2$	CH_3^+	-3.391585	261.7	307.9	18
O	$CH_2CNH_3^+$	59.555	241.299	309.9	45
NO	$CH_3CH_2^+$	21.58	242	315.3	15
CH	$HCOHNH_2^+$	142	124.536	318.6	43
CH_2CH_2	HNO^+	12.54	256	320.5	29

Table B.2 Continued

		$\Delta H_{f,\ 298K}$		$\Delta H_{rxn,\ 298K}$	m/z
D_1	D_2^+	D_1	D_2^+		
H	$CH_2CONH_2^+$	52.103	217.835	326.9	58
CH_2CNH	H_2O^+	42.02	233.200	332.2	18
HNO	CH_2CH_2	23.8	254.6	335.4	28
CH_2	$HCONH_2^+$	92.349	190	339.3	45
H_2	CH_2CONH^+	0	283.340	340.3	57
H_2	$CHCONH_2^+$	0	283.791	340.8	57
NH	CH_3CHO^+	90	195	342.0	44
$HCONH_2$	CH_2^+	-44.5	330.9	343.4	14
H	CH_3CONH^+	52.103	238.881	347.9	58
CH_3OH	HCN^+	11.59737	401.0	353.7	27
O	$CH_2CHNH_2^+$	59.555	202.064	357.7	43
CH_3CHOH	N^+	-13.61	323.1	366.5	14

Table B.3. Reaction endothermicities for open fragmentation pathways in the He* + CH_3CONH_2 spectrum.

		$\Delta H_{f,\ 298K}$		$\Delta H_{rxn,\ 298K}$	m/z
D_1	D_2^+	D_1	D_2^+		
CH_2NH_3	CO^+	59.90295	300	416.9	28
CH_2CNH_2	OH^+	69.17246	309.2	435.3	17
$HCOHNH_2$	CH^+	-4.540345	387.4	439.8	13
CH_2CHNH_2	O^+	14.3593	373.60	444.9	16
$H + H_2$	$HCCONH_2^+$	52.103	348.857	457.9	56
$2H_2$	$CHCON^+$	0	407.028	464.0	55
$H + H_2$	$CCONH_2^+$	52.103	357.762	466.8	56
CH_3COH	NH^+	11.59737	401.0	469.6	15
CH_2CNH_3	O	75.88723	373.60	506.4	16

APPENDIX C

SUPPORTING INFORMATION FOR CHAPTER 5

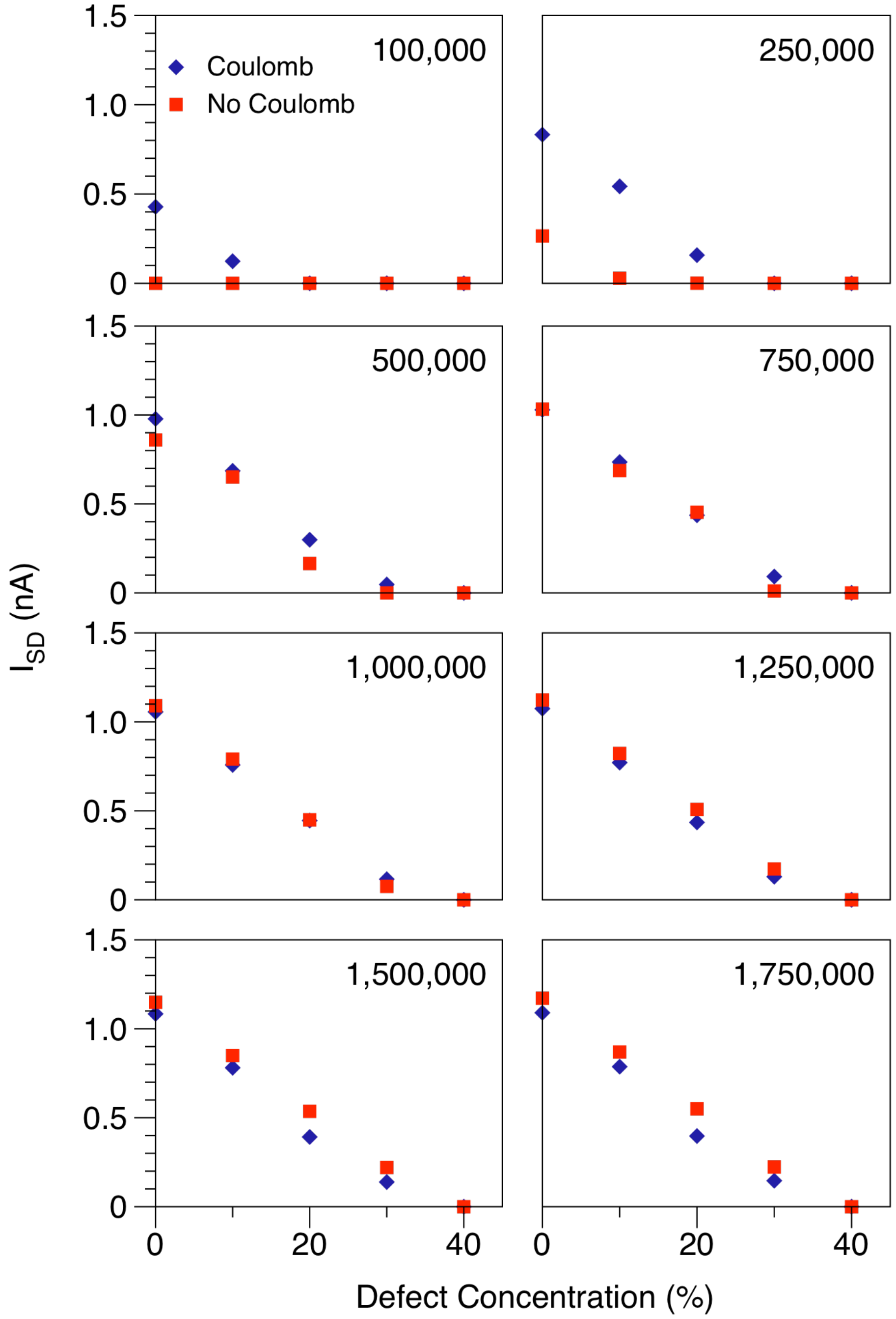

Figure C.1. I_{SD} vs. trap concentration snapshots. Blue diamonds represent calculations that include Coulomb interactions and red squares represent calculations that do not include Coulomb interactions

APPENDIX D

KINETICS CALCULATIONS: CHARGE TRAPS

D.1 KINETIC MODEL

To set up a kinetic model for our simulations, we considered two site types: normal transport sites (A) and trap sites (B). Four types of processes were considered to occur,

$$A + A^* \xrightarrow{k_A} A^* + A \tag{41a}$$

$$B + B^* \xrightarrow{k_B} B^* + B \tag{41b}$$

$$A^* + B \xrightarrow{k_f} A + B^* \tag{41c}$$

$$A + B^* \xrightarrow{k_r} A^* + B \tag{41d}$$

Here, the charged sites are denoted with an asterisk. Equations 41a and 41b show charge transfer between two normal or trap sites. Equations 41c and 41d show charge transport between normal and trap sites. The steady state rate equations are,

$$\frac{d[A]}{dt} = \frac{d[B^*]}{dt} = k_f[A^*][B] - k_r[A][B^*] \tag{42a}$$

$$\frac{d[B]}{dt} = \frac{d[A^*]}{dt} = k_r[A][B^*] - k_f[A^*][B] \tag{42b}$$

Note that contributions from charge transfer between identical sites cancel one another and the rates only depend on charge transfer between normal and trap sites. The rate equations were solved numerically using the fourth order Runge-Kutta (RK4) method[157] implemented in a C++ program. To find the populations ($y(t_{n+1})$) of charged ([A*] and [B*]) and uncharged sites ([A] and [B]) a Taylor series that is truncated at the fourth term is used,

$$y(t_{n+1}) = y(t_n) + hy'(t_n) + \frac{h^2}{2!}y''(t_n) + \frac{h^3}{3!}y'''(t_n) + \frac{h^4}{4!}y''''(t_n), \quad n = 0,1,2,...,N \tag{43}$$

Here, N is the total number of steps taken in the kinetics simulation, $y'(t_n)$ is the rate equation that describes the population change, and h is the step size, which is given by:

$$h = \frac{t_N - t_0}{N} \tag{44}$$

The higher order terms are found using the finite difference. For example, $y''(t_n)$ is given by:

$$y''(t_n) = \frac{\Delta y'}{\Delta t} = \frac{y'(t_n + h) - y'(t_n)}{h}$$

Our MC simulations are typically run for 50,000 iterations, which simulates 50 ns. To represent this in the kinetic model, a step size of 0.5 ns and a total of 100 steps were used.

The rate constants k_f and k_r were found using the relationship between the free energy and equilibrium constant,

$$\Delta G = -RT \ln K \tag{45}$$

R is the universal gas constant and *T* is the absolute temperature. Neglecting the entropy, ΔG is approximately equal to $\Delta\varepsilon$ and,

$$K = \frac{k_f}{k_r} \tag{46}$$

Setting k_r=1 yields k_f for each value of $\Delta\varepsilon$ used in our calculations. These rate constants are tabulated in Table D.1.

Table D.1. Trap energies and corresponding k_f values.

$\Delta\varepsilon$ (eV)	k_f
-0.2	2288.7
-0.15	330.8
-0.1	47.840
-0.05	6.9167
-0.01	1.4722
0.01	0.67924
0.05	0.14458
0.1	0.020903
0.15	0.0030221
0.2	0.00043693

D.2 RESULTS OF RK4 SIMULATIONS

Initial populations were generated using a separate C++ program that takes the total number of sites as well as the trap and charge concentrations and randomly distributes charge carriers between A and B sites. For our MC simulations, a grid of 256x1024 sites is used (262,144 sites total). The initial concentrations are given in Table D.2.

Table D.2. Initial populations of A, A*, B, and B*

Trap Concentration (%)	$[A]_0$	$[A^*]_0$	$[B]_0$	$[B^*]_0$
10	233892	2275	25739	238
20	207548	2031	52079	486
30	181698	1815	77847	784
40	155815	1651	103562	1116
50	129731	1305	129803	1305
60	103662	1096	156019	1367
70	78429	779	181167	1769
80	52079	486	207548	2031
90	25739	238	233892	2275

Tables D.3-D.12 give [A], [A*], [B], [B*] after 100 steps (50 ns) for the $\Delta\varepsilon$ values shown in Table D.1. Also given are population ratios.

Table D.3. Final populations and population ratios for Δε = -0.2 eV.

Trap Concentration (%)	$[A]_t$	$[A^*]_t$	$[B]_t$	$[B^*]_t$	[A*]/[[A]	[B*]/[B]	[B]/[A]	[B*]/[A*]
10	236018	149	23614	2364	6.333E-04	1.001E-01	1.000E-01	1.581E+01
20	209568	11	50059	2506	5.071E-05	5.007E-02	2.389E-01	2.358E+02
30	183509	4	76036	2595	1.985E-05	3.413E-02	4.143E-01	7.125E+02
40	157464	2	101913	2765	1.514E-05	2.713E-02	6.472E-01	1.159E+03
50	131034	2	128500	2608	1.508E-05	2.030E-02	9.807E-01	1.320E+03
60	104757	1	154924	2462	1.075E-05	1.589E-02	1.479E+00	2.186E+03
70	79207	1	180389	2547	1.382E-05	1.412E-02	2.277E+00	2.327E+03
80	53364	1	207063	2516	1.836E-05	1.215E-02	3.880E+00	2.568E+03
90	25976	1	233655	2512	3.729E-05	1.075E-02	8.995E+00	2.593E+03

Table D.4. Final populations and population ratios for Δε = -0.15 eV.

Trap Concentration (%)	$[A]_t$	$[A^*]_t$	$[B]_t$	$[B^*]_t$	[A*]/[[A]	[B*]/[B]	[B]/[A]	[B*]/[A*]
10	234659	1508	24972	1005	6.425E-03	4.026E-02	1.064E-01	6.668E-01
20	208699	880	50928	1637	4.219E-03	3.213E-02	2.440E-01	1.859E+00
30	182994	519	76551	2080	2.834E-03	2.718E-02	4.183E-01	4.012E+00
40	157155	311	102222	2456	1.979E-03	2.403E-02	6.505E-01	7.897E+00
50	130876	160	128658	2450	1.226E-03	1.904E-02	9.831E-01	1.526E+01
60	104670	88	155011	2375	8.401E-04	1.532E-02	1.481E+00	2.701E+01
70	79166	42	180430	2506	5.322E-04	1.389E-02	2.279E+00	5.947E+01
80	53347	18	207080	2499	3.314E-04	1.207E-02	3.882E+00	1.414E+02
90	25971	6	233660	2507	2.362E-04	1.073E-02	8.997E+00	4.087E+02

Table D.5. Final populations and population ratios for $\Delta\varepsilon = -0.1$ eV.

Trap Concentration (%)	$[A]_t$	$[A*]_t$	$[B]_t$	$[B*]_t$	[A*]/[[A]	[B*]/[B]	[B]/[A]	[B*]/[A*]
10	234023	2144	25608	369	9.162E-03	1.440E-02	1.094E-01	1.720E-01
20	207777	1802	51850	715	8.671E-03	1.380E-02	2.495E-01	3.971E-01
30	181995	1518	77550	1081	8.338E-03	1.395E-02	4.261E-01	7.126E-01
40	156165	1301	103212	1466	8.332E-03	1.420E-02	6.609E-01	1.127E+00
50	130068	968	129466	1642	7.442E-03	1.268E-02	9.954E-01	1.696E+00
60	103994	764	155687	1699	7.347E-03	1.091E-02	1.497E+00	2.224E+00
70	78695	513	180901	2035	6.521E-03	1.125E-02	2.299E+00	3.965E+00
80	53063	302	207364	2215	5.684E-03	1.068E-02	3.908E+00	7.345E+00
90	25838	139	233793	2374	5.383E-03	1.015E-02	9.048E+00	1.707E+01

Table D.6. Final populations and population ratios for $\Delta\varepsilon = -0.05$ eV.

Trap Concentration (%)	$[A]_t$	$[A*]_t$	$[B]_t$	$[B*]_t$	[A*]/[[A]	[B*]/[B]	[B]/[A]	[B*]/[A*]
10	233909	2258	25722	255	9.653E-03	9.918E-03	1.100E-01	1.130E-01
20	207579	2000	52048	517	9.636E-03	9.929E-03	2.507E-01	2.584E-01
30	181739	1774	77806	825	9.764E-03	1.060E-02	4.281E-01	4.647E-01
40	155864	1602	103513	1165	1.028E-02	1.125E-02	6.641E-01	7.271E-01
50	129779	1257	129755	1353	9.683E-03	1.043E-02	9.998E-01	1.077E+00
60	103712	1046	155969	1417	1.009E-02	9.085E-03	1.504E+00	1.355E+00
70	78469	739	181127	1809	9.417E-03	9.988E-03	2.308E+00	2.448E+00
80	52907	458	207520	2059	8.654E-03	9.923E-03	3.922E+00	4.497E+00
90	25755	223	233877	2290	8.640E-03	9.794E-03	9.081E+00	1.029E+01

Table D.7. Final populations and population ratios for Δε = -0.01 eV.

Trap Concentration (%)	[A]$_t$	[A*]$_t$	[B]$_t$	[B*]$_t$	[A*]/[[A]	[B*]/[B]	[B]/[A]	[B*]/[A*]
10	233894	2273	25738	240	9.720E-03	9.306E-03	1.100E-01	1.053E-01
20	207551	2028	52076	489	9.773E-03	9.384E-03	2.509E-01	2.409E-01
30	181701	1812	77844	787	9.971E-03	1.011E-02	4.284E-01	4.345E-01
40	155819	1647	103558	1120	1.057E-02	1.081E-02	6.646E-01	6.798E-01
50	129735	1301	129799	1309	1.003E-02	1.008E-02	1.000E+00	1.006E+00
60	103667	1091	156014	1372	1.052E-02	8.797E-03	1.505E+00	1.258E+00
70	78432	776	181164	1772	9.889E-03	9.783E-03	2.310E+00	2.285E+00
80	52881	484	207546	2033	9.152E-03	9.795E-03	3.925E+00	4.201E+00
90	25740	237	233891	2276	9.202E-03	9.732E-03	9.087E+00	9.610E+00

Table D.8. Final populations and population ratios for Δε = 0.01 eV.

Trap Concentration (%)	[A]$_t$	[A*]$_t$	[B]$_t$	[B*]$_t$	[A*]/[[A]	[B*]/[B]	[B]/[A]	[B*]/[A*]
10	233891	2276	25740	237	9.730E-03	9.216E-03	1.101E-01	1.042E-01
20	207547	2032	52080	485	9.793E-03	9.304E-03	2.509E-01	2.384E-01
30	181696	1817	77849	782	1.000E-02	1.004E-02	4.285E-01	4.302E-01
40	155812	1654	103565	1113	1.061E-02	1.075E-02	6.647E-01	6.731E-01
50	129728	1308	129806	1302	1.008E-02	1.003E-02	1.001E+00	9.959E-01
60	103661	1097	156020	1366	1.059E-02	8.754E-03	1.505E+00	1.245E+00
70	78427	781	181169	1767	9.960E-03	9.753E-03	2.310E+00	2.262E+00
80	52877	488	207550	2029	9.227E-03	9.776E-03	3.925E+00	4.159E+00
90	25738	239	233893	2274	9.287E-03	9.722E-03	9.087E+00	9.514E+00

Table D.9. Final populations and population ratios for Δε = 0.05 eV.

Trap Concentration (%)	$[A]_t$	$[A^*]_t$	$[B]_t$	$[B^*]_t$	[A*]/[[A]	[B*]/[B]	[B]/[A]	[B*]/[A*]
10	233890	2277	25741	236	9.737E-03	9.156E-03	1.101E-01	1.035E-01
20	207544	2035	52083	482	9.806E-03	9.250E-03	2.510E-01	2.367E-01
30	181692	1821	77853	778	1.002E-02	9.993E-03	4.285E-01	4.272E-01
40	155808	1658	103569	1109	1.064E-02	1.070E-02	6.647E-01	6.685E-01
50	129724	1312	129810	1298	1.011E-02	9.998E-03	1.001E+00	9.891E-01
60	103656	1102	156025	1361	1.063E-02	8.724E-03	1.505E+00	1.235E+00
70	78423	785	181173	1763	1.001E-02	9.732E-03	2.310E+00	2.247E+00
80	52874	491	207553	2026	9.278E-03	9.763E-03	3.925E+00	4.131E+00
90	25737	240	233894	2273	9.345E-03	9.716E-03	9.088E+00	9.449E+00

Table D.10. Final populations and population ratios for Δε = 0.1 eV.

Trap Concentration (%)	$[A]_t$	$[A^*]_t$	$[B]_t$	$[B^*]_t$	[A*]/[[A]	[B*]/[B]	[B]/[A]	[B*]/[A*]
10	233889	2278	25742	235	9.738E-03	9.142E-03	1.101E-01	1.033E-01
20	207543	2036	52084	481	9.809E-03	9.238E-03	2.510E-01	2.363E-01
30	181691	1822	77854	777	1.003E-02	9.982E-03	4.285E-01	4.266E-01
40	155807	1659	103570	1108	1.065E-02	1.069E-02	6.647E-01	6.675E-01
50	129723	1313	129811	1297	1.012E-02	9.990E-03	1.001E+00	9.875E-01
60	103655	1103	156026	1360	1.064E-02	8.718E-03	1.505E+00	1.233E+00
70	78422	786	181174	1762	1.002E-02	9.727E-03	2.310E+00	2.243E+00
80	52874	491	207553	2026	9.290E-03	9.760E-03	3.925E+00	4.124E+00
90	25736	241	233895	2272	9.358E-03	9.714E-03	9.088E+00	9.434E+00

Table D.11. Final populations and population ratios for Δε = 0.15 eV.

Trap Concentration (%)	$[A]_t$	$[A^*]_t$	$[B]_t$	$[B^*]_t$	[A*]/[[A]	[B*]/[B]	[B]/[A]	[B*]/[A*]
10	233889	2278	25742	235	9.738E-03	9.140E-03	1.101E-01	1.033E-01
20	207543	2036	52084	481	9.810E-03	9.236E-03	2.510E-01	2.363E-01
30	181691	1822	77854	777	1.003E-02	9.980E-03	4.285E-01	4.265E-01
40	155806	1660	103571	1107	1.065E-02	1.069E-02	6.647E-01	6.673E-01
50	129723	1313	129811	1297	1.012E-02	9.989E-03	1.001E+00	9.873E-01
60	103655	1103	156026	1360	1.064E-02	8.717E-03	1.505E+00	1.233E+00
70	78422	786	181174	1762	1.002E-02	9.726E-03	2.310E+00	2.242E+00
80	52874	491	207553	2026	9.292E-03	9.760E-03	3.925E+00	4.123E+00
90	25736	241	233895	2272	9.360E-03	9.714E-03	9.088E+00	9.432E+00

Table D.12. Final populations and population ratios for Δε = 0.2 eV.

Trap Concentration (%)	$[A]_t$	$[A^*]_t$	$[B]_t$	$[B^*]_t$	[A*]/[[A]	[B*]/[B]	[B]/[A]	[B*]/[A*]
10	233889	2278	25742	235	9.739E-03	9.140E-03	1.101E-01	1.033E-01
20	207543	2036	52084	481	9.810E-03	9.236E-03	2.510E-01	2.363E-01
30	181691	1822	77854	777	1.003E-02	9.980E-03	4.285E-01	4.264E-01
40	155806	1660	103571	1107	1.065E-02	1.069E-02	6.647E-01	6.673E-01
50	129723	1313	129811	1297	1.012E-02	9.989E-03	1.001E+00	9.873E-01
60	103655	1103	156026	1360	1.064E-02	8.717E-03	1.505E+00	1.233E+00
70	78422	786	181174	1762	1.002E-02	9.726E-03	2.310E+00	2.242E+00
80	52874	491	207553	2026	9.292E-03	9.760E-03	3.925E+00	4.123E+00
90	25736	241	233895	2272	9.360E-03	9.714E-03	9.088E+00	9.432E+00

APPENDIX E

SUPPORTING INFORMATION FOR CHAPTER 7

E.1 SAMPLE CDFT INPUT FILE

The following is a Q-Chem input file for a CDFT calculation on the singly charged 5-molecule from Series 1. Note that the positive charge is constrained to the central molecule (see figure 7.1).

```
$rem
  JOBTYPE SP
  EXCHANGE B3LYP
  BASIS 6-31G(d)
  BASIS2 r64g
  MAX_SCF_CYCLES 100
  GUI=2
  CDFT true
  CDFT_POSTDIIS true
  CDFT_PREDIIS true
  PRINT_ORBITALS true
  MOLDEN_FORMAT true
$end

$comment
Tilted T-Shaped Cationic Pentamer
$end

$molecule
  1 2
  H       5.11825      26.32296      22.26853
```

C	5.83125	25.93106	22.86663
S	6.27585	26.87686	24.19923
H	6.47695	24.22226	22.12523
C	6.57685	24.80636	22.75883
C	7.50905	25.76896	24.65863
H	7.52885	27.86376	26.75043
C	7.57605	24.64356	23.78663
C	8.27125	27.15976	26.68143
H	8.31845	23.93956	23.71753
C	8.33825	26.03436	25.80943
C	9.27045	26.99696	27.70923
H	9.37035	27.58106	28.34273
S	9.57145	24.92646	26.26873
C	10.01605	25.87226	27.60133
H	10.72905	25.48036	28.19953
H	6.41165	22.59486	18.05613
C	7.12475	22.98676	18.65423
S	7.56925	22.04096	19.98693
H	7.77045	24.69556	17.91293
C	7.87035	24.11146	18.54643
C	8.80255	23.14886	20.44623
H	8.82235	21.05406	22.53813
C	8.86955	24.27426	19.57423
C	9.56475	21.75806	22.46903
H	9.61195	24.97826	19.50513
C	9.63175	22.88346	21.59703
C	10.56385	21.92086	23.49683
H	10.66385	21.33676	24.13033
S	10.86495	23.99136	22.05633
C	11.30955	23.04556	23.38903
H	12.02255	23.43746	23.98713
H	7.70515	20.55196	13.84373
C	8.41825	20.16006	14.44193
S	8.86275	21.10586	15.77453
H	9.06395	18.45126	13.70053
C	9.16385	19.03536	14.33403
C	10.09605	19.99796	16.23383
H	10.11585	22.09276	18.32573
C	10.16305	18.87256	15.36183
C	10.85825	21.38876	18.25663
H	10.90545	18.16856	15.29283
C	10.92515	20.26336	17.38463
C	11.85735	21.22596	19.28443
H	11.95725	21.81006	19.91803
S	12.15845	19.15546	17.84393
C	12.60305	20.10126	19.17663

```
  H     13.31605      19.70936      19.77473
  H      8.99865      16.82386       9.63133
  C      9.71175      17.21576      10.22953
  S     10.15625      16.26996      11.56213
  H     10.35745      18.92456       9.48813
  C     10.45735      18.34046      10.12163
  C     11.38955      17.37786      12.02143
  H     11.40935      15.28306      14.11333
  C     11.45655      18.50326      11.14953
  C     12.15165      15.98706      14.04423
  H     12.19885      19.20726      11.08043
  C     12.21865      17.11246      13.17223
  C     13.15085      16.14986      15.07203
  H     13.25075      15.56576      15.70563
  S     13.45195      18.22036      13.63163
  C     13.89645      17.27456      14.96423
  H     14.60955      17.66646      15.56243
  H     10.29215      14.78096       5.41893
  C     11.00515      14.38906       6.01713
  S     11.44975      15.33486       7.34973
  H     11.65095      12.68026       5.27573
  C     11.75085      13.26436       5.90933
  C     12.68305      14.22696       7.80903
  H     12.70275      16.32176       9.90093
  C     12.75005      13.10156       6.93713
  C     13.44515      15.61776       9.83183
  H     13.49235      12.39756       6.86803
  C     13.51215      14.49236       8.95993
  C     14.44435      15.45496      10.85973
  H     14.54425      16.03906      11.49323
  S     14.74545      13.38446       9.41923
  C     15.18995      14.33026      10.75183
  H     15.90305      13.93836      11.35003
$end

$cdft
 -1
 -1 1 16
 -1 17 32
  1 33 48
 -1 49 64
 -1 65 80
$end
```

E.2 HARTREE-FOCK (HF) CALCULATIONS AND SPIN ORBITAL COMPARISONS

Figure E.1 show plots of the HOMO energies vs. 1/N for neutral, singly, and doubly charged clusters using HF calculations. Series 1 and 2 are the same series used for the DFT calculations discussed in Section 7.3.

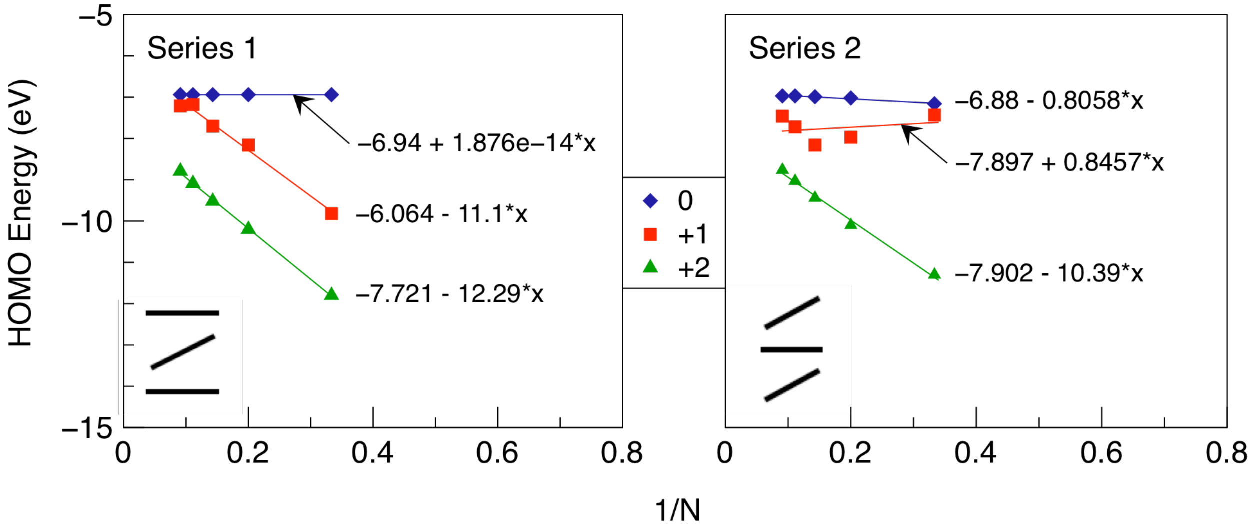

Figure E.1. HF HOMO Energy vs. 1/N for neutral, singly, and doubly charged bithiophene clusters. Blue diamonds represent neutral clusters, red squares represent singly charged clusters, and green triangles represent doubly charged clusters.

Figure E.2 show plots of the alpha and beta HOMO energies vs. 1/N for the singly charged clusters using unrestricted (U) and restricted-open (RO) HF and B3LYP calculations. Series 1 and 2 are the same series that are used for the DFT calculations discussed in Section 7.3. Note that these plots are an attempt to resolve the trend for the singly charged Series 2 clusters observed in Figure E.1, but to no avail.

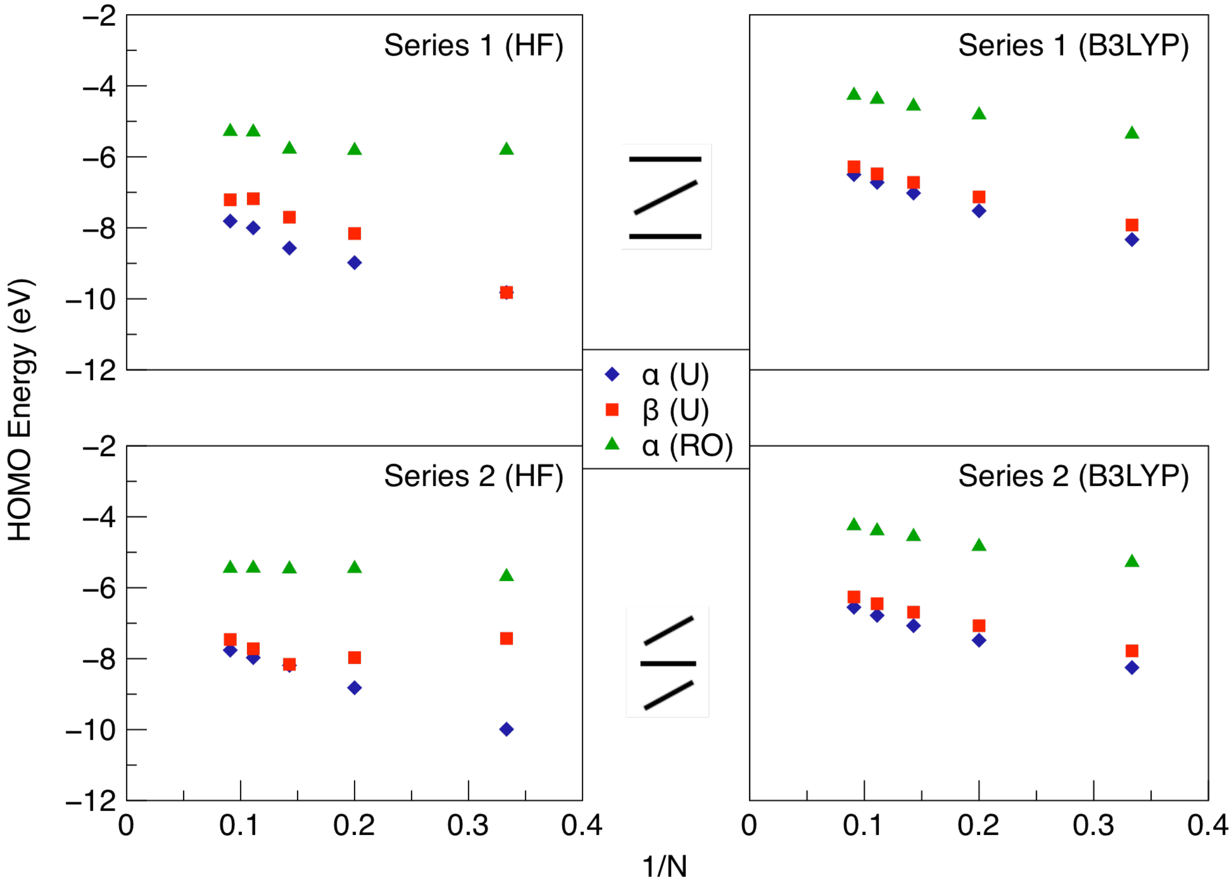

Figure E.2. HOMO Energy vs. 1/N for singly charged bithiophene clusters. Shown are HF (left) and B3LYP results for Series 1 (top) and Series 2. Blue diamonds represent unrestricted alpha orbitals, red squares represent unrestricted beta orbitals, and green triangles represent restricted open alpha orbitals.

BIBLIOGRAPHY

1. Noroski, J. H. Collision energy dependence of the reactions of metastable with small molecules. Ph. D. Dissertation, University of Pittsburgh, Pittsburgh, 2009.

2. Penning, F. M., *Naturwissenschaften* **1927,** *15*, 818.

3. Miller, W. H., *J. Chem. Phys.* **1970,** *52* (7), 3563.

4. Siska, P., *Rev. Mod. Phys.* **1993,** *65* (2), 337-412.

5. Sholette, W. P.; Muschlitz, E. E., Jr., *J. Chem. Phys.* **1962,** *36*, 3368-73.

6. Fort, J.; Laucagne, J. J.; Pesnelle, A.; Watel, G., *Phys. Rev. A.* **1978,** *18*, 2063.

7. Fort, J.; Laucagne, J. J.; Pesnelle, A.; Watel, G., *Phys. Rev. A.* **1976,** *14*, 658.

8. Martin, D. W.; Bernfeld, D.; Siska, P. E., *Chem. Phys. Lett.* **1984,** *110* (3), 298-302.

9. Martin, D. W.; Weiser, C.; Sperlein, R. F.; Bernfeld, D. L.; Siska, P. E., *J. Chem. Phys.* **1989,** *90* (3), 1564-76.

10. Schmeltekopf, A. I.; Fehsenfield, F. C., *J. Chem. Phys.* **1970,** *53*, 3173.

11. Weiser, C.; Siska, P. E., *J. Chem. Phys.* **1986,** *85* (8), 4746-7.

12. Appolloni, L.; Brunetti, B.; Vecchiocattivi, F.; Volpi, G. G., *J. Phys. Chem.* **1988,** *92* (2), 918-21.

13. Aguilar, A.; Brunetti, B.; Gonzalez, M.; Vecchiocattivi, F., *Chem. Phys.* **1990,** *145* (2), 211-18.

14. Navarro, A. A.; Brunetti, B.; Falcinelli, S.; Gonzalez, M.; Vecchiocattivi, F., *J. Chem. Phys.* **1992,** *96* (1), 433-9.

15. Khan, A.; Siddiqui, H. R.; Martin, D. W.; Siska, P. E., *Chem. Phys. Lett.* **1981,** *84* (2), 280-5.

16. Khan, A.; Siddiqui, H. R.; Siska, P. E., *J. Chem. Phys.* **1991,** *94* (4), 2588-99.

17. Longley, E.; Dunlavy, D.; Falcetta, M.; Bevsek, H.; Siska, P., *J. Phys. Chem.* **1993,** *97* (10), 2097-2105.

18. Longley, E.; Siska, P., *J. Chem. Phys.* **1997,** *106* (15), 6365-6375.

19. Gulati, K.; Longley, E.; Dorko, M.; Bittinger, K.; Siska, P., *J. Chem. Phys.* **2004,** *120* (18), 8485-8493.

20. Mhaka, A.; Siska, P., *Chem. Phys. Lett.* **1998,** *282* (3-4), 299-304.

21. Leu, M. T.; Siska, P. E., *J. Chem. Phys.* **1974,** *60*, 4082.

22. Haberland, H.; Lee, Y. T.; Siska, P. E., *Adv. Chem. Phys.* **1981,** *45* (2), 487-585.

23. Khan, A.; Siddiqui, H. R.; Siska, P. E., *J. Chem. Phys.* **1991,** *95* (5), 3371-80.

24. Noroski, J.; Siska, P., *Chem. Phys. Lett.* **2009,** *475* (4-6), 208-214.

25. Yamakita, Y.; Ohno, K., *J. Phys. Chem. A* **2009,** *113* (40), 10779-10786.

26. Kishirnoto, N.; Ohno, K., *J. Phys. Chem. A* **2009,** *113* (3), 521-526.

27. Yamazaki, M.; Kishimoto, N.; Ohno, K., *European Physical Journal D* **2006,** *38* (1), 47-57.

28. Biondini, F.; Brunetti, B. G.; Candori, P.; De Angelis, F.; Falcinelli, S.; Tarantelli, F.; Teixidor, M. M.; Pirani, F.; Vecchiocattivi, F., *J. Chem. Phys.* **2005,** *122* (16), 164307/1-164307/10.

29. Tian, S. X.; Kishimoto, N.; Ohno, K., *J. Electron Spectrosc. Relat. Phenom.* **2002,** *127* (3), 167-181.

30. Bevsek, H.; Dunlavy, D.; Siska, P., *J. Chem. Phys.* **1995,** *102* (1), 133-144.

31. Gregor, R. W.; Siska, P. E., *J. Chem. Phys.* **1981,** *74* (2), 1078-92.

32. Martin, D. W.; Siska, P. E., *J. Chem. Phys.* **1985,** *82* (6), 2630-43.

33. Baudon, J.; Feron, P.; Miniatura, C.; Perales, F.; Reinhardt, J.; Robert, J.; Haberland, H.; Brunetti, B.; Vecchiocattivi, F., *J. Chem. Phys.* **1991,** *95* (3), 1801-7.

34. Brutschy, B.; Haberland, H.; Werner, F., *J. Phys. B* **1982,** *15* (5), 731-8.

35. Herce, J. A.; Penton, J. R.; Cross, R. J.; Muschlitz Jr., E. E., *J. Chem. Phys.* **1968,** *49*, 958.

36. Jones, E. G.; Harrison, A. G., *Int. J. Mass Spectrom. Ion Processes* **1970,** *5*, 137.

37. Faubert, D.; Paul, G. J. C.; Giroux, J.; Bertrand, M. J., *Int. J. Mass Spectrom. Ion Processes* **1993,** *124*, 69.

38. Fagerquist, C. K.; Hellerstein, M. K.; Faubert, D.; Bertrand, M. J., *J Am Soc Mass Spectrom* **2001,** *12* (6), 754-61.

39. Boutin, M.; Lesage, J.; Ostiguy, C.; Bertrand, M. J., *J. Am. Soc. Mass Spectrom.* **2004,** *15* (9), 1315-1319.

40. Boutin, M.; Lesage, J.; Ostiguy, C.; Bertrand, M. J., *J. Anal. Appl. Pyrolysis* **2003,** *70* (2), 505-517.

41. Jamin, E.; Chevolleau, S.; Touzet, C.; Tulliez, J.; Debrauwer, L., *Anal. Bioanal. Chem.* **2007,** *387* (8), 2931-2941.

42. Lebel, S. L.; Beaugrand, C.; Esplat, F.; Bertrand, M. J., *Ind. Biotechnol.* **2006,** *2* (1), 40-43.

43. Moore, S., *Chemosphere* **2002,** *49* (2), 121-125.

44. Moore, S.; Vromet, L.; Rondeau, B., *Chemosphere* **2003,** *54* (4), 453-459.

45. Wilkes, J. G.; Rafii, F.; Sutherland, J. B.; Rushing, L. G.; Buzatu, D. A., *Rapid Commun. Mass Spectrom.* **2006,** *20* (16), 2383-2386.

46. Hiraoka, K.; Fujimaki, S.; Kambara, S.; Furuya, H.; Okazaki, S., *Rapid Commun. Mass Spectrom.* **2004,** *18* (19), 2323-2330.

47. Lifshitz, C., *International Journal of Mass Spectromentry and Ion Processes* **1992,** *118*, 315.

48. Radom, L., *International Journal of Mass Spectromentry and Ion Processes* **1992,** *118*, 339.

49. Ruttink, P. J. A.; Burgers, P. C.; Terlouw, J. K., *Int. J. Mass Spectrom. Ion Processes* **1995,** *145* (1/2), 35-43.

50. McAdoo, D. J.; Olivella, S.; Sole, A., *J. Phys. Chem. A* **1998,** *102* (52), 10798-10804.

51. Choe, J. C., *Chem. Phys. Lett.* **2006,** *421*.

52. Martinez, -. N., E.; Vazquez, S. A., *Journal of Molecular Structure (Theochem)* **2000,** *505*, 109.

53. Lu, H. F.; Li, F. Y.; Nagaya, K.; Hayashi, M.; Mishima, K.; Lin, S. H., *THEOCHEM* **2006,** *761* (1-3), 159-169.

54. Kim, M. H.; Shen, L.; Tao, H. L.; Martinez, T. J.; Suits, A. G., *Science* **2007,** *315* (5818), 1561-1565.

55. Guner, V.; Khuong, K. S.; Leach, A. G.; Lee, P. S., *J. Phys. Chem. A* **2003,** *107*, 11445.

56. Jobst, K. J.; Terlouw, J. K.; Luider, T. M.; Burgers, P. C., *Anal. Chim. Acta* **2008,** *627* (1), 136-147.

57. Jobst, K. J.; Ruttink, P. J. A.; Terlouw, J. K., *Int. J. Mass Spectrom.* **2008,** *269* (3), 165-176.

58. Jobst, K. J.; Burgers, P. C.; Ruttink, P. J. A.; Terlouw, J. K., *Int. J. Mass Spectrom.* **2006,** *254* (3), 127-135.

59. Lee, Y. T.; McDonald, J. D.; LaBreton, P. R.; Herschbach, D. R., *Rev. Sci. Instrum.* **1969,** *40* (11), 1402.

60. Weiser, C.; Siska, P. E., *Rev. Sci. Instrum.* **1987,** *58* (11), 2124-30.

61. Daly, N. R., *Rev. Sci. Instrum.* **1960,** *31* (3), 264.

62. Madison, T. A.; Siska, P. E., *J. Chem. Phys.* **2009,** *131* (13), 134309.

63. Lindstrom, P. J.; Mallard, W. G., NIST Chemistry WebBook. June 2005 ed.; 2005; Vol. 69.

64. Kishimoto, N.; Osada, Y.; Ohno, K., *Journal of Electron Spectroscopy and Related Phenomena* **2001,** *114*, 183-190.

65. Keller, W.; Morgner, H.; Mueller, W., *Mol. Phys.* **1986,** *57*, 637.

66. See Y.K. Kim, K.K. Irikura, M.E. Rudd, M.A. Ali, P.M. Stone, J.S. Coursey, R.A. Dragoset, A.R. Kishore, K.J. Olsen, A.M. Sansonetti, G.G. Wiersna, D.S. Zucker, and M.A. Zucker, "Electron Impact Cross Sections for Ionization and Excitation." NIST Physical Reference Data. http://www.nist.gov/pml/data/ionization/index.cfm

67. Montgomery, J. A., Jr.; Frisch, M. J.; Ochterski, J. W.; Petersson, G. A., *J. Chem. Phys.* **1999,** *110* (6), 2822-2827.

68. Siegbahn, H. L.; Asplund, P.; Kelfve, K.; Hamrin, L.; Karlson, K.; Siegbahn, K., *Journal of Electon Spectroscopy and related Phenomena* **1974,** *5*, 1059.

69. Gonzalez, C.; Schlegel, H. B., *J. Chem. Phys.* **1989,** *90*, 2154.

70. Jobst, K. J.; Ruzni Hanifa, M.; Terlouw, J. K., *Chem. Phys. Lett.* **2008,** *462* (4-6), 152-157.

71. Lee, R.; Ruttink, P. J. A.; Burgers, P. C.; Terlouw, J. K., *Can. J. Chem.* **2005,** *83* (11), 1847-1863.

72. Whitten, G. Z.; Rabinowitch, B. S., *J. Chem. Phys.* **1963,** *38*, 2466.

73. Miller, W. H., *J. Am. Chem. Soc.* **1979,** *101* (23), 6810.

74. Eckart, C., *Phys. Rev.* **1930,** *35* (11), 1303.

75. Beyer, T.; Swinehart, D. F., *Communications of the ACM* **1973,** *16* (6), 1.

76. Robinson, P. J.; Holbrook, K. A., *Unimolecular Reactions*. Wiley: New York, 1972.

77. Meisels, G. G.; Chen, C. T.; Giessner, B. G.; Emmel, R. H., *J. Chem. Phys.* **1972,** *56* (2), 793.

78. Bregel, T.; Yencha, A. J.; Ruf, P.; Waibel, H.; Hotop, H., *Zeitschrift fur Physik D: Atoms, Molecules and Clusters* **1989,** *13*, 51.

79. Bussert, W.; Ganz, J.; Hotop, H.; Ruf, P.; Siegel, A.; Waibel, H.; Botschwina, P.; Lorenzen, J., *Chem. Phys. Lett.* **1983,** *95* (3), 277.

80. The Nobel Prize in Chemistry 2000: Conductive Polymers (Advanced Information). http://nobelprize.org/nobel_prizes/chemistry/laureates/2000/chemadv.pdf

81. Volmer, M., *Annalen der Physik* **1913,** *345* (4), 775-796.

82. Koenigsberger, J.; Schilling, K., *Annalen der Physik* **1910,** *337* (6), 179-230.

83. Shirakawa, H.; Louis, E. J.; MacDiarmid, A. G.; Chiang, C. K.; Heeger, A. J., *J. Chem. Soc., Chem. Commun.* **1977,** (16), 578-580.

84. Li, L. Q.; Tang, Q. X.; Li, H. X.; Hu, W.; Yang, X. O.; Shuai, Z.; Liu, Y. Q.; Zhu, D., *Pure Appl. Chem.* **2008,** *80* (11), 2231-2240.

85. Mabeck, J. T.; Malliaras, G. G., *Anal. Bioanal.Chem.* **2006,** *384* (2), 343-353.

86. Horowitz, G., *J. Mater. Res.* **2004,** *19* (7), 1946-1962.

87. Horowitz, G., *Adv. Mater.* **1998,** *10* (5), 365-377.

88. Anikeeva, P. O.; Halpert, J. E.; Bawendi, M. G.; Bulovic, V., *Nano Lett.* **2009,** *9* (7), 2532-2536.

89. Tomova, R.; Petrova, P.; Buroff, A.; Stoycheva-Topalova, R., *Bulg. Chem. Commun.* **2007,** *39* (4), 247-259.

90. Nelson, J.; Kwiatkowski, J. J.; Kirkpatrick, J.; Frost, J. M., *Acc. Chem. Res.* **2009,** *42* (11), 1768-1778.

91. Bernede, J. C., *J. Chil. Chem. Soc.* **2008,** *53* (3), 1549-1564.

92. Nunzi, J. M., *Comptes Rendus Physique* **2002,** *3* (4), 523-542.

93. Karl, N.; Marktanner, J., *Mol. Cryst. Liq. Cryst.* **2001,** *355*, 149-173.

94. Mott, N. F., *Electronic Processes in Non-Crystalline Materials*. Clarendon Press: Oxford, 1979.

95. Miller, A.; Abrahams, E., *Phys. Rev.* **1960,** *120* (3), 745.

96. Marcus, R. A., *Annu. Rev. Phys. Chem.* **1964,** *15*, 155-196.

97. Marcus, R. A., *J. Chem. Phys.* **1956,** *24* (5), 966-978.

98. Bassler, H., *Physica Status Solidi B Basic Solid State Physics* **1993,** *175*, 15.

99. Demeyu, L.; Stafstrom, S.; Bekele, M., *Phys. Rev. B* **2007,** *76* (15), 155202.

100. Lukyanov, A.; Andrienko, D., *Phys. Rev. B* **2010,** *82* (19), 193202.

101. Borsenberger, P. M.; Pautmeier, L.; Bassler, H., *J. Chem. Phys.* **1991,** *94*, 5447.

102. Kohary, K.; Cordes, H.; Baranovskii, S. D.; Thomas, P.; Yamasaki, S.; Hensel, F.; Wendorff, J. H., *Phys. Rev. B* **2001,** *63* (9), 094202.

103. Mohan, S. R.; Joshi, M. P.; Singh, M. P., *Org. Electron.* **2008,** *9* (3), 355-368.

104. Blom, P. W. M.; deJong, M. J. M.; Vleggaar, J. J. M., *Appl. Phys. Lett.* **1996,** *68* (23), 3308-3310.

105. Veres, J.; Ogier, S. D.; Leeming, S. W.; Cupertino, D. C.; Mohialdin Khaffaf, S., **2003,** - *13* (- 3), - 204.

106. Stephan, J.; Schrader, S.; Brehmer, L., *Synth. Met.* **2000,** *111*, 353-357.

107. Novikov, S. V.; Vannikov, A. V., *Synth. Met.* **1997,** *85* (1-3), 1167-1168.

108. Mozer, A. J.; Denk, P.; Scharber, M. C.; Neugebauer, H.; Sariciftci, N. S.; Wagner, P.; Lutsen, L.; Vanderzande, D., *J. Phys. Chem. B* **2004,** *108* (17), 5235- 5242.

109. Mozer, A. J.; Sariciftci, N. S.; Pivrikas, A.; Osterbacka, R.; Juska, G.; Brassat, L.; Bassler, H., *Phys. Rev. B* **2005,** *71* (3).

110. Pai, D. M., *J. Chem. Phys.* **1970,** *52* (5), 2285- 2291.

111. Gill, W. D., *J. Appl. Phys.* **1972,** *43* (12), 5033- 5040.

112. Wolf, U.; Bassler, H.; Borsenberger, P. M.; Gruenbaum, W. T., *Chem. Phys.* **1997,** *222*, 259.

113. Pai, D. M.; Yanus, J. F.; Stolka, M., *J. Phys. Chem.* **1984,** *88*, 4714-4717.

114. Borsenberger, P. M.; Gruenbaum, W. T.; Wolf, U.; Bassler, H., *Chem. Phys.* **1998,** *234*, 277.

115. Fishchuk, II; Kadashchuk, A. K.; Vakhnin, A.; Korosko, Y.; Bassler, H.; Souharce, B.; Scherf, U., *Phys. Rev. B* **2006,** *73* (11), 115210.

116. Fishchuk, I.; Kadashchuk, A.; Bassler, H.; Weiss, D. S., *Phys. Rev. B* **2002,** *66*, 205208.

117. Hanwell, M. D.; Madison, T. A.; Hutchison, G. R., *The Journal of Physical Chemistry C* **2010,** *114* (48), 20417-20423.

118. Jaquith, M. J.; Anthony, J. E.; Marohn, J. A., *J. Mater. Chem.* **2009,** *19* (34), 6116-6123.

119. Jaquith, M.; Muller, E. M.; Marohn, J. A., *J. Phys. Chem. B* **2007,** *111* (27), 7711-7714.

120. Muller, E. M.; Marohn, J. A., *Adv. Mater.* **2005,** *17* (11), 1410.

121. Bolinger, J. C.; Fradkin, L.; Lee, K. J.; Palacios, R. E.; Barbara, P. F., *Proc. Natl. Acad. Sci. U. S. A.* **2009,** *106* (5), 1342-1346.

122. Cramer, T.; Steinbrecher, T.; Koslowski, T.; Case, D. A.; Biscarini, F.; Zerbetto, F., *Phys. Rev. B* **2009,** *79*, 155316.

123. Hallam, T.; Duffy, C. M.; Minakata, T.; Ando, M.; Sirringhaus, H., *Nanotechnology* **2009,** *20*, 025203.

124. Chen, L.; Ludeke, R.; Cui, X.; Schrott, A. G.; Kagan, C. R.; Brus, L. E., *J. Phys. Chem. B*. **2005,** *109* (5), 1834.

125. Ludeke, R.; Cartier, E., *Appl. Phys. Lett.* **2001,** *78* (25), 3998.

126. Zhou, J.; Zhou, Y. C.; Zhao, J. M.; Wu, C. Q.; Ding, X. M.; Hou, X. Y., *Phys. Rev. B* **2007,** *75* (15), 153201.

127. Mady, F.; Renoud, R.; Iacconi, P., *J. Phys.-Condes. Matter* **2007,** *19* (4), 046219.

128. Lonergan, M. C.; Nitzan, A.; Ratner, M. A., *J. Mol. Liq.* **1994,** *60* (1-3), 269-288.

129. Lonergan, M. C.; Perram, J. W.; Ratner, M. A.; Shriver, D. F., *J. Chem. Phys.* **1993,** *98* (6), 4937-4947.

130. Lonergan, M. C.; Shriver, D. F.; Ratner, M. A., *Electrochim. Acta* **1995,** *40* (13-14), 2041-2048.

131. Gartstein, Y. N.; Conwell, E. M., *J. Chem. Phys.* **1994,** *100* (12), 9175-9180.

132. Bredas, J. L.; Calbert, J. P.; da Silva, D. A.; Cornil, J., *Proc. Natl. Acad. Sci. U. S. A.* **2002,** *99* (9), 5804-5809.

133. da Silva, D. A.; Kim, E. G.; Bredas, J. L., *Adv. Mater.* **2005,** *17* (8), 1072.

134. Kim, E. G.; Coropceanu, V.; Gruhn, N. E.; Sanchez-Carrera, R. S.; Snoeberger, R.; Matzger, A. J.; Bredas, J. L., *J. Am. Chem. Soc.* **2007,** *129* (43), 13072-13081.

135. Kjelstrup-Hansen, J.; Norton, J. E.; da Silva, D. A.; Bredas, J. L.; Rubahn, H. G., *Org. Electron.* **2009,** *10* (7), 1228-1234.

136. Li, H.; Bredas, J. L.; Lennartz, C., *J. Chem. Phys.* **2007,** *126* (16), 164704.

137. Hutchison, G. R.; Ratner, M. A.; Marks, T. J., *J. Am. Chem. Soc.* **2005,** *127* (7), 2339-2350.

138. Facchetti, A.; Hutchison, G. R.; Keinan, S.; Ratner, M. A., *Inorg. Chim. Acta* **2004,** *357* (13), 3980-3990.

139. Deng, W. Q.; Goddard, W. A., *J. Phys. Chem. B* **2004,** *108* (25), 8614-8621.

140. Hutchison, G. R.; Ratner, M. A.; Marks, T. J., *J. Am. Chem. Soc.* **2005,** *127* (48), 16866-16881.

141. Barbara, P. F.; Meyer, T. J.; Ratner, M. A., *J. Phys. Chem.* **1996,** *100* (31), 13148-13168.

142. Becke, A. D., *J. Chem. Phys.* **1993,** *98* (7), 5648.

143. Lee, C.; Yang, W.; Parr, R. G., *Phys. Rev. B* **1988,** *37*, 785.

144. Dunning, T. H.; Hay, P. J., *Modern Theoretical Chemistry*. Plenum Press: New York, 1976; Vol. 3.

145. Hay, P. J.; Wadt, W. R., *J. Chem. Phys.* **1985,** *82* (1), 270.

146. Hay, P. J.; Wadt, W. R., *J. Chem. Phys.* **1985,** *82* (1), 299.

147. Wadt, W. R.; Hay, P. J., *J. Chem. Phys.* **1985,** *82* (1), 284.

148. Gaussian 03, Revision C.02, Frisch, M. J.; Trucks, G. W.; Schlegel, H. B.; Scuseria, G. E.; Robb, M. A.; Cheeseman, J. R.; Montgomery, Jr., J. A.; Vreven, T.; Kudin, K. N.; Burant, J. C.; Millam, J. M.; Iyengar, S. S.; Tomasi, J.; Barone, V.; Mennucci, B.; Cossi, M.; Scalmani, G.; Rega, N.; Petersson, G. A.; Nakatsuji, H.; Hada, M.; Ehara, M.; Toyota, K.; Fukuda, R.; Hasegawa, J.; Ishida, M.; Nakajima, T.; Honda, Y.; Kitao, O.; Nakai, H.; Klene, M.; Li, X.; Knox, J. E.; Hratchian, H. P.; Cross, J. B.; Bakken, V.; Adamo, C.; Jaramillo, J.; Gomperts, R.; Stratmann, R. E.; Yazyev, O.; Austin, A. J.; Cammi, R.; Pomelli, C.; Ochterski, J. W.; Ayala, P. Y.; Morokuma, K.; Voth, G. A.; Salvador, P.; Dannenberg, J. J.; Zakrzewski, V. G.; Dapprich, S.; Daniels, A. D.; Strain, M. C.; Farkas, O.; Malick, D. K.; Rabuck, A. D.; Raghavachari, K.; Foresman, J. B.; Ortiz, J. V.; Cui, Q.; Baboul, A. G.; Clifford, S.; Cioslowski, J.; Stefanov, B. B.; Liu, G.; Liashenko, A.; Piskorz, P.; Komaromi, I.; Martin, R. L.; Fox, D. J.; Keith, T.; Al-Laham, M. A.; Peng, C. Y.; Nanayakkara, A.; Challacombe, M.; Gill, P. M. W.; Johnson, B.; Chen, W.; Wong, M. W.; Gonzalez, C.; and Pople, J. A.; Gaussian, Inc., Wallingford CT, 2004.

149. The spacing of the grid depends significantly of the orientation of the phthalocyanine molecules relative to the substrate. We have assumed an amorphous film in this work, but changes to the lattice spacing (e.g., with an ordered film "standing up" from the substrate) does not significantly affect the results described.

150. Shi, N.; Ramprasad, R., *Appl. Phys. Lett.* **2006,** *89* (10), 102904.

151. Wu, Y. Q.; Gu, D. H.; Gan, F. X., *Opt. Mater.* **2003,** *24* (3), 477-482.

152. Chang, H. C.; Ruden, P. P.; Liang, Y.; Frisbie, C. D., *J. Appl. Phys.* **2010,** *107*, 104502.

153. Bourguiga, R.; Mahdouani, M.; Mansouri, S.; Horowitz, G., *Eur. Phys. J. Appl. Phys.* **2007,** *39* (1), 7-16.

154. Cho, M. Y.; Kang, H. S.; Kim, K.; Kim, S. J.; Joo, J.; Kim, K. H.; Cho, M. J.; Choi, D. H., *Colloids and Surfaces a-Physicochemical and Engineering Aspects* **2008,** *313*, 431-434.

155. Abthagir, P. S.; Ha, Y. G.; You, E. A.; Jeong, S. H.; Seo, H. S.; Choi, J. H., *J. Phys. Chem. B* **2005,** *109* (50), 23918-23924.

156. Young, T. Nanoscale Morphology and Phase Structure of Regioregular Poly(3-hexylthiophene) in Single and Multicomponent Systems. Ph. D Dissertation, Carnegie Mellon University, Pittsburgh, 2010.

157. Steinfield, J. I.; Francisco, J. S.; Hase, W. L., *Chemical Kinetics and Dynamics*. 2nd ed.; Prentice Hall: Upper Saddle River, 1999.

158. Calhoun, M. F.; Hsich, C.; Podzorov, V., *Physical Review Leters* **2007,** *98*, 096402.

159. Oberhoff, D.; Pernstich, K. P.; Gundlach, D. J.; Batlogg, B., *IEEE Trans. Electron Devices* **2007,** *54* (1), 17-25.

160. Kang, J. H.; da Silva, D.; Bredas, J. L.; Zhu, X. Y., *Appl. Phys. Lett.* **2005,** *86* (15), 152115.

161. Brütting, W., *Physics of Organic Semiconductors*. Wiley-VCH: Weinheim, 2005.

162. Epstein, A. J.; Joo, J.; Kohlman, R. S.; Du, G.; Macdiarmid, A. G.; Oh, E. J.; Min, Y.; Tsukamoto, J.; Kaneko, H.; Pouget, J. P., *Synth. Met.* **1994,** *65* (2-3), 149-157.

163. Joo, J.; Oh, E. J.; Min, G.; Macdiarmid, A. G.; Epstein, A. J., *Synth. Met.* **1995,** *69* (1-3), 251-254.

164. Prigodin, V. N.; Epstein, A. J., *Physica B-Condensed Matter* **2003,** *338* (1-4), 310-317.

165. Kaake, L. G.; Barbara, P. F.; Zhu, X. Y., *The Journal of Physical Chemistry Letters* **2010,** *1*, 628-635.

166. Mas-Torrent, M.; Hadley, P.; Bromley, S. T.; Crivillers, N.; Veciana, J.; Rovira, C., *Appl. Phys. Lett.* **2005,** *86* (1), 012110.

167. Mas-Torrent, M.; Hadley, P.; Ribas, X.; Rovira, C., *Synth. Met.* **2004,** *146* (3), 265-268.

168. Nicolet, A. A. L.; Hofinann, C.; Kol'chenk, M. A.; Orrit, M., *Mol. Cryst. Liq. Cryst.* **2008,** *497*, 550-559.

169. Miller, L. L.; Mann, K. R., *Acc. Chem. Res.* **1996,** *29* (9), 417-423.

170. Hill, M. G.; Penneau, J. F.; Zinger, B.; Mann, K. R.; Miller, L. L., *Chem. Mater.* **1992,** *4* (5), 1106-1113.

171. Levillain, E.; Roncali, J., *J. Am. Chem. Soc.* **1999,** *121* (38), 8760-8765.

172. Poterya, V.; Tkac, O.; Fedor, J.; Farnik, M.; Slavicek, P.; Buck, U., *International Journal of Mass Spectrometry* **2010,** *290* (2-3), 85-93.

173. Profant, V.; Poterya, V.; Farnik, M.; Slavicek, P.; Buck, U., *J. Phys. Chem. A* **2007,** *111* (49), 12477-12486.

174. Mitsui, M.; Ando, N.; Nakajima, A., *J. Phys. Chem. A* **2008,** *112* (25), 5628-5635.

175. Valeev, E. F.; Coropceanu, V.; da Silva, D. A.; Salman, S.; Bredas, J. L., *J. Am. Chem. Soc.* **2006,** *128* (30), 9882-9886.

176. Coropceanu, V.; Sanchez-Carrera, R. S.; Paramonov, P.; Day, G. M.; Bredas, J. L., *J. Phys. Chem. C* **2009,** *113* (11), 4679-4686.

177. Martinelli, N. G.; Olivier, Y.; Athanasopoulos, S.; Delgado, M. C. R.; Pigg, K. R.; da Silva, D. A.; Sanchez-Carrera, R. S.; Venuti, E.; Della Valle, R. G.; Bredas, J. L.; Beljonne, D.; Cornil, J., *Chemphyschem* **2009,** *10* (13), 2265-2273.

178. Sanchez-Carrera, R. S.; Paramonov, P.; Day, G. M.; Coropceanu, V.; Bredas, J. L., *J. Am. Chem. Soc.* **2010,** *132* (41), 14437-14446.

179. Wu, Q.; Van Voorhis, T., *Phys. Rev. A* **2005,** *72* (2), 024502.

180. de la Lande, A.; Salahub, D. R., *THEOCHEM* **2010,** *943* (1-3), 115-120.

181. Ding, F. Z.; Wang, H. B.; Wu, Q.; Van Voorhis, T.; Chen, S. W.; Konopelski, J. P., *J. Phys. Chem. A* **2010,** *114* (19), 6039-6046.

182. Oberhofer, H.; Blumberger, J., *J. Chem. Phys.* **2009,** *131* (6), 064101.

183. Wu, Q.; Van Voorhis, T., *J. Chem. Phys.* **2006,** *125* (16), 164105.

184. Wu, Q.; Van Voorhis, T., *J. Phys. Chem. A* **2006,** *110* (29), 9212-9218.

185. Wu, Q.; Van Voorhis, T., *Journal of Chemical Theory and Computation* **2006,** *2* (3), 765-774.

186. Chaloner, P. A.; Gunatunga, S. R.; Hitchcock, P. B., *Acta Crystallographica Section C: Crystal Structure Communications* **1994,** *50* (12), 1941-1942.

187. Avogadro: an open-source molecular builder and visualization tool. Version 1.0.1. http://avogadro.openmolecules.net/

188. Shao, Y.; Molnar, L. F.; Jung, Y.; Kussmann, J.; Ochsenfeld, C.; Brown, S. T.; Gilbert, A. T. B.; Slipchenko, L. V.; Levchenko, S. V.; O'Neill, D. P.; DiStasio, R. A.; Lochan, R. C.; Wang, T.; Beran, G. J. O.; Besley, N. A.; Herbert, J. M.; Lin, C. Y.; Van Voorhis, T.; Chien, S. H.; Sodt, A.; Steele, R. P.; Rassolov, V. A.; Maslen, P. E.; Korambath, P. P.; Adamson, R. D.; Austin, B.; Baker, J.; Byrd, E. F. C.; Dachsel, H.; Doerksen, R. J.; Dreuw, A.; Dunietz, B. D.; Dutoi, A. D.; Furlani, T. R.; Gwaltney, S. R.; Heyden, A.; Hirata, S.; Hsu, C. P.; Kedziora, G.; Khalliulin, R. Z.; Klunzinger, P.; Lee, A. M.; Lee, M. S.; Liang, W.; Lotan, I.; Nair, N.; Peters, B.; Proynov, E. I.; Pieniazek, P. A.; Rhee, Y. M.; Ritchie, J.; Rosta, E.; Sherrill, C. D.; Simmonett, A. C.; Subotnik, J. E.; Woodcock, H. L.; Zhang, W.; Bell, A. T.; Chakraborty, A. K.; Chipman, D. M.; Keil, F. J.; Warshel, A.; Hehre, W. J.; Schaefer, H. F.; Kong, J.; Krylov, A. I.; Gill, P. M. W.; Head-Gordon, M., *Phys. Chem. Chem. Phys.* **2006,** *8* (27), 3172-3191.

189. Zhao, Y.; Truhlar, D. G., *Theor. Chem. Acc.* **2008,** *120*, 215-241.

190. Janak , J., *Phys. Rev. B* **1978,** *18* (12), 7165.

191. Grimme, S., *J. Comput. Chem.* **2004,** *25* (12), 1463 - 1473.

192. Cohen, A. J.; Mori-Sanchez, P.; Yang, W., *Science* **2008,** *321*, 792-794.

193. Mori-Sanchez, P.; Cohen, A. J.; Yang, W., *Phys. Rev. Lett.* **2008,** *100* (14), 146401.

194. Ochterski, J. W., Thermocheistry in Gaussian. Gaussian Inc 2000.